SLAC-R-565
UC-414

A Search for Free Fractional Electric Charge Elementary Particles*

V. Halyo

Stanford Linear Accelerator Center
Stanford University
Stanford, CA 94309

SLAC-Report-565
November 2000

Prepared for the Department of Energy
under contract number DE-AC03-76SF00515

Printed in the United States of America. Available from the National Technical Information Service, U.S. Department of Commerce, 5285 Port Royal Road, Springfield, VA 22161.

*Ph.D. thesis, Stanford Linear Accelerator Center OR Stanford University, Stanford, CA 94309.

Abstract

A direct search was carried out in bulk matter for free fractional electric charge elementary particles using the largest mass single sample ever studied— about 17.4 mg of silicone oil. The search used an improved and highly automated Millikan oil drop technique. No evidence for fractional charge particles was found. The concentration of particles with fractional charge more than 0.16 e (e being the magnitude of the electron charge) from the nearest integer charge is less than 4.71×10^{-22} particles per nucleon with 95% confidence.

Acknowledgements

First, I would like to deeply thank my adviser Prof. Martin Perl for his invaluable guidance and help during my Ph. D. I will always be grateful to him for accepting me as his student. I feel privileged to have the chance to learn from his example.

Second, I would like to thank Eric Lee for sharing with me his expertise in electrical and mechanical engineering and especially for the many heated arguments. I would also like to thank Irwin Lee, for his great help in teaching me programming and for all the long, fun hours of work. Sharing the office with Eric and Irwin was a lot of fun. I thank Dinesh Loomba for his astrophysical insights on our FCP search.

In addition, I want to thank all the people with whom I have worked: Peter Kim for all his useful advice, especially while writing the paper, Prof. Edward Garwin for being kind enough to let me use his lab, Bob Leonard for showing me how to solder and wire wrap my first electrical designs, Howard J. Rogers for his patience in explaining all the basics of the machine shop, Gerard J. Oxoby for building my 1000 LEDs strobe and Gerard Putallaz for letting me use his office during the writing of my the thesis. Special thanks to Judy Meo, for her kindness, support and help throughout my Ph. D.

Last but not least, I would like to thank my husband Edi for his support, understanding and encouragement and my adorable son Tsahi who gives me joy and inspiration.

I dedicate this thesis to my dear father

Yosef Agatchy

who unfortunately cannot be with us and to my

dear mother Liliane who never ceases to support me.

Contents

List of Tables

List of Figures

Chapter 1

Introduction

Direct observation of free Fractional Charge elementary Particles (FCP) would be an undisputed signature of physics beyond the Standard Model. In this thesis, we present the results of an improved Millikan oil drop experiment designed to look for such particles. There are no confirmed discoveries of free particles with fractional electric charge. Searches have been made using accelerators, cosmic rays [1] and in bulk matter [2], [3]. Searches in bulk matter fall into two classes: those that attempt to concentrate the FCPs before the search [4] and those that directly search through a bulk matter sample [5], [6]. We prefer the direct bulk matter search because it is often difficult to make a reliable estimate of the efficiency of the pre-concentration method.

Specifically, we chose a search method based on the original Millikan experiment. We generated drops with a diameter size of a about 10 microns and then measured the electric charge on them by letting the drops fall in the air under the influence of gravity and in the presence of an alternating electric field. The forces on the drops were measured by observing the changes in the position of the drops which allowed the value of the charge to be determined. The old Millikan technique has improved from a manual and low throughput experiment to an automated experiment limited only by new technological developments. In our experiment, drops were ejected through a silicon micromachined orifice and ejected between two parallel plate capacitors producing the electric field. The falling drops were backlit by light emitting

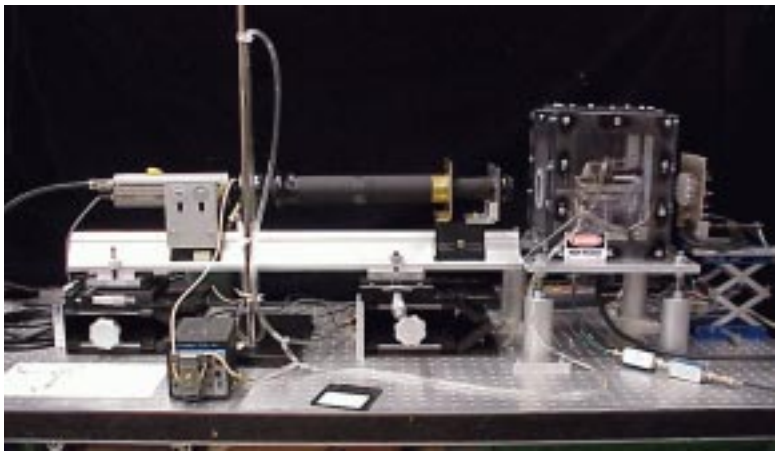

Figure 1.1: Our automated Millikan experiment.

diodes (LED) twice for each electric field orientation and a lens magnified the drop images onto a digital charge coupled device (CCD) camera interfaced to a computer. The same computer was used to simultaneously collect and analyze the data and to monitor and control the experiment.

The advantages of this method are as follows. First, the Millikan method allows a broad charge range to be studied with good charge resolution. Second, it provides a natural self-calibration of the charge measurement. Third, it is amenable to automation and simple replication. Finally, it permits a relatively large amount of material to be examined. The previous Millikan type search used about 1 mg of silicone oil and set an upper limit of less than 4.76×10^{-21} FCPs per nucleon [6]. The largest mass sample previously used in a direct bulk matter search was 4.9 mg of niobium [7] again with a negative result. The apparatus of the experiment which is shown in figure [1.1] made it possible to generate and measure the charges of multiple columns of multiple drops simultaneously, each drop being $7.6 - 11.0$ μm in diameter. This allowed us to have a large throughput of 4.17×10^7 drops or about 17.4 mg of silicone oil. The advantages of the Millikan method helped us to improve the previous limits. No evidence (or more precisely repeatable evidence) for FCPs was found. The concentration of particles with fractional charge more than 0.16 e (e being the magnitude of the electron charge) from the nearest integer charge is less than 4.71×10^{-22} particles per nucleon with a 95% confidence limit.

This thesis is organized as follows. The theoretical motivation for looking for FCPs is given in chapter 2. A review of previous FCP searches is presented in chapter 3. The theory of the experiment is presented in chapter 4. The layout of the automated Millikan experiment is presented in chapter 5 along with a discussion of the development and use of the main components. Data acquisition is described in chapter 6. A thorough discussion of the data analysis explaining various phenomena that have been taken into account, the different sources of error that affected the charge measurement accuracy and the presentation of the final results are given in chapter 7. Our conclusions are summarized in chapter 8. Our future plans including the new technique to look for FCPs, the problems we encountered and the way we overcame them are presented in chapter 9. Various contributions to the charge measurement accuracy are derived and estimated in Appendix A. The search for charged stable and massive particles using the Millikan technique is discussed in appendix B. The theory and technique of the preparation of colloidal suspensions using surfactants is explained in appendix C including instructions for preparing meteorite suspensions. Finally, a few open questions that arose during the experiment and were left unanswered are presented in appendix D.

Chapter 2

Motivation

There is no experimental evidence for free fractional electric charge particles; all known free particles are quantized in units of the electron charge (e). In the Standard Model there are fractionally charged quarks with charges of $\frac{2}{3}$ and $\frac{-1}{3}$, however previous accelerator experiments have shown that we cannot isolate them. The extremely stringent limits on free quarks led to the idea of quark confinement and to a successful QCD theory. Confinement means that we cannot see an isolated, free quark. When we pull a quark away from another quark (or antiquark) to distances of the order of the QCD scale $\Lambda \sim 1\,GeV$, the energy of the pair becomes large ($\sim \Lambda$) due to the confining potential which grows linearly with distance as $V(r) \approx \Lambda^2 r$. As a result, there is enough energy in the QCD field (gluons) to create new quarks and/or antiquarks. This shows that whenever two quarks have large kinetic energies, this energy will be transformed into the confining potential energy which in turn creates new quarks. The final state of the two energetic quarks will be many hadrons of size Λ (mesons or baryons) which are bound states of quarks and/or antiquarks.

Searches for free quarks are still necessary because they test for a possible breakdown of confinement. In our experiment we look for all types of fractional electric charge elementary particles. Like quarks, these particles may have other conserved charges. On the other hand, unlike quarks they do not have to carry color charge and be confined. We know that direct observation of free fractional charge elementary particles would be an undisputed signature of physics beyond the Standard Model.

In principle, there is no reason to exclude fractional charge particles just because they do not appear in the low energy (i.e. $\sim 250\,GeV$) theory. Theories which describe physics beyond the Standard Model often contain FCPs. A very important though speculative example is superstring theory which unifies all particles and interactions as vibrational modes of a string. All semi-realistic superstring models constructed to date contain many FCPs not only with charges $2/3$ and $-1/3$ but also with exotic ones like $1/5$, $1/7$ etc. Depending on the model these may or may not carry color (or other confining) charges. Often, even FCPs that confine lead to mesons and/or baryons which have fractional electric charge. It can be shown that, in general, if one requires gauge coupling unification (or the correct value of $sin^2\theta_w$ at high energies) in string theory one is forced to have FCPs in the physical spectrum [52]. The only way known to avoid FCPs but keep unification is to consider very complicated and unnatural constructions in string theory. Observation of FCPs would be not only the proof of physics beyond the Standard Model but also a fascinating hint of superstring theory. Other models for fractional charge particles are outlined in [53].

Of course, the fact that stable FCPs exist at very high energies does not necessarily mean that they exist today at low energies. The abundance of FCPs today depends on their properties and the cosmological evolution of the early universe. During the very early stages of the universe when the temperature was very high all particles including massive FCPs were in thermal equilibrium. As the universe expanded, it cooled down and FCPs began to fall out of equilibrium, i.e. their production and decay rates (which depend on the their mass and interactions and the temperature) became smaller than the expansion rate of the universe. As a result, after this era the number of FCPs was almost constant with their density decreasing due to the expansion of the universe. The thermal history of the universe is one of the best understood and precise subjects in Big Bang cosmology. Therefore, one can calculate the present day abundance of an FCP with a given mass and interactions quite precisely. Our motivation for bulk matter search of FCPs is based on the possibility that if they existed in the early universe, they may have a nonnegligible abundance today.

Chapter 3

Different Types of FCP Searches

There are different ways to look for FCPs. Searches have been made using accelerators, cosmic rays [1] and in bulk matter [2], [3]. Searches in bulk matter fall into two classes: those that attempt to concentrate the FCPs before the search [4] and those that directly search through all of a bulk matter sample [5], [6]. We prefer the direct bulk matter search because it is difficult to make a reliable estimate of the efficiency of the pre-concentration method. In this chapter, we give a brief description of the different methods that were used to look for FCPs.

3.1 Accelerator Searches

The quark model with fractional charge quarks was initially regarded simply as a way of explaining the data and not necessarily as having any direct physical basis. In spite of this, the search for free quarks soon started and was pursued with increasing interest both as the model gained wider acceptance and as larger accelerators enabled the production of heavier particles. Some of the early experiments are summarized in Tables [3.1] and [3.2].

Different accelerator searches consist of hadronic reactions, i.e. heavy ion and $p\bar{p}$ collisions, deep inelastic scattering and electron-positron annihilations. In the following these will be described briefly. It is important to know the uncertainties involved in this type of search. First, the center of mass energy available in an

group	charge ($\frac{e}{3}$)	Mass (GeV)	energy	beam	X-SECT (cm^2)
DELPHI(97) [8]	± 2	$45-84$	$130-172$	e^+e^-	$< 1.3 \times 10^{-36}$
CDF (92) [9]	$+2$	250	1800	$p\bar{p}$	$< 2. \times 10^{-35}$
Spec (83) [10]	$\pm 1, 2$	< 9	200	μ	$< 1. \times 10^{-36}$
CNTR (80) [11]	$\pm 2, 4$	$1-3$	200	p	$< 2. \times 10^{-10}$
SPEC (78) [12]	± 1	< 20	52	pp	$< 1. \times 10^{-33}$
CNTR (75) [13]	$+1, 2$	< 20	52	pp	$< 1. \times 10^{-35}$
CNTR (74) [14]	$-1, 2$	$4-9$	200	p	$< 5. \times 10^{-38}$
SPEC (73) [15]	$+2, 4$	$4-24$	52	pp	$< 1. \times 10^{-32}$
CNTR (73) [16]	$+1, 2, 4$	< 12	300	p	$< 5. \times 10^{-31}$

Table 3.1: Summary of quark production cross sections from previous accelerator searches.

group	charge ($\frac{e}{3}$)	Mass (GeV)	energy	beam	Flux	
OPAL(95) [17]	± 2	$2-30$	$88-94$	e^+e^-	$< 0.94 \times 10^{-4}$	a
ALEPH (93) [18]	$+1$	$5-40$	$88-94$	e^+e^-	$< 2. \times 10^{-3}$	a
MLEV (87) [19]	$\pm 1, 2$	< 300	320	$p\bar{p}$	$< 2. \times 10^{-4}$	b
UA2 (85) [20]	$\pm 1, 2$	1	540	$p\bar{p}$	$< 6. \times 10^{-5}$	c
CNTR (82) [21]	$\pm 1, 2$	< 14	29	e^+e^-	$< 1. \times 10^{-2}$	a
MRK2 (81) [22]	± 2	$1.8-2$	7	e^+e^-	$< 3. \times 10^{-4}$	a
JADE (80) [23]	$+1, 2, 4, 5$	$2-12$	27	e^+e^-	$< 5. \times 10^{-2}$	a
SPEC (78) [12]	± 1	< 21	52	pp	$< 6. \times 10^{-11}$	d
CNTR (75) [13]	$+1, 2$	< 20	52	p	$< 7. \times 10^{-10}$	d

Table 3.2: Summary of upper limits on the quark fluxes obtained in previous accelerator searches. See text for meaning of a,b,c,d.

accelerator limits the mass of the free quarks produced. Second, the apparent masses of the bound quarks do not yield the masses of the free quarks and therefore the required energy to isolate a quark is not known. Third, we do not have a model that describes the transformation from a quark diagram to a hadronic diagram and therefore there are hadronic uncertainties in interpreting the limits achieved in these searches. Fourth, as we see in Tables [3.1]-[3.2] these limits correspond to different techniques and definitions, raising the question whether we can compare the results. In Table [3.2] the letter that appears adjacent to the quark flux limits corresponds to the flux definition in each experiment as follows.

a. The inclusive quark production cross section ratio to $\sigma(e^+e^- \rightarrow \mu^+\mu^-)$.

b. The ratio of measured free quarks to predicted free quarks if there is no confinement.

c. The probability of fractional charge on nuclear fragments.

d. Quark flux per charge particle.

The following accelerator searches demonstrate the restrictions of the method.

3.1.1 Heavy Ion Reactions

The motivating idea for looking for FCPs using heavy ion reaction is that as the density of nucleons in a system is increased, the quarks and gluons which were confined within individual nucleons may become capable of moving around freely over the whole nuclear volume and form a quark-gluon plasma. Such a phase may have existed during the early stages of the Universe when the temperature was high. The most likely way of producing it now is through heavy ion collisions. Once the quark-gluon plasma is produced the hope is that either isolated quarks or nuclei containing an extra quark might escape.

The Plastic Detector Experiment

Experiments with emulsions exposed to cosmic rays have suggested that some secondaries [24] have larger than usual interaction cross section. These secondaries became known as the anomalous events [25]-[26]. Motivated by these anomalous events a group at UC at Berkeley [27] measured the charges of secondaries in heavy ion collisions in order to determine if they are third integral. The technique used the fact that when particles of charge Z pass through a thin sheet of CR-39 plastic track detector the size of the subsequently produced etch pit is a monotonic function of Z. The resolution of a single measurement on Z was ± 0.23, so with successive measurements of 16 etch pits per track a statistical accuracy of ± 0.06 was achieved. The detector consisted 400 sheets of plastic, each with a thickness of $640\,\mu$m. The detector was exposed to a beam of 1.85 GeV/nucleon argon ions from the Berkeley Bevelac. Some 1437 argon tracks were followed through the stack which resulted in 248 projectiles of charges with $10 < Z < 17$. With the assumption that the secondaries have the same velocity as the incident beam ions, the distribution of measured charges was consistent with a set of Gaussians centered on integers and with the expected width. All but one of the secondaries were within 4 standard deviations of an integer. The estimated charge for the remain track was 11.23 ± 0.04 but it could have been a charge of 11 with a velocity 2% lower than that of the beam. To obtain a sample enriched in anomalous events, a further 747 secondary tracks were measured within 1.7 cm of the primary interaction point. Again no one or two third integer charges were observed. Finally, a search was made of 32 secondaries that interact a second time within 1 cm of the original production point and again no one or two third integer charges were observed. The experiment thus set a 95% confidence limit of $< 3 \times 10^{-3}$ for the fraction of secondaries having one or two third integer charge.

The Čherenkov Experiment

Barwick, Musser and Stevenson [28] have looked for fractionally charged secondaries from the interaction of an argon beam at 1.8 GeV/nucleon. Their technique involves the use of a series of 14 Čerenkov detectors of thickness between $0.35 - 1.3$ cm. Since

the Čerenkov light output for particles above threshold is proportional to the square of their charge, this system can detect charge changing interactions and is then sensitive to the projectile fragment with the largest charge. The charge resolution of individual detectors for the argon beam varied from $0.15 - 0.25$ for the thickness and thinnest counters. The observed resolution of the system for charge 17 secondaries was 0.07, increasing to 0.1 at charge 14. By demanding that the primaries interact in one of the first two Čerenkov detectors and that the leading secondary pass through the rest of the system without further interaction, Barwick *et al.* [28] accepted 22000 secondaries with charges $14 - 17\frac{2}{3}$. The 90% confidence limit on fractional charge production in this range is less than 10^{-4}.

The Emulsion Experiment

Bloomer *et al.* [29]. have looked for fragments with a charge of $\frac{4}{3}$,$\frac{8}{3}$ among 1179 measured secondaries of charge $1 - 3$ from the interaction of approximately an energy of 1.88 GeV/nucleon iron beam in an emulsion. The charges of the tracks were estimated to a precision of ± 0.07. Those that were inconsistent with integer numbers were remeasured leaving at most one candidate consistent with any of the third integral values. If anomalous events described above were produced among such low charges at the typical optimistic estimated rate of 6% and if they had fractional charge, then 11 anomalous events should have been seen. However anomalous events were not observed. Note that although the last three experiments described looked for anomalous events with fractional charge there was no evidence for this.

3.1.2 Hadronic Production

The CDF Collaboration

A search for massive stable particles with fractional charges of $Q = \frac{2}{3}$,$\frac{4}{3}$ in a $p\bar{p}$ collision at center of mass energy of $\sqrt{s} = 1.8\,\text{TeV}$ was carried out using the collider detector at Fermilab based on integrated luminosity of $3.54\,\text{pb}^{-1}$ [9]. Particles are considered stable if their life time is long enough to pass through the detector before they decay i.e. $\gamma\tau \geq 10^{-7}\,\text{s}$. The Collider Detector at Fermilab (CDF) considered

pair production of FCPs via the gluon fusion and quark-antiquark annihilation. The distinguishing characteristics of such particles are high transverse momenta, velocities that are lower than ordinary high momentum particles and muon-like penetration of matter. The transverse momenta were characterized by distributions which peak at about one half of the particle mass. Although these particles are strongly interacting they can penetrate a considerable amount of material with relatively little loss of energy. CDF is a general purpose 4π detector with a 1.4 T solenoidal magnetic field. The detector combines electromagnetic and hadronic calorimeters in a projective tower geometry with charged particle tracking. Of particular interest are the scintillation counter arrays which signaled an inelastic collision, the vertex time projection chamber (VTPC) which determined the interaction point, the central tracking chamber (CTC), the central hadron calorimeter and the central muon chamber. The acceptance was defined as the probability of an event having at least one particle with transverse momenta greater than 25 GeV/c in the signal region. There is an increase in acceptance as the mass increases since the β distribution shifts to lower values in addition to the average transverse momentum (p_T). Since the track momenta were reconstructed assuming $Q = 1$, the transverse momenta cut of 25 GeV/c became an actual p_T cut of 16.7 GeV/c for $Q = \frac{2}{3}$ particles and 33.3 GeV/c for $Q = \frac{4}{3}$ particles. The amount of energy deposited in the calorimeter depended upon the charge of the object; so $Q = \frac{2}{3}$ particles of a given mass and time of flight deposit less energy than a similar $Q = 1$ particles whereas $Q = \frac{4}{3}$ particles deposit more energy. Because of the penetrating characteristic of the massive FCPs, the data set used consisted of events containing high p_T muons. The muon trigger required hits in the scintillation counter arrays indicative of an inelastic collision and a track above 11 GeV/c in the CTC which loosely matched a track segment formed from hits in the muon chamber. Additional off-line cuts were used to refine the data sample. Events with multiple interactions, as identified by the VTPC were removed. The vertex position along the beam axis was required to be within 60 cm of the detector center. The penetrating track was required to have $p_T > 16.7$ GeV/c and to match a track segment in the muon chamber to within 10 cm in the drift direction. The final cut was the required time to reach the hadron calorimeter $t_{arrival} > 5.4$ ns late compared to $\beta = 1$ particles.

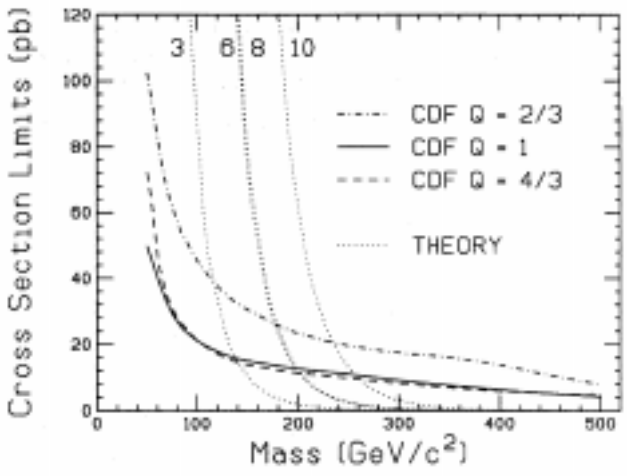

Figure 3.1: The cross section upper limit (95% C.L.) for the pair production of stable charged fermionic colored particles as a function of mass for $Q = 1Q = 2/3Q = 4/3$. Also are shown the theoretical cross sections for the production of fermionic color triplet (3), sextets (6), octets (8) and decuplets (10).

Figure [3.1] gives the resulting 95% confidence level upper cross section limits on the production of stable charged colored particles. Knowledge of the theoretical cross sections allows one to set limits on the masses of the particles produced with these cross sections charges. Charge $\frac{2}{3}$ objects produced with masses between $50\,\mathrm{GeV/c^2}$ and $116\,\mathrm{GeV/c^2}$ are excluded as are charge $\frac{4}{3}$ objects with masses between $50\,\mathrm{GeV/c^2}$ and $140\,\mathrm{GeV/c^2}$ at the 95% confidence level. Interactions of these FCPs could weaken the cross section limits by a factor of $1.5 - 4.0$ where a factor of 4.0 would lower the mass limits by $30 - 40\,\mathrm{GeV/c^2}$.

3.1.3 Electron-Positron Annihilation

Hadronic production in electron-positron annihilation is well described in the Feynmann diagram in Figure [3.2]. The intermediate virtual photon couples to the quark-antiquark which produces jets of hadrons. Neglecting higher order QCD contributions, the ratio of the cross section for this process to that of muon pair production

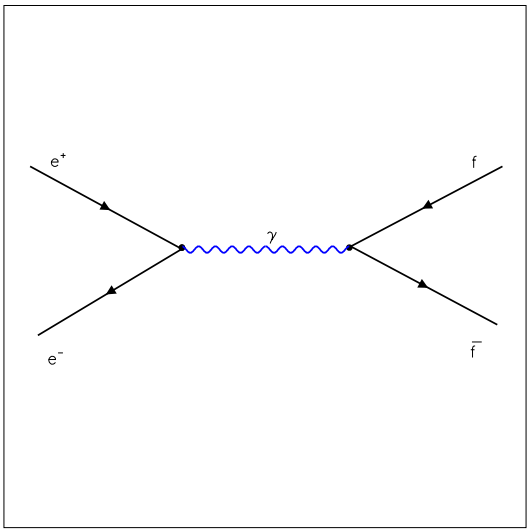

Figure 3.2: The lowest order Feynman diagram for $e^+e^- \longrightarrow f\bar{f}$

is

$$R_Q = \frac{\sigma(e^+e^- \longrightarrow q\bar{q})}{\sigma(e^+e^- \longrightarrow \mu^+\mu^-)} = 3\sum {q_i}^2 \tag{3.1}$$

where q_i^2 is the charge of the i^{th} quark flavor. For energies below the $t\bar{t}$ mass, we expect $R_Q = \frac{11}{3}$. Electron-positron annihilation can produce quark-antiquark pairs either exclusively or inclusively. The exclusive production of quark-antiquark pairs ($e^+e^- \longrightarrow q\bar{q}$) leads to collinear two jet events.

The inclusive production of quark-antiquark pairs ($e^+e^- \longrightarrow q\bar{q}X$) produces quarks together with ordinary particles inside a jet. No evidence of free quarks has been found in e^+e^- annihilation experiments. In the following, a few typical searches are described in detail.

The DELPHI Collaboration

A search for long lived heavy charged particles produced in electron-positron annihilation with center of mass energies of $\sqrt{s} = 130 - 136, 161$ and 172 GeV has been performed using the data taken by the DELPHI experiment at LEP [8]. The search was based on the particle identification provided at the Time Projection Chamber (TPC) and the Čerenkov Ring Imaging detector (RICH). The search for heavy particles with mass above 45 GeV/c^2 was based on ionization loss measurements in the main tracking device of DELPHI and the fact that no Čerenkov photons were expected in the gas or liquid radiator. The combination of the TPC and the RICH detectors allowed for an efficient detection of these particles due to the small background from ordinary matter particles. The data taken in 1995 corresponded to a total integrated luminosity of 5.9 pb^{-1} at center of mass energies of $130 - 161$ GeV and 9.9 pb^{-1} at 172 GeV. The event selection was mainly based on the TPC and optimized for both both low and high multiplicity events. Events with initial state radiation and resonant Z were kept in the sample. Tracks were selected if their impact parameter was less than 5 cm in the transverse plane and less than 10 cm in the longitudinal direction. Each event was divided into two hemispheres according to the thrust axis calculated from charged and neutral particles. The total momentum of all the particles in each hemisphere was required to be more than 10 GeV/c. An event was accepted if it had at least one charged particle with momentum above 5 GeV/c reconstructed on the basis of the TPC and it was lying inside the Barel RICH with acceptance of $|cos\theta| < 0.68$ where θ is the polar angle. To remove cosmic ray muons tighter cuts were applied on the impact parameter: 0.15 cm in the transverse and 1.5 cm in the longitudinal directions for events with two tracks, at least one of each had one or more associated hits in the barrel muon chamber. Thus, 2068 events for the $130 - 161$ GeV data set, 1795 events for the 161 GeV data set and 1441 for the 172 data set were selected. The analysis was optimized to select high mass particles with charges of $\pm\frac{2}{3}$ and high β. To insure a reliable measurement of the normalized ionization loss $\langle dE/dx \rangle$ in the TPC, at least 80 wire signals out of maximum 192 were required. The average resolution for particles with momenta above than 5 GeV/c was better than %10. The ionization loss was normalized to that of the minimum ionizing

particle. It was calibrated on a run-to-run basis and cross checked with identified particles in the RICH detector. Tracks were selected if they had no associated photons in the gas RICH and the particles had momenta above 15 GeV/c with ionization loss below the expected ionization for proton by more than 0.3 units. Upper limits of 95% confidence level were derived on the cross section for heavy long lived pair produced charge $\pm\frac{2}{3}$ particles in the range of $0.4 - 2.3$ pb for masses from 45 to 84 GeV/c^2.

3.2 Cosmic Ray Searches

Cosmic ray experiments can claim having discovered the positron, the muon, the pion and strange particles. Thus, it is not surprising that quark searches have been performed in cosmic rays as well. The quarks could be either part of the primary cosmic ray flux or produced as secondaries in the interactions of very high energy cosmic rays with the upper atmosphere. The cosmic ray experiments described below were capable of measuring the charge of any incident quarks.

3.2.1 FQS

The FQS experiment [30] made use of the same apparatus that used to look for quarks in e^+e^- annihilations but with the PEP storage rings turned off. A total exposure of 2.3×10^6 s was obtained; for about one third of the data the apparatus was in the PEP shielding tunnel while for the remainder it was outside but adjacent to the tunnel. The apparatus was sensitive to cosmic rays at zenith angles of $45^0 - 90^0$. A total of $\sim 10^7$ triggers were obtained with the requirement that there was at least one hit of pulse height greater than $I_0/30$ in two specified scintillator planes. The charge resolution was $\pm 3.5\%$ and tracks with measured charge less than 0.8 were regarded as candidates for quarks. There were 271 of these during the first third of the exposure. After a series of cuts to remove various backgrounds however, there was no evidence for particles of either charge $\frac{1}{3}$ or $\frac{2}{3}$. The resulting 90% confidence limit on the flux of quarks of either charge $\pm\frac{1}{3}$ or $\pm\frac{2}{3}$ in cosmic rays was $3 \times 10^{-9}\,\mathrm{cm^{-2}sr^{-1}s^{-1}}$.

3.2.2 The Japanese Magnetic Monopole Experiment

A Tokyo group [31] has operated a cosmic ray telescope 250 m underground to look for magnetic monopoles or for FCPs by measuring the velocities and energy losses for isolated tracks. The telescope consisted of three pairs of cross scintillators, with effective cross sectional area of 2.5 m × 2.5 m. The depth of the apparatus was 80 cm and together with iron supporting plates corresponded to a thickness of 3.5 radiation lengths. Each scintillator was viewed by a photomultiplier at each end. A truncated mean of the six pulse heights was used to obtain the dE/dx estimates for tracks. The requirement for accepted pulses restricted the sensitivity of the experiment to $dE/dx > 0.2$. The time resolution of ± 0.3 ns enabled the particle velocities to be determined via their time of flight and a distinction between upward and downward going tracks. For nonrelativistic particles this required their mass to be $\geq 10^{10}/\beta^4$ MeV. The experiment ran for 2361 h. Events with more than 1 track were rejected. The majority of the 3×10^6 accepted tracks were consistent with being relativistic muons. Based on calculated the energy loss of particles with different charges, the sensitivity of the experiment was such that a limit of 6×10^{-13} particles $cm^{-2}sr^{-1}s^{-1}$ and β in the range $3.5 \times 10^{-4} - 0.4$ for particles of charge $\frac{1}{3}$ or β of $6.0 \times 10^{-4} - 0.4$ for particles of charge $\frac{1}{3}$ was obtained. They also provided a limit of 2×10^{-12} particles $cm^{-2}sr^{-1}s^{-1}$ for relativistic charge $\frac{2}{3}$ particles. All these values included in the calculated acceptance of the apparatus the possibility of upward going particles being detected, as well as downward ones.

3.2.3 The McCusker Experiment

McCusker's report [32] in 1969 claimed that quarks have been observed in air showers using cloud chamber detectors. His data suggested phenomena in energetic showers initiated by primary cosmic rays with energy over than 10^5 GeV which corresponded to anomalously large transverse momenta. The quark concept suggested a mechanism for the generation of such phenomena. A single proton at the top of the atmosphere in the energy range $10^3 - 10^7$ GeV will generate an electromagnetic cascade which at sea level produces an average number of electrons approximately equal to the energy

in GeV divided by 10. At sea level a good approximation to the electron number density in the interval $1 < r < 200$ m from the shower axis is given by

$$\rho(N, r) = (aN/r)e^{(-r/b)} \tag{3.2}$$

where ρ is the density of electrons per square meter, N is the total number of electrons, $a = 2 \times 10^{-3}$, r is the distance in meters and $b = 60$ m. At any height, the average density at a given r increases about linearly with energy. Therefore, using Eq. (3.2) we find that a primary of 10^3 GeV will seldom produce more than 1 electron shower in units of particle/m^2 at sea level, even near axis, a primary of 10^5 GeV will on average produce $10 - 100$ particle/m^2 within 1 m of the axis.

The consequence of this for quark searches is that a counter telescope of about one square meter area at sea level, which is sensitive only if no more than one particle strikes it within its time resolution would be adequately sensitive to quarks produced by 10^3 GeV protons but virtually insensitive to quarks produced by primaries 10^5 GeV, assuming that quarks generally lie in the core.

The sea level lateral distribution of quarks from the shower axis is given by

$$r_q \approx \frac{1.5 \times 10^4}{m_q^2(\mathrm{GeV}^2)}\mathrm{meters} \tag{3.3}$$

Thus a quark of 100 GeV rest mass will lie about 1 m from the core. The main idea is that quarks having $m_q > 50\,\mathrm{GeV/c^2}$, would often be found accompanied by a dense flux of shower particles. McCusker introduced this new perspective of quark search which has subsequently led to the most stringent limits on the existence of very massive quarks ($m_q > 25\,\mathrm{GeV/c^2}$).

The McCusker experiment utilized a trigger consisting of three arrays of Geiger counters each with a 110 cm^2 effective area arranged in a horizontal equilateral triangle 2 m on a side. This should provide an efficient trigger for air shower cores corresponding to primary cosmic ray energies in excess of 10^6 GeV. In addition, it included four cloud chambers each with a cylindrical volume of dimensions 5 cm high and 30 cm base diameter which were oriented with their cylindrical axes horizontal

and positioned between and below the trigger counters. In several months of operation, 5500 air shower events were photographed and analyzed resulting in 5 quark candidates among the 60000 tracks that were found in the scanning. If quarks were found by the McCsker group then their flux would have been $10^{-7}\,(\mathrm{cm^2 srsec})^{-1}$. However, their identification depended critically on the correlation between track age and bubble size, a correlation the authors calculated but did not measure for the relevant set of chamber operating conditions. Their interpretation has been sharply challenged by the Argonne bubble chamber group [33]. Their flux was in complete disagreement by orders of magnitude with many convincing negative results. The combined 90% confidence level on the quark flux from all the subsequents experiment gives

$$\phi < 0.71 \times 10^{-11}\,(\mathrm{cm^2 srsec})^{-1} \text{ for q} = 1/3 \tag{3.4}$$

$$\phi < 1.4 \times 10^{-11}\,(\mathrm{cm^2 srsec})^{-1} \text{ for q} = 2/3 \tag{3.5}$$

In view of the design of later single particle searches which used lead shielding and which were sensitive to several simultaneous particles in the meter square detector, there is now convincing evidence against the existence of fractionally charged cosmic ray quarks at flux levels above $10^{-11}(\mathrm{cm^2 srsec})^{-1}$.

3.2.4 Kamiokande II

The Kamiokande II [34] water Čerenkov detector looked for FCPs $|Q| = \frac{1}{3}$ and $|Q| = \frac{2}{3}$ produced by primary cosmic rays. The Kamiokande II water Čerenkov detector which is 2700 m of water equivalent is located underground in the Kamioka mine 300 km west of Tokyo. The detector is cylindrical steel tank which contains 2400 tons of water viewed by 94820 onein photomultiplier tubes (PMT's) covering 20% of the tank inner surface. The inner detector is surrounded by a 4π steradian water anticounter at least 1.2 m thick, viewed by 12320 onein PMT's. The Kamiokande II detector is able to distinguish FCPs from unit charged particles by the emitted Čerenkov light intensity. The number of Čerenkov photons per unit path length and unit wavelength emitted

by a charged particle of $\beta > 1/n$, $d^2N/dxd\lambda$, is given by

$$\frac{d^2N}{dxd\lambda} = 2\pi|Q|^2\alpha\left(1 - \frac{1}{(n\beta)^2}\right)\frac{1}{\lambda^2} \tag{3.6}$$

where n is the refraction index of water, β is the velocity of the particle relative to the light velocity and α is the fine structure constant. Equation (3.6) indicates that the number of Čerenkov photons associated with charged particles is proportional to $|Q^2|$. Therefore, the total Čerenkov emissions of $|Q| = \frac{1}{3}$ and $|Q| = \frac{2}{3}$ particles, $(d^2N/dxd\lambda)_{(|Q|=\frac{1}{3})}$ and $(d^2N/dxd\lambda)_{(|Q|=\frac{2}{3})}$ are related to the total Čerenkov emission of normal ($|Q| = 1$) cosmic-ray muons, $(d^2N/dxd\lambda)_\mu$ by the factors 1/9 and 4/9 respectively. Figure [3.3] shows the correlation of path length of cosmic ray muons that penetrated the Kamiokande II detector with the total yield of Čerenkov light measured in number of photo-electrons. The total number of photo electrons can be written as

$$(P_{total})_\mu \approx (1000L)_{p.e.} \tag{3.7}$$

where L is the path length of muons in meters. Charged particles that penetrate the detector with a path length larger than 10 m and with a total of photoelectrons yield less than 7000 p.e. might be considered to be FCPs. Such events were searched for in the photoelectron range 750 p.e. $< P_{total} <$ 2000 p.e. for $|Q| = \frac{1}{3}$ and 3000 p.e. $< P_{total} <$ 7000 p.e. for $|Q| = \frac{2}{3}$. Data was collected for 1009 days corresponding to 7.1×10^7 events. Most of the events were penetrating muons with a short path length in the detector or muons which stopped in the detector. After removing those events, 1945 events with $3000 p.e. < P_{total} < 7000 p.e.$ and 2863 events with $3000\, p.e. < P_{total} < 7000\, p.e.$ remained. Most of the remaining events were muons with more complicated behavior such as muons with appreciable multiple scattering (70%), muons with short path length accompanied with hadronic interaction in the detector (20%) and those that stopped in the detector (10%). No fractional charged event was observed. The 90% confidence limit upper limits on the fluxes (ϕ) can be calculated from the detection area $S = 130\, m^2$, observation time $T = 1009$ days and

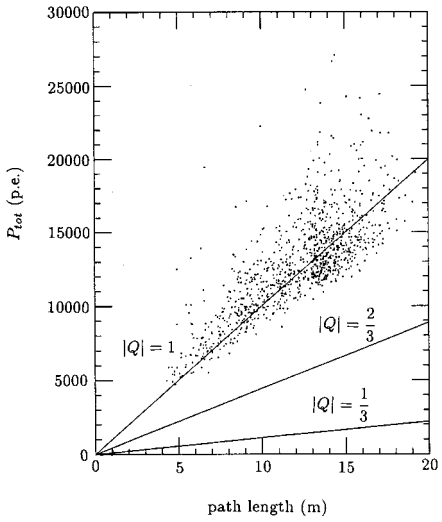

Figure 3.3: Correlation between the total Čerenkov light yield measured in photoelectrons and the path of radiating particles in the detector. The scattered points are for a selected, reconstructed sample of muons $|Q| = 1$, and the solid lines for $|Q| = \frac{1}{3}$ and $|Q| = \frac{2}{3}$ particles.

selection efficiency ϵ. The results are

$$\Phi(|Q| = \frac{1}{3}) = 2.1 \times 10^{-15} cm^{-2} s^{-1} sr^{-1} \quad (3.8)$$

$$\Phi(|Q| = \frac{2}{3}) = 2.3 \times 10^{-15} cm^{-2} s^{-1} sr^{-1} \quad (3.9)$$

$$(3.10)$$

These upper limits are the most stringent limits obtained from cosmic ray searches on FCPs flux. A summary of previous cosmic ray searches results is given in Table [3.3].

3.3 Bulk Matter Searches

Accelerator and cosmic ray [1] searches put an upper limit on the mass of the FCP produced contrary to bulk matter searches [2], [3] in which you can look for heavier masses and a larger mass range. The disadvantage of the bulk matter search technique

Collaboration first author	charge ($\frac{e}{3}$)	Φ	Quark i.d.
Kamiokande II [34]	1	$< 2.1 \times 10^{-15}$	Čerenkov
	2	$< 2.3 \times 10^{-15}$	Čerenkov
FQS [30]	1, 2	$< 3 \times 10^{-9}$	$\frac{dE}{dx}$+ TOF
Mashimo [31]	2	$< 2 \times 10^{-12}$	$\frac{dE}{dx}$+ TOF
	1, 2	6×10^{-13}	$\frac{dE}{dx}$+ TOF
Bhat [35]	*any*	2×10^{-11}	Delayed air shower
Wada [36]	4	2×10^{-9}	$\frac{dE}{dx}$
	1.2	2×10^{-10}	$\frac{dE}{dx}$
McCusker [32]	any	$\approx 10^{-11}$	Images from cloud chambers

Table 3.3: Summary of previous cosmic ray results. The flux Φ is quoted in particles $cm^{-2}s^{-1}sr^{-1}$. Only McCusker [32] group claimed discovery of FCPs. Subsequent experiment reported null results.

is that the distribution of FCPs in matter is not known. In order to set the density of FCPs in the universe the same way it is done for the primordial elements we will need to understand the geochemistry of FCPs.

In both types of bulk matter searches, the methods of measuring the electric charge is based on the application of an electric field. The electric force on the sample is measured by observing the changes in the position of the sample which allows the value of the charge to be determined.

3.3.1 The Levitometer Technique

The earliest bulk matter searches [2] used the magnetic levitation technique to look for free quarks. The principle of the technique is to suspend an object by a magnetic force preferably in vacuum and to employ an alternating electric field on it to measure its charge. There are two methods of magnetic levitation ferromagnetic and diamagnetic. In the ferromagnetic levitation method the object is typically a 0.25 mm diameter steel ball or a nonmagnetic material coated with steel. The object is levitated at room temperature by means of a shaped magnetic field. In the diamagnetic method, the sample is a small superconducting sphere levitated in vacuum at a temperature of 4 K,

by means of superconducting coils. In the diamagnetic method, the magnetic field provides stable levitation but in the ferromagnetic levitation case additional coils and a feedback technique are used to achieve stability. The feedback mechanism consists of a light source creating a shadow of the object on a photodetector. When the object falls (rises), the shadow covers a smaller (larger) fraction of the sensitive region of the photodetector. With an appropriate amplifier the magnetic field is increased (decreased) [37] and the object is pushed upward (downward). To determine the charge of the object it is assumed that the object is levitated by a shaped magnetic field such that it is located at a local minimum of the field. Once the object is levitated, a uniform, transverse, oscillating electric field forces the object to execute harmonic motion. The force equation for this object with charge Q is

$$m\ddot{x} + \alpha\dot{x} + \beta x = QE sin\,\omega t. \tag{3.11}$$

where α is the damping coefficient, β is the restoring force parameter and ω is the driving frequency of the system.

The steady state solution to Equation (3.11) is given by

$$A = A_0 sin(\omega t - \phi),$$

where the amplitude of oscillation, A_0, is

$$A_0 = \frac{QE}{\sqrt{(\alpha\omega)^2 + (\beta - m\omega^2)^2}}. \tag{3.12}$$

At resonance, this amplitude becomes

$$A_0 = \frac{QE}{\alpha\omega}. \tag{3.13}$$

Since E, α, and ω are known parameters and A_0 is measured, we solve for Q to obtain

$$Q = \left(\frac{\alpha\omega}{E}\right) A_0. \tag{3.14}$$

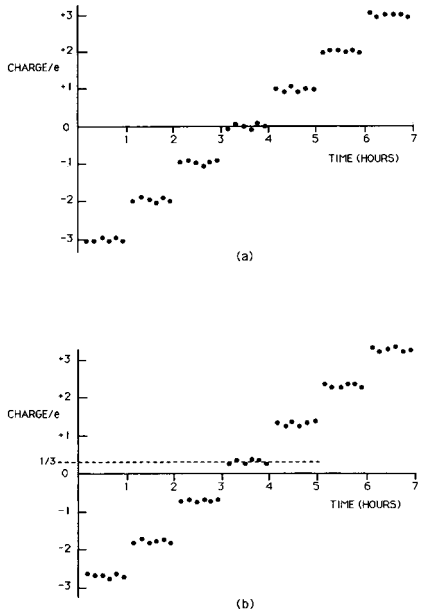

Figure 3.4: Typical appearance of data from levitation experiment, showing effect of removing single electrons by exposure to weak ultraviolet light. Each point is calculated from the average oscillation amplitude of the levitated sample over a period of 10 min. (a) Ideal appearance of data for zero residual charge and no systematic zero error, giving an oscillation amplitude passing through zero. (b) Data offset by fractional residual charge (or by zero shift produced by "patch effect")

To check for the presence of a fractional charge, one begins with a negative charge on the sample, and progressively removes electrons by illumination with ultraviolet light or with a movable radioactive source. Then the oscillation amplitude $A_0(t)$ is plotted as a function of time as shown in figure 3.4a. If the object did not contain a free quark, then $Q = n$ and $A_0(t)$ would pass through zero. On the other hand, If the object contained a FCP $A_0(t)$ would never pass through the value zero. The presence of fractional charge $\frac{1}{3}$ or $\frac{2}{3}$ would give an offset $\pm\frac{1}{3}$ as illustrated in figure 3.4b. Typically 10 hours are needed in order to reduce the statistical errors to less less 0.05 which is sufficient to exclude the possibility of an offset of 0.33 arising as a chance of fluctuation in the data.

3.3.2 Electric Forces on a Levitated Object

Problems arising from several sources of systematic errors are capable of producing a shift of sufficient magnitude to simulate the presence of fractional residual charges of $Q = \frac{1}{3}$. The first simplifying assumption in discussing the levitation method is to consider a uniform electric field between the capacitor plates whereas in practice there is a nonuniform electric field that can give rise to spurious residual charges. In the following, we consider the different electric forces that can contribute to this spurious effect.

The Polarization Force: A conducting sphere in a nonuniform electric field experiences a polarization force, F_{pol}, which is the induced dipole force on the conducting sphere.

$$F_{a-pol} = \alpha E^a \frac{\partial E^a}{\partial x}, \tag{3.15}$$

where the polarizability, α is given by $4\pi\epsilon_0 r^3$, and E^a is the applied electric field. This force does not introduce a spurious charge effect since F_{pol} is quadratic in E^a and hence would produce a motion at twice the resonance frequency of E^a. The detection system can select only the resonance frequency since this frequency is enhanced or other frequencies can be filtered out.

The Patch Force: Contaminants deposited on the field plates or local irregularities at the Fermi level of the plates (patches) could lead to a static field contribution, E^v, to the total electric field.

$$F^v = 4\pi\epsilon_0 r^3 \frac{\partial E^v}{\partial x} E^a, \tag{3.16}$$

Clearly F^v adds to the force QE^a producing a total force of

$$F = (Q + 4\pi\epsilon_0 r^3 \frac{\partial E^v}{\partial x}) E^a, \tag{3.17}$$

The second term simulates a spurious charge given by

$$Q_v = 4\pi\epsilon_0 r^3 \frac{\partial E^v}{\partial x} \tag{3.18}$$

The potential differences corresponding to the patch fields have typical values of tens of millivolts. While these fields are small with respect to the applied field, they make a nonnegligible contribution to the residual charge calculation. Therefore, the apparent residual charge must be determined and subtracted from the measured value of Q to ascertain the true charge on the object. This is done by taking balls with the same radius and measuring them successively in conditions where the patches do not change. If one ball contains a quark and the subsequent one does not, then the difference in their residual charge must be $\pm\frac{1}{3}$. Then these runs, where different balls of the same radius are compared, are intermixed with runs on balls of a different radius. Because the residual charge depends on r^3, this information confirms the normalization of the patch effect.

The Unbalance Force: The average potential difference between each capacitor plate with respect to the walls of the levitation chamber does not vanish to a good precision since in practice the square wave oscillations of the electric field are not perfectly symmetric. This is due to a difference in the switching times of the potential on the plates.

This non zero average potential is equivalent to a time independent potential above zero applied to the plates, and due to edge effects produces a gradient, $\partial E^u/\partial x$, at the position of levitation. This yields an unbalance force given by

$$F^u = \alpha E^a \frac{\partial E^u}{\partial x}.$$

However, this gradient is negligible if the plates have a large diameter and a small separation. Therefore, its contribution to a pseudo-fractional charge can be ignored.

The Permanent Electric Dipole Force: The permanent electric dipole moment of the ball couples to the field gradient in a nonuniform field to yield the dipole force

$$F_{dipole} = p_x \frac{\partial E^a}{\partial x}.$$

Because this is also linear in E^a, it would simulate a fractional charge. This force can be estimated by measuring the permanent electric dipole moment of the ball. This is done by creating a known gradient of the applied electric field at the position of

the ball and by measuring the corresponding change in the force acting on the ball. However ensuring that the plates are flat and parallel enough results in ignoring this force. The same conclusion is true for the higher multiple moments.

The Magneto-Electric Force: The alternating electric field produces a torque on an object with a permanent electric dipole moment

$$\vec{T} = \vec{p} \times \vec{E^a}.$$

and therefore tilts the object. The tilting implies a tilting of the permanent magnetic moment of the ball $\vec{\mu}$. This in turns entails a variation of the force on the object since the object moves in a region of a nonuniform magnetic field. If the magnetic field is orthogonal to the electric field applied and the object spins around the z axis, the magneto-electric force is

$$F_{m.e.} = \beta E_x^a \frac{\partial H_x}{\partial x}.$$

and the apparent charge due to this force is

$$Q_{m.e.} = \beta \frac{\partial H_x}{\partial x} \tag{3.19}$$

where β is a coefficient typical for each ball. The apparent charge can be measured for each ball and subtracted to get the real charge of the ball.

3.3.3 The Claim of Positive Results in the LaRue Experiment

The only bulk search experiment ever to claim discovery of FCPs was based on the superconducting levitation of 0.28 mm niobium balls. Their results summarized in three papers [38]-[40] between $1977-1981$ claimed unambiguous evidence of FCP. Full experimental detail is given in the theses of Hebard [41], LaRue [42] and Phillips [43]. This claim was based on the 40 measurements of 13 niobium samples for which it was believed that all systematic errors were taken into account and reduced to levels well below 0.1. Hence they could not account for the observations of values

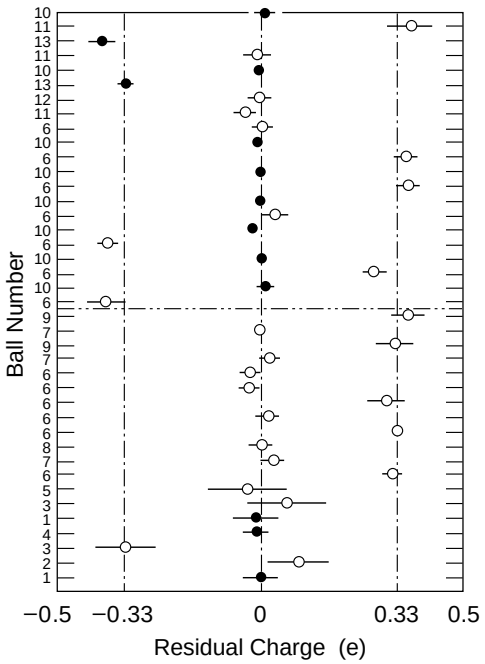

Figure 3.5: Residual charge results for niobium samples, as reported by LaRue *et al* at Stanford. Results are in chronological order from bottom to top.

in the region of $\pm\frac{1}{3}$. Other levitometer experiments [37] [5][44] did not confirm the LaRue results. However these other experiments used ferromagnetic instead of diamagnetic levitation and the original sample was never retested. The results of the LaRue experiment in figure [3.5] showed a number of charge values grouped around zero accompanied by a number of charge values grouped in the vicinity of $\pm\frac{1}{3}$. The author claimed that any conceivable source of error should give a continuous spread of values and thus cannot account for the grouping of the results. However, there were a few difficulties associated with the data. The charge on a given sample did not remain constant; three samples showed fractional charge values and also a zero charge value on repeated measurements. One sample was measured with charges of $\frac{1}{3}$, 0, $-\frac{1}{3}$ which suggest that charge was easily lost and gained between the surface of the sample and the matter it came in contact with between tests. The latter imply that FCPs are not specifically associated with niobium balls but should exist in other terrestrial materials, whereas there was no evidence for FCPs at this abundance in

tests made on steel balls. Another difficulty with the LaRue experiment is the patch effect. This effect is due to a force that results from small electric field gradients arising from impurity patches on the electric field plates. As explained before, these field gradients interact with the induced dipole moment on the sample to imitate a residual fractional charge. These effects can only temporarily and partially be removed by cleaning the plate surfaces since further impurity layers form on the plates and change with time. The magnitude of the effect is inversely proportional to the square of the plate separation; therefore it could be as large as $0.5 - 0.8$ e for a 1 cm plate separation. The effect is also proportional to the cube of the sample diameter hence limiting the sample size to 0.3 mm ($\approx 10^{-4}$g). The result of this effect would appear as a constant charge shift for two successive measurements. Subtraction of successive measurements on different samples would give any difference of residual charge between the two samples. However random fluctuations of $\approx \frac{1}{3}$ occurred due to a large patch field and to investigate this point, measurements were made to check the constancy of the patch field gradient. It was required that the patch remain constant over a period of several days; otherwise the whole sequence of data was discarded. The need to discard data in this way reduced the output to only 40 measurements on 13 samples over a period of about 5 years, making it hard to carry out enough tests to investigate the origin and consistency of the apparent fractional charges. In addition, the need to discard data when the patch varied slightly during the test sequence created a concern about how acceptance decisions were made in borderline cases. To settle this problem a test was suggested but was never carried out, since a number of technical problems arose. Unfortunately no reliable residual charge measurements were possible. Furthermore, there have been concerns that slight misalignments of the electric and magnetic fields and some uncertainties regarding the ball spin could have caused the same systematic errors in the original measurements. Attempts to investigate or reproduce their results failed and LaRue *et al.*modified their claim of observation of fractional charge to evidence for fractional charge [43].

The RAL/IC Levitation Experiment

In 1982 work began in the UK at the Rutheford Appletion Laboratory (RAL) and at Imperial College (IC) London to develop an independent experiment capable of repeating the Stanford observations with lower systematics errors. The RAL/IC [5] experiment analyzed niobium spheres 0.28 mm in diameter that were coated with 0.01 mm of iron in order to allow ferromagnetic levitation. The experiment was carried at room temperature. The samples were levitated in vacuum (so that their charges would not change frequently due to the presence of ions) by a horizontal magnetic field distribution produced by the poles of an electromagnet shaped and positioned to maximize the working volume. Two additional field shaping blocks were positioned to convert the shallow double maximum in the magnetic field (in the x-direction) into a single maximum at the mid-plane. A schematic drawing of the experiment is shown in figure [3.6] A given sample was situated at the mid-plane, where it was stable with respect to displacements in the x- and z-directions, but unstable in the y-direction (vertical). The vertical motion was stabilized by feedback control of the levitation field. A $\pm 2.5\,\mathrm{kV}$ alternating electric field in the x-direction was applied at a frequency adjusted for each sample to the resonant frequency of the x-motion. Typically this was about 1.9 Hz. The plates were capable of sliding in the z-direction relative to the fixed levitation position, to allow investigation of patch effect variations if required. For charge measurements, however, they were always centrally located. Small damping coils outside the plates provided a magnetic restoring force proportional to dx/dt that limited the resonant oscillations to an amplitude proportional to the AC electric force and therefore proportional to the charge on the sample. The z-motion was also damped so that further instabilities were minimized. A weak alternating magnetic field spun the sample at $1-2\,\mathrm{Hz}$ about the x-axis to average out any surface irregularities and any nonaxial components of the intrinsic electric and magnetic dipole moments on the sample.

The transverse magnetic field configuration was chosen to satisfy the criteria (a) that the magnetic and electric axes should be parallel to avoid the additional error that arises when the induced electric and magnetic dipole moments are orthogonal "magneto-electric effect" discussed earlier [37] and (b) that minimum noise level

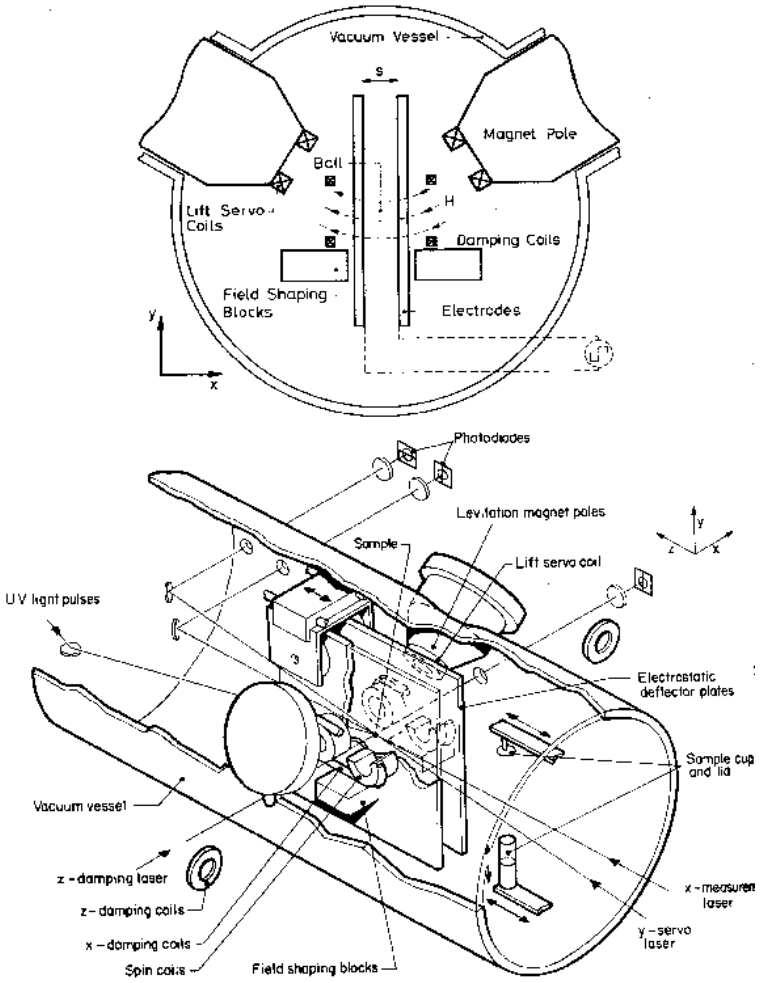

Figure 3.6: RAL/IC levitation system, (Top) Cross section of basic levitation geometry, showing parallel transverse electric and magnetic fields. (Bottom) Three -dimensional view of apparatus, showing laser/photodiode sample position measurement system. The electric deflector plates are 15 cm square and there is a separation of 2.5 cm.

measurements of the ball motion should be made in a direction perpendicular to the direction of stabilization.

The ball motion was measured by means of three laser beams. The shadow of the ball from each were imaged onto a split photodiode to provide separate voltage signals proportional to the displacement in the x, y and z-directions. The ball was inserted into the levitation position by an externally controlled removable cup. Pulses of ultraviolet light of adjustable intensity and duration neutralized the ball from an initial value of $Q \approx -10^6$ to the required starting value of $Q \approx -6$ and then changed the charge on the ball in unit steps to a final value of $Q \approx +6$. Beginning at -6, a maximum of twelve 4 min blocks of data were recorded at each charge level, after which short pulses of UV light were fired until the computer detected a charge change. This process was repeated until the charge reached $+6$. In practice, one test would take between two and twelve hours depending on whether there were any spontaneous charge changes.

The photodiode signals corresponding to the x-coordinate of the ball were processed by a lock-in amplifier and the voltage V corresponding to the oscillation amplitude at the driving frequency were recorded every 4 μs by computer. Every 4 min the data was averaged and the phase of the electric field square wave was shifted by 180° to eliminate a small zero shift arising from stray coupling affects. To minimize vibrational noise data was acquired at night.

The apparent residual charge, Q_r, on a ball was obtained from a least squares fit to the expression $V = k(Q_i + Q_r)$, where Q_i is an integral multiple of e. Fits to second and third order polynomials were also made to check the validity of the linearity assumption. Runs were rejected if spontaneous charge changes prevented the accumulation of sufficient data at each charge level or sufficient number of charge levels to obtain a least squares fit with a statistical error of less than 0.05. In normal runs, the data had a standard deviation of 0.2 after 4 min and 0.02 after 400 m. The RAL/IC [5] experiment also observed that the patch effect appeared to decrease with time. An initial non-zero bias of $0.1 - 0.2$ was present but disappeared after a conditioning period of about two weeks, leaving results centered close to zero with a spread of 0.05. A total of 64 measurements on 46 different samples showed no evidence

of a fractionally charged particle. This corresponded to an upper limit of 600 quarks/g or 10^{-21} quark/nucleon at the 95% confidence level. Because of the larger amount of niobium tested in this experiment compared to the Stanford experiments, the RAL/IC [5] experiment did not confirm the Stanford findings.

3.3.4 The Last Levitometer Experiment

The first search for FCPs in extra-terrestrial materials were carried by W. G. Jones *et al.* [44]. The tests were made on diced samples of the Hoba and Forsyth County iron- nickel meteorites and the Murchison stony meteorite, the latter being iron plated to allow ferromagnetic levitation. The three samples were provided by the British Museum of Natural History in London. Although the levitation technique has in the past used mainly spherical samples, the Jones experiment has been able to test satisfactorily samples which were nonspherical due to mechanical spin that is applied parallel to the electric field. A total of 54 tests, on samples from two iron meteorites (Hoba and Forsyth) and one stony meteorite (Murchison) showed no indication of nonzero residual charge. The total quantities tested were (Hoba) 1.3 mg, (Forsythe) 1.1 mg,(Murchison) 0.4 mg. The apparatus of this experiment was based on the principle developed by Marinelli and Morpurgo [37], with some changes in geometry such as an increase in plate separation and the parallel electric and magnetic fields. The samples had average diameters of $0.2 - 0.3$ mm and were either ferromagnetic or coated with a layer of ferromagnetic material such as iron or nickel about 20 μm thick. The samples were magnetically levitated in vacuum and stabilized horizontally by the field shape and vertically by the feedback control of the field strength which used optical techniques to measure the displacement of the sample. The levitated sample oscillated in response to an alternating ($\approx$ 1Hz) electric field with an amplitude proportional to the charge. The charge was reduced to a small negative value using UV light and then changed in integral steps between -6 and $+6$ over a period of $4-8$ hours, the average oscillation amplitude being measured at each charge level. A least squares fit to the data determined the "residual charge" with a typical statistical error of ± 0.02. Systematic errors associated with asymmetries or irregularities

Group	Material	Mass (mg)	Method	σ_q
LaRue *et al.*(1981) [38]-[43]	niobium	1.1	levitometer	0.093
Marinelli *et al.*(1982) [45]	iron	3.7	levitometer	0.129
Liebowitz *et al.*(1983) [46]	iron	0.72	levitometer	0.001
Smith *et al.*(1985) [5],[7]	niobium	4.7	levitometer	0.05
Jones *et al.*(1989) [44]	meteorite	2.8	levitometer	0.07
Hodges *et al.*(1981) [47]	mercury	0.175	Millikan	0.040
Joyce *et al.*(1983) [4]	sea water	0.051	Millikan	0.037
Lindgren *et al.*(1983) [48]	mercury	0.5	Millikan	0.035
Savage *et al.*(1986) [49]	native mercury	2.0	Millikan	0.040
Mar *et al.*(1995) [6]	silicone oil	1.07	Millikan	0.025

Table 3.4: Summary of stable bulk matter searches. Only LaRue *et al.* [38]–[43] claimed to have observed fractionally charged particles. Subsequent experiments all yielded null results. The last four entries are from the San Francisco State University experiment.

in the sample were eliminated by spinning the samples at $\approx 1kHz$ about the electric field. Spinning prevented permanent electric and magnetic dipole moments oriented in different directions and allowed nonspherical samples to be tested. The only unavoidable systematic error was the "patch effect" discussed earlier. In that apparatus, the effect was in the range of ± 1 and varied less than $0.01\,e/week$. Thus it was easily measured and subtracted by means of periodic tests with a standard sample. No evidence of fractional charges of value $\pm\frac{1}{3}$ or,$\frac{2}{3}$ was found and the number of FCPs per nucleon with 95% confidence level was less than 4.0×10^{-20}.

3.3.5 The Millikan Technique and Summary of Previous Bulk Matter Searches

Table [3.4] summarizes the results from previous bulk matter searches. As we can see most of the experiments tested refined materials besides one levitometer type experiment done by Jones *et al.* which tested meteorites and one Millikan type experiment done by Hodges *et al.* [47] which tested native mercury. Both bulk matter techniques are able to study any unrefined material. In the levitometer method the

solid material is cut to little fragments usually of about 0.3 mm each and in the Millikan technique suspensions are prepared with the interesting mineral as discussed in appendix C. However the Millikan method had improved in recent years due to technological developments discussed in chapter 5. The experiment can be automated which allows achievement of 50 mg a year. In addition, it provides self-calibration of the charge measurements since multiple drops are measured simultaneously. Due to these advantages we prefer to use the Millikan type method.

3.3.6 The San Francisco Millikan Experiment

A classic experiment to measure the charge of a sample is the Millikan experiment. The first automated Millikan experiment was constructed by Hodges *et al.* [47] where automated refers to the measuring technique, data taking and data analysis. They ejected drops with diameter between $7.\,\mu\mathrm{m} - 13.\,\mu\mathrm{m}$ or equivalently drop masses of approximately 8×10^{-8} mg. This experiment tested 0.06 mg of refined and 0.115 mg of native mercury respectively. The principle of the method was as follows. The mercury drops were viewed by appropriately positioned photomultipliers and recorded while falling through air. The velocity of the drops were recorded twice, when the electric field pointed downward and upward $v_{down,up}$. If r is the radius of the drop, η is the viscosity of the air and m the mass of the drop, then the two force equations that govern the motion of the drop are

$$mg = 6\pi\eta r \frac{(v_{E_{\mathrm{down}}} + v_{E_{\mathrm{up}}})}{2}, \tag{3.20}$$

$$qE = 6\pi\eta r \frac{(v_{E_{\mathrm{down}}} - v_{E_{\mathrm{up}}})}{2}, \tag{3.21}$$

These two equations hold provided that the charge q of the drop does not change during the whole measurement. In order to check if a charge change occured two additional measurements of the velocity $v_{E_{const1}}$, $v_{E_{const2}}$ were made with the electric field pointing in the same direction. A selection criteria excluded drops with $\Delta q > 0.3$ defined in Eq. (3.22).

$$\Delta q = 6\pi\eta r(v_{E_{const1}} - v_{E_{const2}}) \tag{3.22}$$

In addition offline tests rejected drops with large velocity residual or drops radius far from the norm. $100,000$ drops were analyzed and $53,973$ survived the rejection criteria which correspond to 0.029 mg of native and 0.013 mg of refined mercury respectively. The conclusion was that the concentration of FCPs in mercury was less than one FCP per 8.43×10^{18} nucleons with 95% confidence level. The technique described above is very valuable because it shows the potential throughput of an automated Millikan experiment.

3.3.7 The Stanford Millikan Experiment

Mar *et al.* [6] have conducted a search for elementary particles with fractional electric charge in silicone oil using an improved Millikan liquid drop method in which they automatically measured the charge on individual drops of about $7\,\mu$m in diameter.

The method is built upon the technique developed in FCPs searches at San Francisco State University [47]-[49] and goes back to the original work of Millikan [50]–[51]. As shown schematically in Figure [3.7], the mechanical part of the apparatus consisted of two flat, circular, stainless steel plates separated by a distance small compared with the plate diameter, the ratio being on the order of 1:16. A device called a dropper produces on demand a spherical drop of silicone oil whose diameter is between $7\,\mu$m and $8\,\mu$m. Early in the experiment, drops that were $7.6\,\mu$m in diameter were produced. But 94% of the drops studied had a diameter of $7.1\,\mu$m.

The drops fell vertically through a small hole in the upper plate through the space between the plates and then left the apparatus through a small hole in the lower plate. The entire apparatus was in dry air at atmospheric pressure and room temperature. The frictional resistance of the air brought a $7.1\,\mu$m drop to terminal velocity within a few thousandths of a millimeter. The terminal velocity for a neutral drop of this size was 1.35 mm/s. The frequency of drop production was set at 0.6 Hz. A $7.1\,\mu$m diameter drop of silicone oil has a mass of $1.71 \times 10^{-4}\,\mu$g and contains 1.03×10^{14}

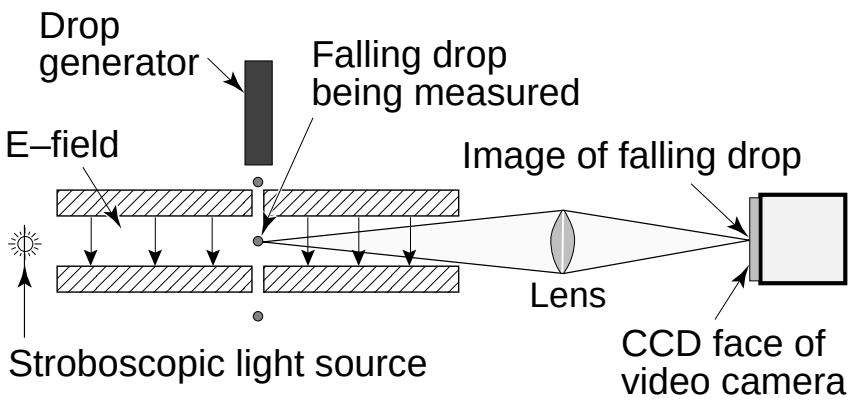

Figure 3.7: Schematic drawing of the fractional charge search apparatus which is not to scale.

nucleons.

Between the plates there was a uniform, vertical electric field. The field strength changed in time with a square wave oscillation amplitude of 1.4×10^6 V/m. If the drop had a nonzero charge, the terminal velocity differed according to whether the electric field reinforced or opposed the gravitational force. By the methods described in the following, the terminal velocity in both situations were measured and the charge on the drop was calculated.

Continuing to refer to Figure [3.7], a stroboscopic lamp illuminated the drop twice for each electric field orientation and a lens imaged the shadow of the drop onto a charge coupled device (CCD) video camera. Thus, the position of the shadow of the drop on the CCD surface measured the position of the drop in real space when the stroboscopic lamp flashed. A desktop computer used the output of the CCD camera to calculate the terminal velocities and the diameter and charge of the drop. The computer also controlled the experiment and stored the data. The search tested through 1.07 mg of oil and found no drops that contained a fractional charge particle with $\pm \frac{1}{3}$e or $\pm \frac{2}{3}$. Therefore, with 95% confidence, the concentration of isolated quarks with these charges in silicone oil was less than 1 particle per 2.14×10^{20} nucleons.

Chapter 4

Theory of the Automatated Millikan Experiment

In our automatated Millikan Experiment we studied silicone oil. In order to determine the charge on the oil drop, consider a drop falling in the air under the influence of gravity and in the presence of an alternating vertical electric field that switches between two discrete states, up and down. Since the drop falls in air, according to Stokes Law, the air exerts a resistive force on the drop causing it to reach a terminal velocity.

The two equations of motion that govern the motion of the drop are:

$$mg + qE_{\text{down}} = 6\pi\eta r v_{E_{\text{down}}}, \tag{4.1}$$

$$mg - qE_{\text{up}} = 6\pi\eta r v_{E_{\text{up}}}, \tag{4.2}$$

where m is the mass of the drop, g is the acceleration due to gravity, q is the electric charge on the drop, $E_{\text{up,down}}$ is the magnitude of the applied electric field depending on whether the field points up or down respectively, η is the dynamic viscosity of air, $v_{E_{\text{up}}}$ and $v_{E_{\text{down}}}$ are the terminal velocities of the drop associated with the direction of the electric field and r is the radius of the drop.

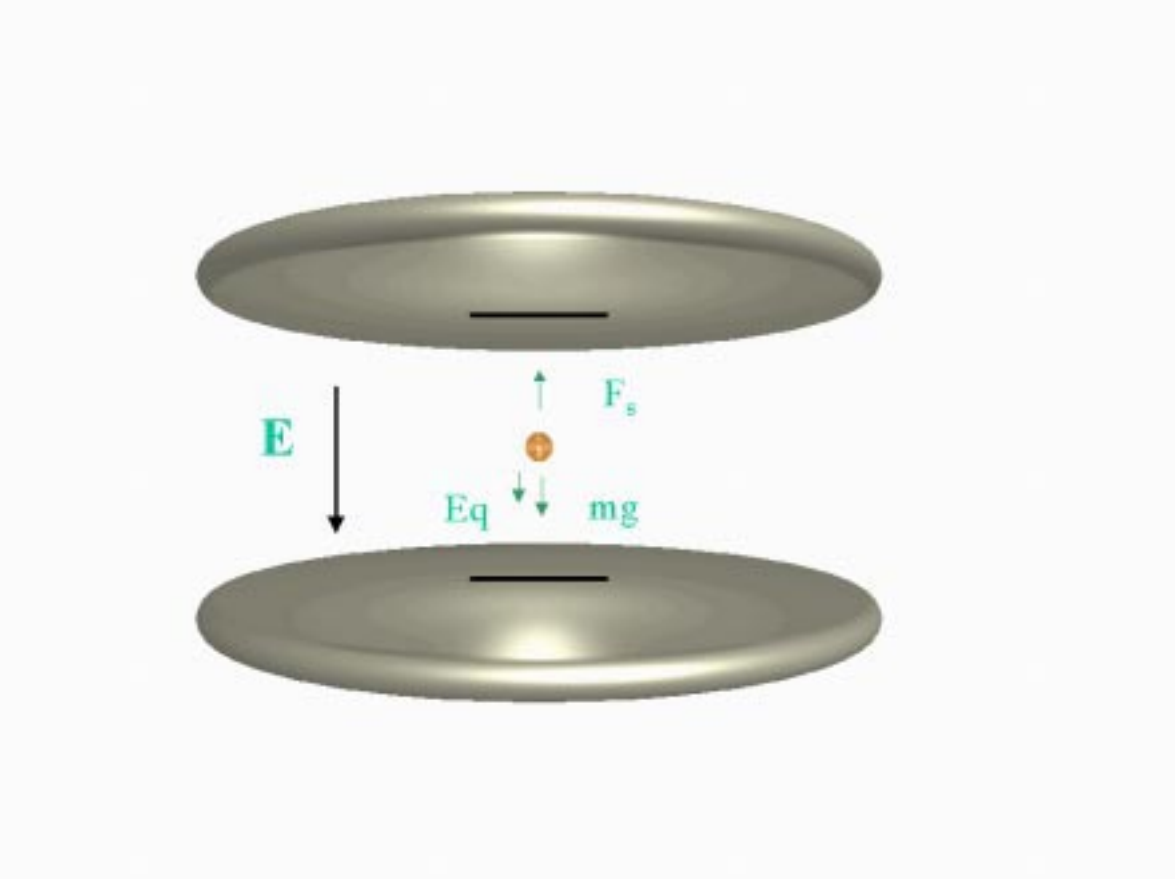

Figure 4.1: The drawing of a falling drop in the air between capacitor plates. The arrows illustrate the forces that are exerted on the drop.

We can redefine two new velocities in terms of the measured velocities

$$\begin{aligned} v_e &= \frac{(v_{down} - v_{up})}{2} \\ v_g &= \frac{(v_{down} + v_{up})}{2} \end{aligned}$$

In order to calculate the charge on the drop, we use the measured velocities $v_{E_{\rm up}}$ and $v_{E_{\rm down}}$ and then do the best fit to v_e and v_g. We find that the charge on the drop is

$$N_e \equiv \frac{q}{e} = C\, v_e \sqrt{v_g}\,, \tag{4.3}$$

where C is defined to be

$$C = \frac{18\ \pi d}{e}\ \sqrt{\frac{2}{(\rho_{oil} - \rho_{air})\ g}}\ \frac{1}{V_{down} + V_{up}}\ \eta^{3/2}\,, \tag{4.4}$$

in units of $s^{\frac{3}{2}} m^{-\frac{3}{2}}$ where d is the distance between the electric field plates, $\rho_{oil} = 913\,\mathrm{kg/m^3}$ is the density of silicone oil and $V_{down,up}$ is the voltage applied to the capacitor plates.

Once we measure the terminal velocities of the falling oil drops we can obtain the radius of each drop by

$$r = 3\ \sqrt{\frac{\eta}{2\ g\ (\rho_{oil} - \rho_{air})}}\ \sqrt{v_g}\,, \tag{4.5}$$

In our improved Millikan experiment we used four different effective states of the electric field instead of the two states $E_{\mathrm{up,down}}$ described above and used by the original Millikan experiment details are disscused in chapter 7.

Chapter 5

Apparatus

5.1 Improvements of the Original Millikan Technique

Technological developments have improved the original Millikan experiment of 1911 as shown in figure [5.1]. First, developments in semiconductor technology allowed us to use a CCD camera instead of a telescope in order to look at the falling drops. Second, a special drop ejector was designed using micromachining technology to produce multiple columns of multiple drops on demand. Finally, instead of a student sitting behind the telescope with a stopwatch in order the measure velocity of the drops, we used a desktop computer interfaced with a high speed framegraber to capture the images of the drops, collect and analyze the data and monitor the experiment.

5.2 The Experimental Layout

Our experiment is based on an improved Millikan technique. A simple layout is given in Figure [5.2]. We mounted all the hardware on a vibrationally damped optical table. Drops were produced and ejected inside the main Millikan chamber. The falling drops were backlit by a two dimensional array of red Light Emmiting Diodes (LEDs). In addition, since the drops were produced with diameter between $7 - 11\,\mu$m a 135 mm

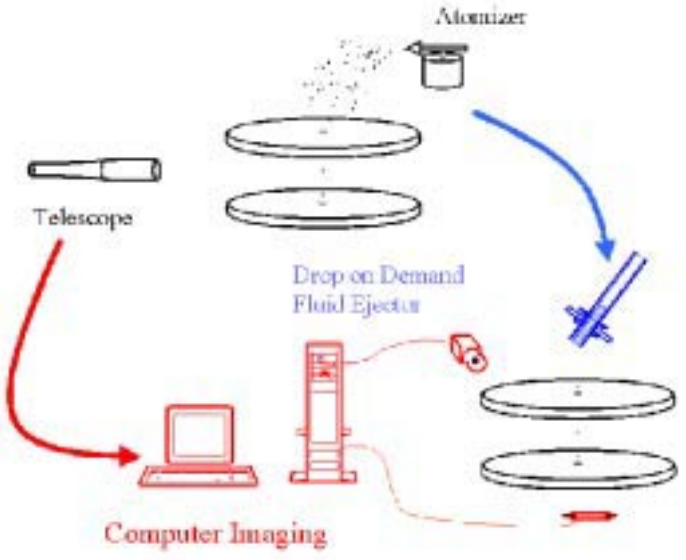

Figure 5.1: Improvements of the original Millikan experiment include replacing a telescope with CCD camera, an atomizer with a special micromachined drop ejector and a desktop computer interfaced with a high speed framegraber to capture the images of the drops, collect and analyze the data and monitor the experiment.

focal length lens was used in order to magnify the image of the drops onto the Charged Couple Device (CCD) camera.

5.3 Electronics

We used a CCD COHO camera Model 4110 in order to capture the positions of the falling drops. The output signal of the camera was transmitted at 60 Hz but since the signals were internally dual-interlaced we decided to use only one of the two internally overlapping fields. Therefore the camera output signal we used was 30 Hz. This output signal was split into two: one was transmitted to a high speed framegraber inside the computer and the other was transmitted to a frequency divider. The diagram of the electronic setup is shown in figure [5.3]. The drops were backlit by a stroboscopic LED source at 10 Hz; therefore the frequency divider divided the CCD signal by 3 to achieve eventually the 10 Hz flash rate of the LED strobe. The 10 Hz signal from the frequency divider was sent to a Wavetek 859 pulse generator and the

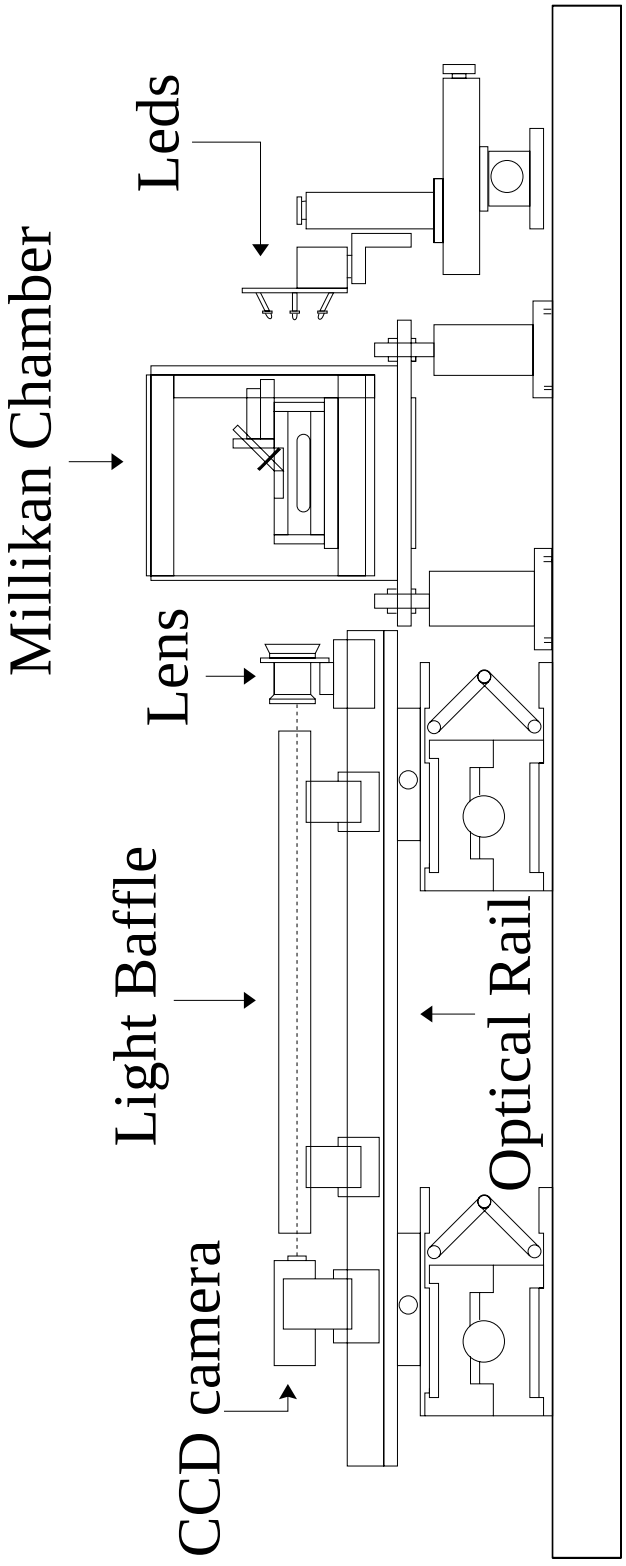

Figure 5.2: The layout of the Millikan experiment.

pulse generator was used to set the pulse width and pulse height of the LED strobe. The output of the pulse generator was split into two parts. One was transmitted to the LED strobe to set the times when images of drops were taken. The other part was transmitted to the computer in order to tell the framegraber when to capture an image.

The drop generation was an independent part of the electronics and unlike the LED strobe the signal was asynchronous with the camera output signal. The drop generation electronics included a Wavetek 859 pulse generator, an IRCO high voltage amplifier [65], a sequencing amplitude attenuator and the drop generator. The pulse generator was used in order to set the parameters that tuned the drops for stable ejection. The different parameters included the pulse width, the ejection frequency and the ejection mode i.e. single or double pulse with a delay time between each pulse. The output signal of the pulse generator was transmitted to the high voltage pulse amplifier to set the maximum pulse height that initiated the drop generator to produce a drop. The output of the high voltage amplifier was sent to the sequencing amplitude attenuator simultaneously with the sync output of the pulse generator. The reason for this is that the voltage sequencer contained several voltage dividers and therefore had to be fed by a high voltage and cycle between them. The output signal from the voltage sequencer was transmitted to a piezoelectric transducer which was part of the drop generator to initiate drop ejection as will be discussed in the following . The vertical and horizontal interdrop spacings were controlled by the drive pulses received by the drop generator.

The third part of the electronic setup was the alternating electric field the drops fell in. It included a positive and a negative high voltage power supply that were connected to the high voltage switcher. The voltage or the electric field switched at a frequency of 2.5 Hz. The frequency of the alternating electric field was set using the 10 Hz output signal from the frequency divider which was divided again by 4. The output signal from the high voltage switcher was transmitted to the bottom round capacitor plate in the Millikan chamber.

The part that was not mentioned in the electronics setup, Figure [5.3], is the delay between the alternating electric field and the image taking. The LED strobe and the

alternating electric field were synchronous but had a relative phase that was adjusted. The reason for the relative phase was to maximize the effect of the electric field per velocity measurement in order minimize the charge measurement error. A discussion of this will be given in chapter 7.

5.4 The Drop Generator

The special design for a fluid drop generator, called the dropper for brevity, was based on a combination of ideas for fluid drop ejectors to generate drops on demand using micromachining technology. The original idea was developed by inkjet companies (Cannon, Epson etc.) and then was adapted and improved for our needs.

The drop generator we used as seen in Figure [5.4] consisted of a glass fluid reservoir tube with a micromachined silicon orifice plate thermally welded to the end of the tube with no adhesive [55],[56]. The orifice plate we used had a 7 or 10 μm diameter, and the fluid used came in contact only with the glass tube and the silicon orifice plate that were chemically inert.

A piezoelectric transducer disk made from lead zirconate titanate was attached to the lower portion of the tube with epoxy or other high strength adhesive. The dropper was filled with 5 cS silicone oil. Silicone oil was chosen because of its low vapor pressure, low dielectric constant and the right viscosity and surface tension to generate small stable drops. Drop ejection was initiated by an electrical pulse that caused the piezoelectric transducer disk to contract radially on the glass, forcing a drop to form due to a pressure pulse traveling in the glass tube.

A manometer pressure controller made from flexible tubing and filled partially with liquid was connected to the glass tube controlling the pressure within the glass fluid reservoir. The manometer pressure was used to generate negative pressure on the fluid in the glass tube, to prevent the escape of dropper fluid onto the aperture in the absence of a drive pulse. The diameter of the drops could be varied by a factor of two by adjusting the pulse height duration and the negative pressure used, using the method described in [56]. Once the parameters were set, the drop diameter remained constant to better than 1%.

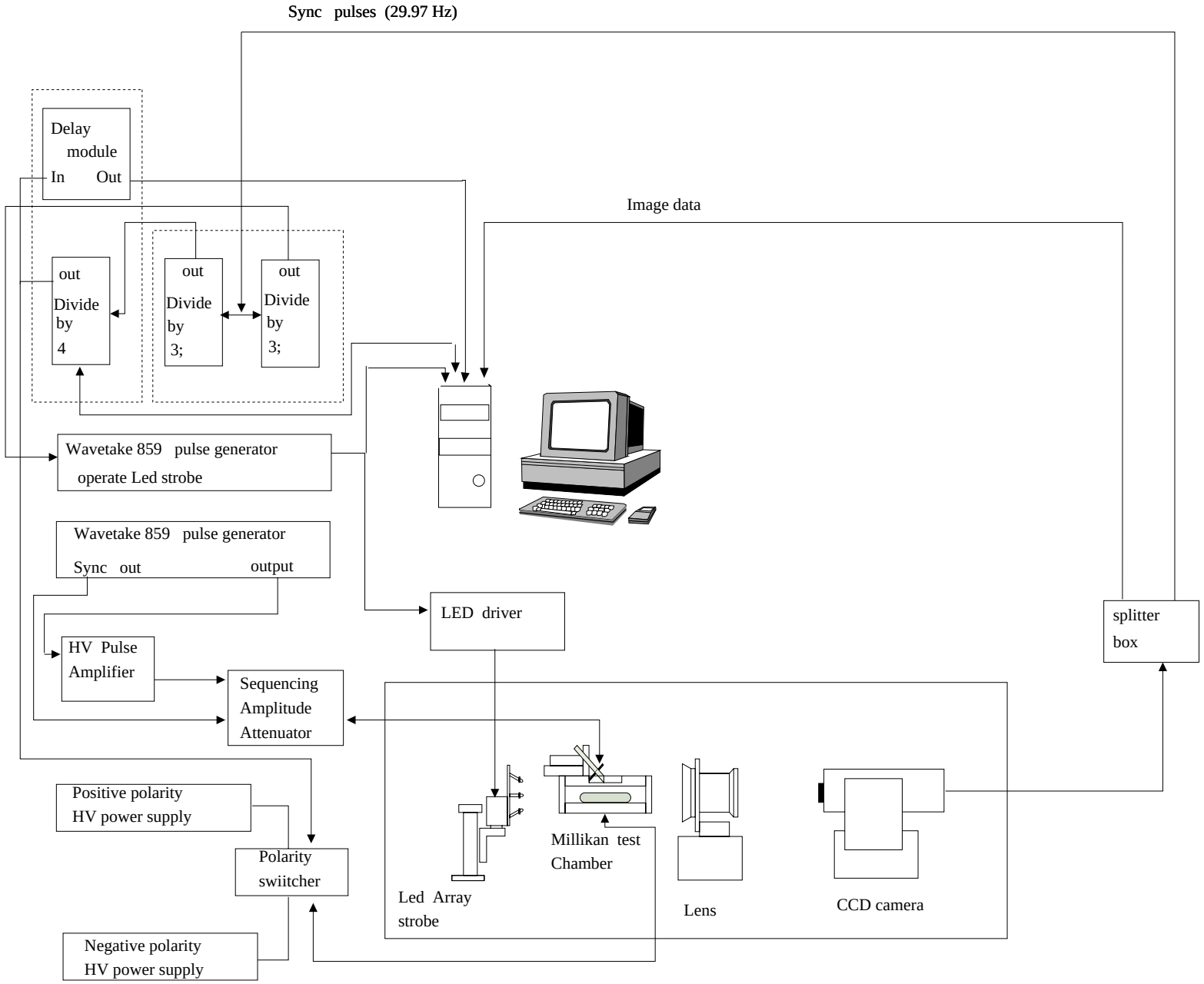

Figure 5.3: The electronic setup of the experiment.

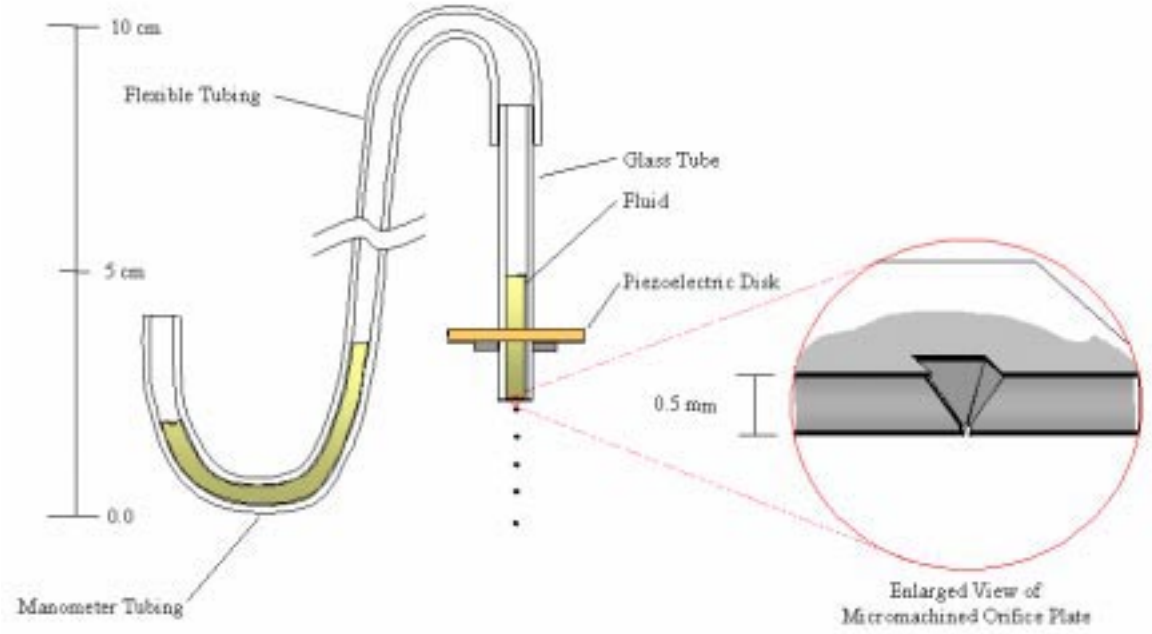

Figure 5.4: The schematic drawing of the dropper and of a micromachined silicon orifice plate that is thermally welded to the bottom of the dropper. An enlarged view of the micromachined orifice plate appears at the lower right. It shows the geometrical design of a 10 μm diameter hole that determines approximately the size of the drop.

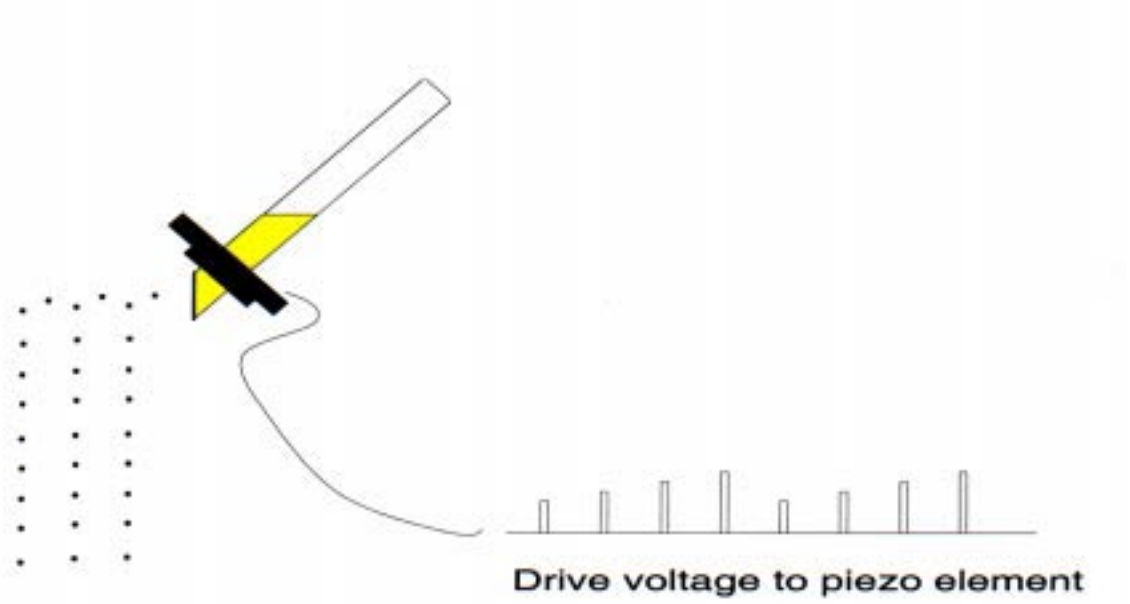

Figure 5.5: A plot of side ejection of drops using a voltage sequencer pulse. This technique was patented by E. Lee and M. L. Perl as described in [56].

In our experiment we wanted to achieve a high mass throughput. Therefore we wanted to automate the drop generation process and to produce multiple columns of multiple drops. The technique we used was based on a patent described in [56]. The horizontal and vertical inter-droplet spacing was controlled by the drive pulses received by the piezoelectric transducer on the glass fluid reservoir. The vertical spacing between two consecutive drops was determined by the time difference between the drive pulses corresponding to the two droplets. The horizontal spacing between two streams was controlled by the amplitude difference of the driving pulses corresponding to the two streams. The drive pulse amplitude determined the initial horizontal droplet velocity and position and hence the horizontal displacement of the droplet at any given time. In our experiment the drive pulses were varied such that the dropper generated two columns of drops separated horizontally by 300 μm and each column produced drops at 2 Hz.

5.5 The Electric Field Plates

Once the drops were produced, they fell through the electric field produced by a stainless steel parallel plate capacitor formed by an upper square ground plate of dimension 10 cm × 10 cm and a lower circular high voltage plate 7.62 cm in diameter. The plates were placed horizontally 0.81 cm apart with rectangular slits of dimension 1.27 cm × 0.08 cm to allow the passage of multiple columns of drops. A dropper holder, was placed on top of upper square ground plate with an x-y positioner to make sure the drops fell in the middle of the rectangular slits. The bottom circular plate was attached to a nylon platform by three screws that enabled us to adjust the parallelism of the plates. Since the drops we generated were $7.0 - 10.0\,\mu$m in diameter, they were sensitive to air currents. Therefore, the electric field plates and the dropper were contained within two layers of transparent polycarbonate shielding the drops from convection or other air currents. The inner box containing the capacitor plates was transparent acrylic 6.35 mm thick. This material was chosen so that we could illuminate and view the falling drops. The inner box and the dropper were located within another chamber with 9.5 mm thick transparent acrylic walls because we had observed in the previous experiment [6] that a single air current shielding box was insufficient (see Figure [5.6]).

5.6 Imaging Instruments

Once the drops were falling in between the capacitor plates they were backlit by the red LED strobe. The red LED light was diffused by a ground glass screen to create a uniform background illumination to the drop image. In addition, since the drops were contained inside two layers of polycarbonate shielding, we placed two optical windows; one in the front side of each box in order to prevent any distortion of the drop images created by the thick transparent polycarbonate shielding. The $7 - 10\,\mu$m diameter size drops we generated were magnified and the images were focused onto the CCD camera using a 135 mm focal length lens 18 cm away from the drop generator. Every 0.1 s the LED strobe flashed for 56 μs and the drops were

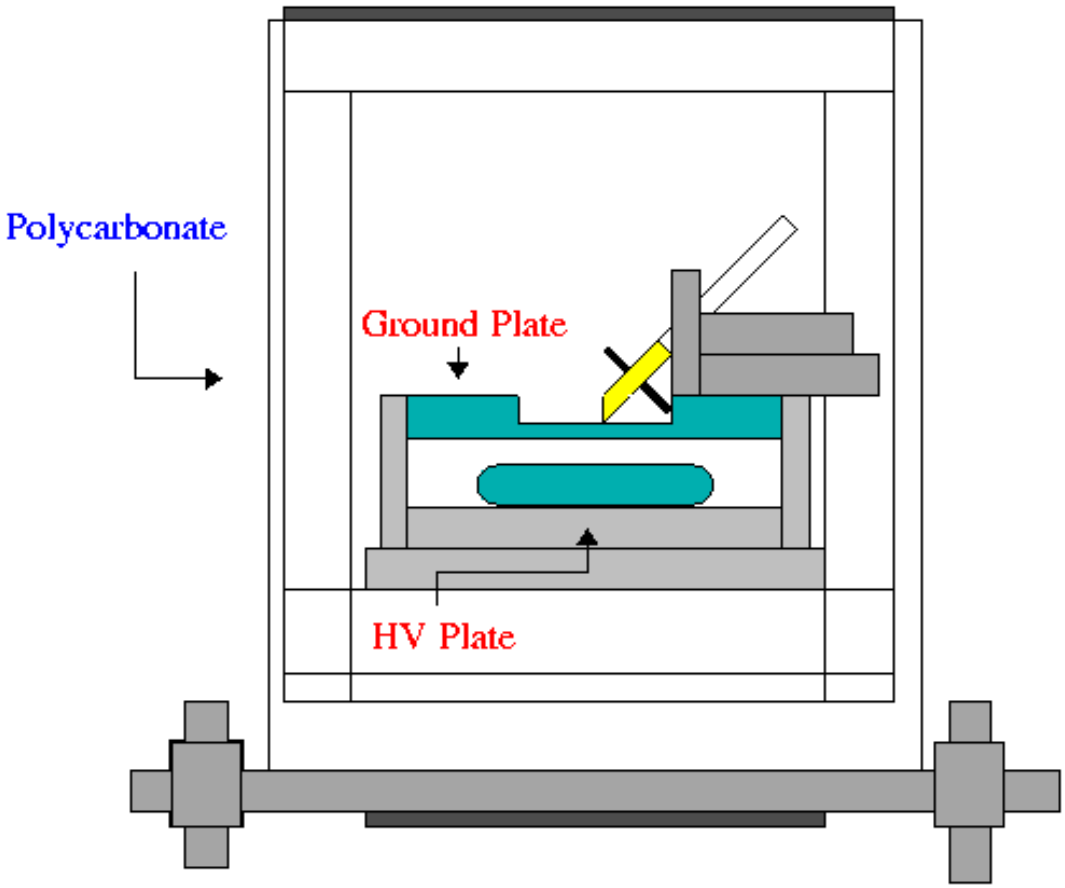

Figure 5.6: Diagram of the Millikan chamber.

imaged with a CCD COHO camera model 4110 [66]. The active region of the CCD was 6.4 mm ×4.8 mm (736 pixels×242 pixels) where the 6.4 mm edge was chosen along the trajectory of the falling drops to maximize the number of position measurements and to avoid image distortion caused by camera interlacing. The optical system had a magnification of 2.7 so that the actual field of view of the falling drops was 2.37 mm vertically and 1.77 mm horizontally. The drops had an average terminal velocity of 1.3–3.2 mm/s depending on the drop radius so that each drop was in the field of view for 8–11 sequential images. A high speed video framegraber captured images from the CCD camera for computer analysis. We used a Bitflow data rapter pci version VS4 framegraber device, 8 bit (256 gray scale) resolution. The image information was then written to the hard disk. Discussion on the data acquisition and the position measurement algorithm is given in chapter 6.

5.7 Electronic Sensors

The last components of the experiment are a set of electronic sensors that were added to the apparatus in order to monitor the experiment and a tool that checked whether interesting events that showed up were artifacts or not. We added a few electronic sensors. The first addition was a vibration sensor that was attached to the Millikan chamber. The second was a motion sensor that checked if somebody was in the lab during the run. The third was a temperature sensor to study and understand the influence of temperature on the system. The fourth was the humidity sensor to keep the air dry. The last one was a pressure sensor that monitored the negative pressure that was applied on the fluid in the dropper and studied its influence on drops ejection. We found that the different negative pressures applied changed the diameter of the drops and the lateral position of the columns of drops generated.

Chapter 6

Data Acquisition

6.1 Data Recording

The falling drops were recorded by a CCD COHO camera model 4110. The digital output of the camera was transmitted to a framegrabber. A framegrabber is an image capture card device that maintains in its memory a buffer of the captured images. We used a Bitflow data rapter pci version vs4 framegrabber device with 8 bit (256 gray scale) resolution. The image information was then written to the hard disk. Since the camera had an internal pseudo-interlacing procedure involving intensity averaging over alternate vertical pixels, we chose only one set of frames that was written to the disk at 10 Hz. Once the data was copied to the hard disk a recording program was responsible for looking at each frame that contained different drop images. A frame is a picture of all the drops in the field of view taken by the CCD camera every 0.1 s. An example of a frame containing drops image is shown in Figure [6.1].

6.2 Position Measurements

To find the positions of the drops in each frame an image processing program was written. The image recognition aspect of this task was made simpler because of the controlled environment. The operating point for the background illumination was chosen to maximize the signal to noise ratio produced by the camera response

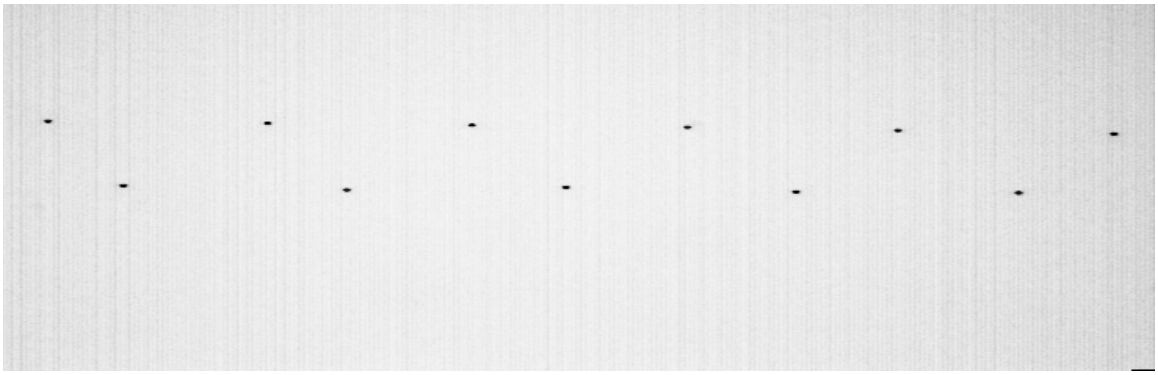

Figure 6.1: An example of a captured image of 2 columns of multiple drops $\sim 10\ \mu$m in diameter falling along the 2.37 mm vertical field of view.

function. Illumination was strictly controlled in such a way that over the entire field of view, the background intensity varied by less than ± 1.2 greyscale units. The position measurements were made in two steps. In the first step, The drop images were guaranteed to have at least one pixel with intensity less than a threshold value that was chosen to be 200 greyscale units. The thresholding procedure isolated the pixels which composed the drop images and a recursive algorithm using an adjacency criteria grouped together pixels from the same drop image. From this information, a rough center of mass calculation of the image position was possible. To achieve the required accuracy, it was necessary to minimize the effects of camera noise and variations in background illumination. Details of the calibration will be described in chapter [7]. In the second step a higher accuracy algorithm was used. It operated on an adjustable 10 pixel $\times$ 10 pixel region centered around the rough center of mass. It calculated the background illumination level for each drop image independently by averaging the pixels intensity value from the four corner pixels in the considered region. Once the background illumination level is measured its value is used combined with the 20 darkest pixels to calculate the center of mass position of the drops using equation (6.2).

Let the region of interest of the image as shown in Figure [6.2] be represented by N pixels with coordinates x_i, z_i and greyscale value I_i. Suppose that the background illumination has greyscale value B. The center of mass in the z direction can be

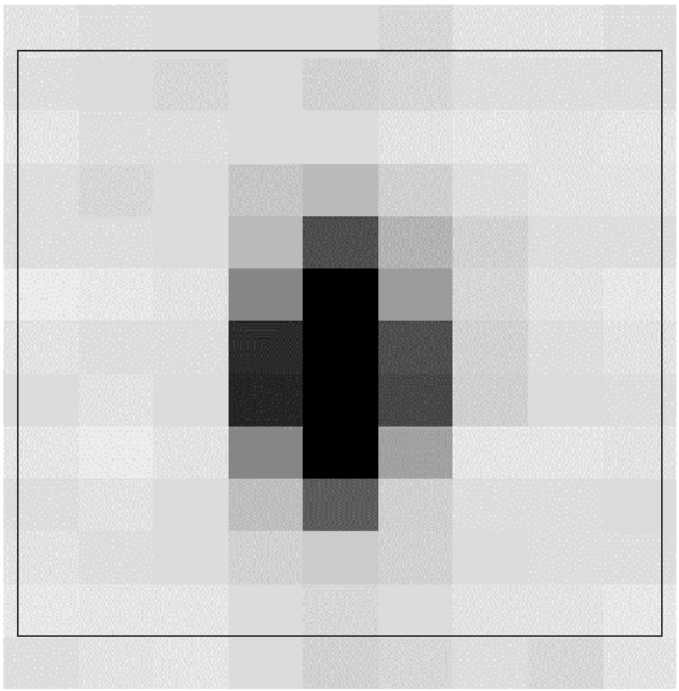

Figure 6.2: A typical drop image containing about 6×7 pixels. The 20 darkest pixels above the background illumination level were included in the position measurement algorithm.

calculated as follows.

$$\begin{aligned} z_{CM} &= \frac{\sum_{i=1}^{N}(I_i - B)z_i}{\sum_{i=1}^{N}(I_i - B)} \\ &= \frac{\sum I_i z_i - B\sum z_i}{\sum I_i z_i - B\sum 1} \end{aligned} \tag{6.1}$$

Once the position of the different drops in each frame had been measured the recording program wrote the data to hard disk. The data was saved every hour with different file names. The structure of the data in the file was organized to save the data frame by frame with the beginning of each frame containing a frame header with the following information: the electric field strength, the vibration sensor output, the motion detector output, the time the frame was captured and the output of the pressure and humidity sensors.

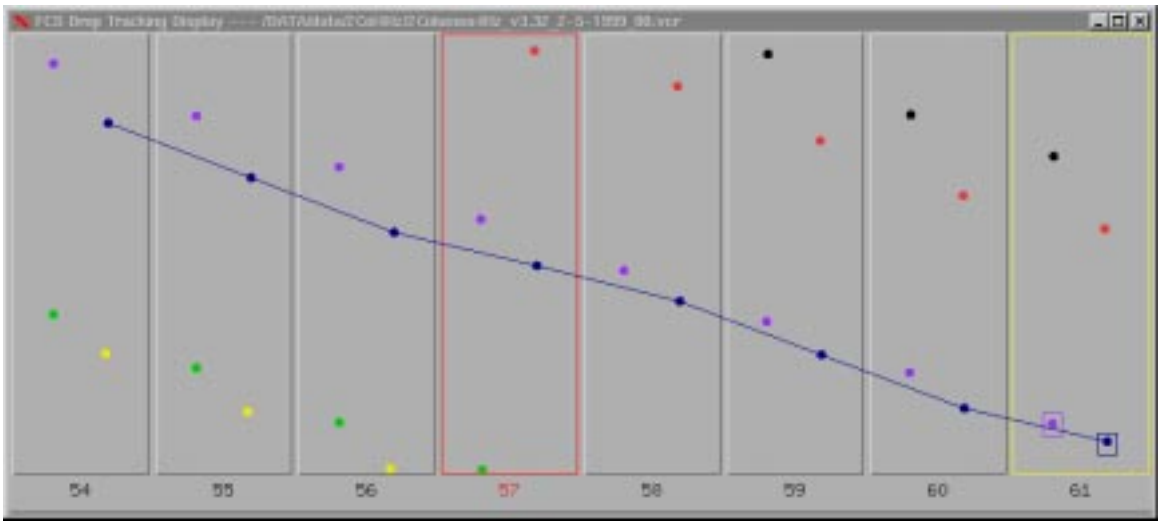

Figure 6.3: An example of the tracking algorithm extracting the trajectory of a drop with 8 positions as it fell.

6.3 Image Recognition and Tracking

The initial stage of data processing converted the raw data which was a series of sequential 8 bit greyscale images into a list of measured centroid positions that were stored in data files. Since more than one drop image was present in each frame, in the second stage, a tracking algorithm was used to extract the sequence of centroids corresponding to the trajectory of each drop from the stream of data. The centroids from the same drop in different frames should be associated together into a single trajectory. The algorithm used maintained an internal state consisting of a list of drops for which some amount of data existed and the future trajectory was calculable. The information was extracted from a buffer of 20 frames of past centroid data. The algorithm applied the following procedure to every incoming frame:

1. The expected positions of all drops for which some amount of data were calculated.

2. The current image was checked for centroids in the expected positions.

3. If the position of a centroid in the current image was found correctly it was eliminated from the list. The centroid data was then used to update the data

on the appropriate drop. Every drop which was not correctly identified in the current image was eliminated from the list and passed to the analysis code.

4. The remaining centroids from the current image were added to the buffer.

5. Using the data in the buffer, all possible combinations of centroids were hypothesized to be the trajectory of a drop. This trajectory was then checked for consistency. If the trajectory was satisfactory, the centroids were removed from the buffer and the data was used to add a new drop to the list drops for which some data existed.

The details of the algorithm were consistent with the low artifact rate achieved and the available computational speed. Step 3 in the algorithm was very conservative; an apparent collision between a drop and any centroid caused the drop to be eliminated from the list. Step 5 incorporated hashing techniques and an optimized search order through the list of possible trajectories in order to minimize the combinatorics involved. In order to prevent any given drop from entering the data sample twice, the trajectories found in Step 5 were constrained to have an initial point near the top of the field of view. A handful of adjustable parameters were necessary to control the tolerances in steps 3 and 5 and to minimize the statistical possibility that an incorrect combination in step 5 would be found to be satisfactory.

The above algorithm achieved efficiencies in excess of 99.9% and was tested using Monte Carlo techniques to have a sufficiently low artifact rate. Details of the test are described below. High drop rates with over 40 centroids per image were possible where the limiting factors were statistical issues in Step 5. The algorithm was also easily capable of on-line operation at such rates. Hence, the experiment was not limited by tracking or computational issues.

The tracking algorithm described above extracted all the physically consistent trajectories of drops from the data files and passed the list of drop information to the analysis code. The information passed consisted, for each drop, a list of vertical and horizontal position measurements, guessed values for the electric field value, the frame and drop number it belonged to and the number of pixels in the drop image

that were above threshold. Using this information the analysis code described in the next chapter 7 was used to look for the FCPs.

6.4 The Monte Carlo Program

A Monte Carlo program was used to check the efficiency of the tracking algorithm and to make sure an FCP has the same effciency as any other charge drop. The data simulated represent data set two in Table [7.1]. The drop size generated was $9.5\,\mu$m. The terminal velocity of the drops due to the gravitational force was 2.4 mm/sec and the terminal velocity of drops with one electron charge due to the electric field was 0.18 mm/sec. The charge measurement accuracy was $q \pm 0.019$.

Figure [6.4] shows the tracking efficiency versus the charge. The charge efficiency for drops with fractional charge was 99.94% of that for neutral drops. The tracking efficiency for larger drops was smaller. We found that the difference in the efficiency between the charges was about 0.1%. The reason was that the tracking algorithm did not contain the correct values of the electric field which were measured in the analysis stage. Therefore, the values used for the electric field naturally lead to worse estimates of the position of a drop in the future image to larger charge drops.

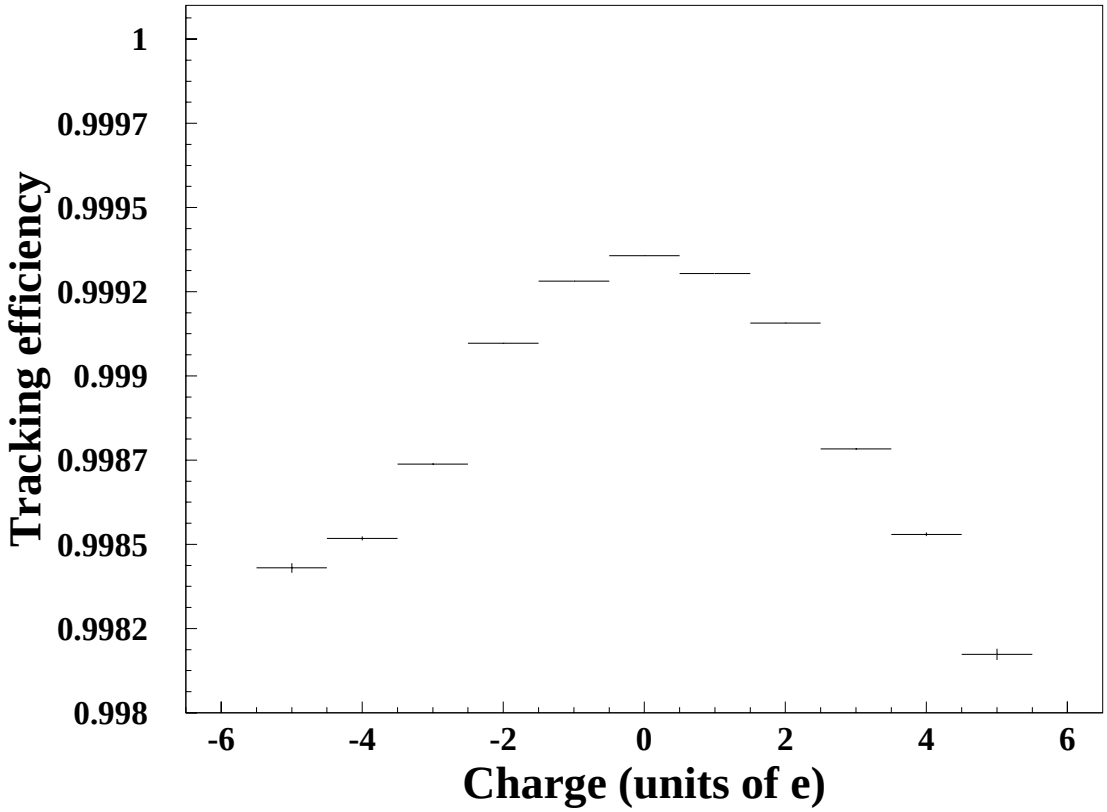

Figure 6.4: The tracking efficiency vs. the charge on the drop. The measurement is based on a Monte Carlo program to insure we did not loose any FCP.

Chapter 7

Analysis

7.1 Calibration

A few measurements were made in order to calibrate the image analysis before we started the experiment. First, we had to adjust the centroid calculation algorithm. Second, we had to find the threshold level to isolate the relevant pixels and adjust the illumination to have the lowest camera noise.

7.1.1 The Pixel Cut

The number of dark pixels taken into the centroid calculation had to be calibrated since it affected the position measurement accuracy. The first test we did was to measure the residuals, which were defined to be the measured velocity minus the fitted velocity, versus the number of pixels that went into the centroid calculation. We can see the results of the test in Figure [7.1] which is a representative of run II and III. The figure shows the results with background illumination of 200 (gray scale value). Based on this plot the optimum value for the number of pixel is 15, this number depends on the size of the drop and optical system. The intensity of each pixel is digitized to 8 bit resolution giving 256 gray scale value.

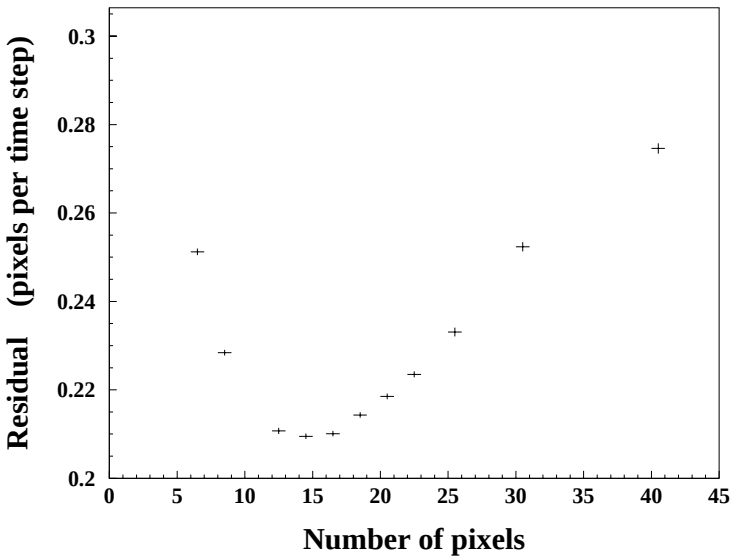

Figure 7.1: The velocity residuals vs. the number of dark pixels used in the position measurement algorithm. Background illumination was 200 (gray scale value).

7.1.2 Illumination Gray Scale Value

The next test checked the variation in the pixel noise with respect to changes in the intensity level. The test was done by pointing an LED through ground glass to the CCD camera and gradually increasing the current that passed through the LED and recording the average intensity of an image. The test was done without drops in the field of view. The response of pixel noise to variation in the intensity was measured by recording the intensity values of each image and by calculating two different quantities: the partial rms intensity and the total rms intensity. The partial rms intensity measured the intensity fluctuations in each pixel by calculating the difference between the corresponding pixel value between two images and using Equation (7.1)

$$I_{partial\ rms} = \frac{1}{\sqrt{2}} \sqrt{\frac{\sum_{i=1}^{N} (I_1(x_i, y_i) - I_2(x_i, y_i))^2}{N}}\,, \tag{7.1}$$

The difference was used to eliminate systematic changes in illumination across the surface of the CCD camera.

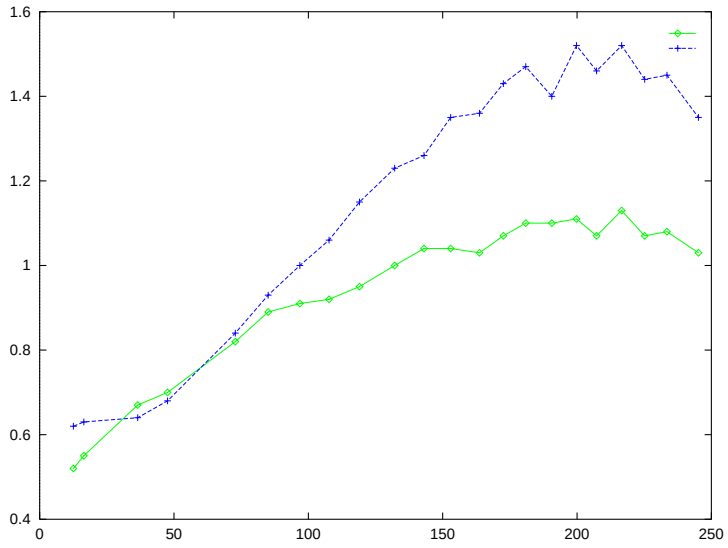

Figure 7.2: The partial rms intensity $I_{partial\ rms}$ green trace (diamond) and the total rms intensity $I_{total\ rms}$ blue trace (cross) versus the average intensity gray scale value.

The second quantity was the total rms intensity of an image that was calculated using

$$I_{total\ rms} = \sqrt{\frac{\sum_{i=1}^{N}(I_i^2)}{N} - < I >^2}\,, \tag{7.2}$$

The results are presented in the Figure [7.2].

The total rms intensity saturated at about 150 (gray scale value) and then the stripping effect which will be discussed in section 7.8.2 started to be appreciable. We measured the noise level to find at what background level to operate. We had to find the illumination level that corresponded to the best signal-to-noise ratio. The next test was done by taking images using the usual experimental set-up with drops in the field of view in order to check the contrast versus the background intensity. The contrast was defined as the maximum difference between the drop and background intensity level. The measurement results are shown in Figure [7.3]. Figure [7.3] shows that the contrast response to the intensity was linear and on the other hand Figure [7.2] shows that the pixel noise reached a threshold at background level of 150 gray scale value. Therefore, the signal over noise increased as the background level increased. We did not want to operate at maximum background level to prevent the

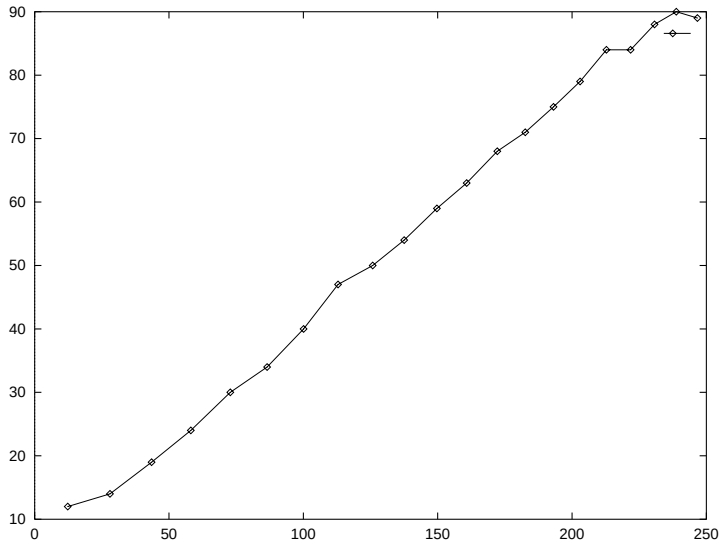

Figure 7.3: Contrast versus the intensity. where the contrast is defined as the maximum difference between the drop and background intensity level.

saturation of the CCD camera and hence lose information on the exact background level. Our conclusions from the calibration measurements were to operate at a background level of 200 gray scale value which was optimal taking into account the signal over noise. In addition, based on the first test the 15 darkest pixels went into the position measurement algorithm.

7.2 The Charge on the Drop

In chapter 4 we explained how the charge on the drop was determined once we observed the changes in the position or motion of the drops. We found the charge on the drop to be

$$N_e \equiv \frac{q}{e} = C v_e \sqrt{v_g}\,, \tag{7.3}$$

where C is defined to be

$$C = \frac{18\ \pi d}{e} \quad \sqrt{\frac{2}{(\rho_{oil} - \rho_{air})\ g}} \quad \frac{1}{V_{down} + V_{up}} \quad \eta^{3/2}\,, \tag{7.4}$$

in units of $s^{\frac{3}{2}}m^{-\frac{3}{2}}$ where d is the distance between the electric field plates, $\rho_{oil} = 913\,\mathrm{kg/m^3}$ is the density of silicone oil and $V_{down,up}$ is the voltage applied to the capacitor plates.

However the expressions for v_e and v_g given in chapter 4 are too simple since they assume that the electric field was produced by a perfect square wave voltage which was not the case as will explained in the next section. The charge on the drop was calculated by using the measured velocities $v_{E_{\mathrm{up}}}$ and $v_{E_{\mathrm{down}}}$ and then using a least square fit to find v_e and v_g. The measured velocities were given by $\Delta z_i \equiv z_i - z_{i-1}$, the difference between two consecutive z position measurements taken 0.1 second apart. Each drop velocity is given by Equation (7.5)

$$\Delta z_i = v_g + qE^r v_e \tag{7.5}$$

where $v_e,\ v_g$ are the terminal velocities of the drops due to the electric or gravitational force respectively, q is the charge on the drop and E^r Eq. (7.8) expresses the relative strength ($|E^r| \leq 1$) of the electric field during the Δt interval before the z_i measurement. If the electric field was generated by a perfect square wave E^r would have been ± 1 as we assumed in chapter 4.

Using the expression (7.5) we find $v_e,\ v_g$ in terms of the measured velocities and the different values of the effective electric field to be

$$v_e \Delta t = \frac{N \sum_i^N E_i^r \Delta z_i - \sum_i^N E_i^r \sum_i^N \Delta z_i}{N \sum_i^N (E_i^r)^2 - (\sum_i^N E_i^r)^2} \tag{7.6}$$

$$v_g \Delta t = \frac{N \sum_i^N \Delta z_i - \sum_i^N E_i^r \sum_i^N \Delta z_i E_i^r}{N \sum_i^N (E_i^r)^2 - (\sum_i^N E_i^r)^2} \tag{7.7}$$

where N is the number of measured Δz_i. In our experiment each drop had about $7 - 10$ velocity measurements.

7.3 The Electric Field

The electric field alternated in synchronization with the position measurements, but at a frequency down by a factor of 4. We took position measurements at 10 Hz and the electric field alternated at 2.5 Hz. Therefore, every 100 ms the drops would feel a different effective electric field resulting in four different values of the effective electric field during its period of oscillation. The effective electric field between two position measurements is called polarity for brevity and given by

$$E^r = \int_t^{t+\Delta t} E(t)\, dt \tag{7.8}$$

Due to the design of the high voltage switch, the rising and falling switching time constants were different and have been measured to be 7.91 ms and 1.56 ms respectively. For $\Delta t = 100$ ms electric field was normalized such that $\int_t^{t+\Delta t} E_{constant}\, dt = 1$. The four effective electric fields can be calculated to be

$$E_{effective,HH} = \int_{\delta}^{100.+\delta} \frac{1.}{100.}(A - (A-B)e^{\frac{-t}{\tau_{LH}}})\, dt \tag{7.9}$$

$$E_{effective,HL} = \int_{-100.+\delta}^{0} \frac{A}{100.}dt + \int_{0.}^{\delta} \frac{1.}{100.}((A-B)e^{\frac{-t}{\tau_{HL}}} + B)dt \tag{7.10}$$

$$E_{effective,LL} = \int_{\delta}^{100.+\delta} \frac{1.}{100.}((A-B)e^{\frac{-t}{\tau_{HL}}} + B)dt \tag{7.11}$$

$$E_{effective,LH} = \int_{-100.+\delta}^{0} \frac{B}{100.}dt + \int_{0.}^{\delta} \frac{1.}{100.}((A-B)e^{\frac{-t}{\tau_{LH}}} + B)dt \tag{7.12}$$

where $\tau_{LH} = 7.61$ and $\tau_{HL} = 1.56$. A and B are the normalized electric fields pointing up and down and δ is the delay time between a position measurement and the time the electric field alternates.

The reason for choosing a delay time was the fact that the charge measurement

error was inversely proportional to the sum of the square of the polarities as given by

$$\sigma_{v_g}^2 = \frac{\sum_i^N (E_i^r)^2}{N\sum_i^N (E_i^r)^2 - (\sum_i^N E_i^r)^2}\sigma_v^2\,, \tag{7.13}$$

$$\sigma_{v_e}^2 = \frac{N}{N\sum_i^N (E_i^r)^2 - (\sum_i^N E_i^r)^2}\sigma_v^2\,, \tag{7.14}$$

Optimizing the contribution of the polarities to the charge measurement accuracy, it was found that delay time should be $\delta = 2\,\text{ms}$.

7.3.1 Measurement of the Effective Electric Field

The technique to measure the electric field was to plot the velocity of the drops for two different charges for each of the four different polarities.

$$\Delta z_{q_1} = v_g + q_1 E^r v_e \tag{7.15}$$

$$\Delta z_{q_2} = v_g - q_2 E^r v_e \tag{7.16}$$

where E^r is the electric field polarity. The difference between the mean measured velocities values was equal to the terminal velocity of the drop due to the electric field. Hence the electric field was given by

$$E = \frac{\Delta z_{q_1} - \Delta z_{q_2}}{(q_1 - q_2)}\frac{6\pi\eta r}{e} \tag{7.17}$$

7.4 The Electric Dipole Moment

The two rectangular slits in the center of the electric field plates which allowed the passage of the drops caused a spatial nonuniformity in the electric field. This nonuniformity combined with the induced dipole on the drop produced small changes in the apparent terminal velocity. This dipole force monotonically reduced the velocity of the drops as the drops fell. Figure [7.4] shows the measured electric field over the

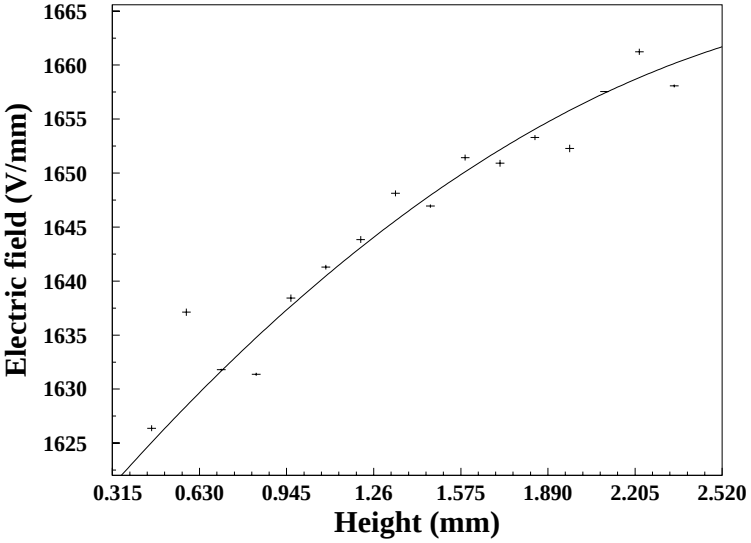

Figure 7.4: The measured electric field (in units of V/mm) vs. the height (in units of mm).

field of view. Fitting the electric field to a second order polynomial gave

$$E(z) = 0.16116 \times 10^7 + 99.765Z - 0.46402 \times 10^{-1}Z^2 \tag{7.18}$$

We obtained the gradient of the electric field from the equation above and the induced dipole on the drop from

$$P = 0.16116 \times 10^7 (5.14 \times 10^{-6})^3 (\epsilon - 1)/(\epsilon + 2) 4\pi\epsilon_0 = 8.465 \times 10^{-21} \tag{7.19}$$

where 5.14×10^{-6} m is the diameter of the drop. The induced dipole force is given by $\vec{F_P} = (\vec{P} \cdot \vec{\nabla})\vec{E}$. From this calculation we were able to find the induce dipole effect to be 3.15% of v_g.

7.5 The First Aerodynamic Effect

In addition, there was an aerodynamic effect on the trajectory of the drops. The air in the vicinity of the columns of falling drops was dragged downwards changing the

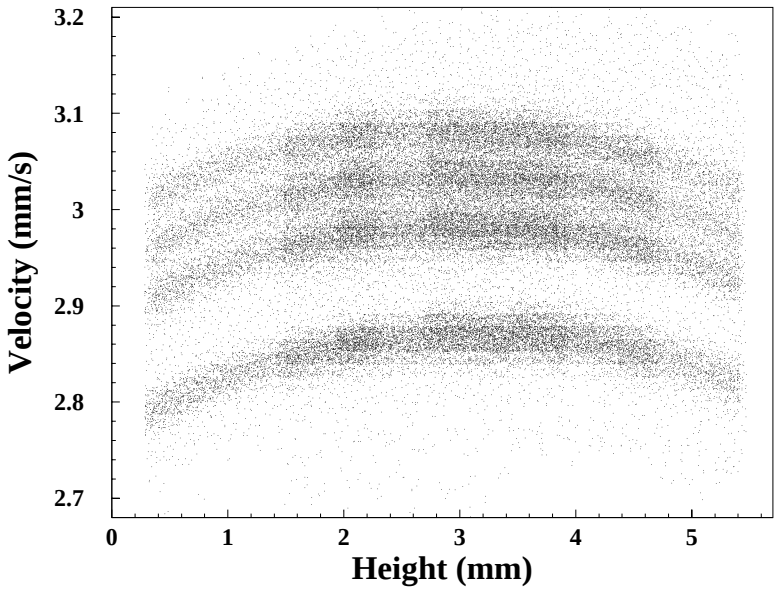

Figure 7.5: The velocity of the drops (in units of mm/s) vs. the height (in units of mm). The four dark shaded bands in the figure correspond to four columns of drops with the electric field turned off.

apparent terminal velocity. The resulting steady flow of the air caused the drops to reach a maximum velocity half-way between the plates, and then decelerate as can be seen in Figure [7.5]. The magnitude of the effect was 1.46% of v_g. Since our operating point was 0.2 mm higher than half way between the plates the electric dipole moment effect and the first aerodynamic effect acted simultaneously with opposite signs as can see in Figure [7.6]. These two phenomena caused the drops to decelerate over the field of view leading to an overall effect of 1.69% of v_g.

7.6 The Second Aerodynamic Effect-The Shift

Moreover, there was an additional interesting aerodynamic effect. Since we had an imbalance in the number of positively and negatively charged drops, as can be observed in Figure [7.7] there was a net motion of the drops and hence of the air, which oscillated with the alternating electric field. This caused a shift in the measured charge of the order of 0.01 which was corrected. The correction was made by adding

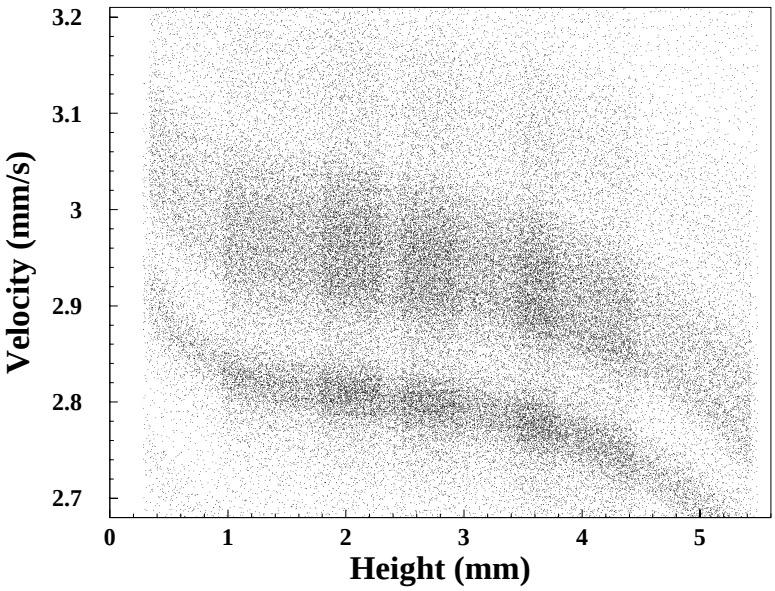

Figure 7.6: The velocity of the drops (in units of mm/s) vs. the height (in units of mm). The four dark shaded bands (three of them converged into the top wide band) in the figure correspond to four columns of drops with the electric field turned on.

a small velocity value to all the drop velocities depending on the direction, value of the electric field and the size of the drops. The small velocity value was estimated by measuring the charge shift of all the peaks and calculating the apparent velocity they would have acquired under the influence of the alternating electric field. Figure [7.8] shows the values of the small velocity correction that lead the charge peaks to be aligned on integer numbers. The reason we have an increase of 38% in the value of the shift correction on the 38 day of data set II is not believed to be a real effect. As explained above, the voltage did not alternate as a perfect square wave and therefore the values of the effective electric field were $E^r \leq 1$. In addition, the charge received small corrections that were inversely proportional to the difference between the adjacent effective electric field values. Hence changing the delay time between a position measurement and the time the electric field alternates on the 38^{th} day of data set II from $\delta = 10\,\text{ms}$ to $\delta = 2\,\text{ms}$ changed the effective electric field values and affected the shift correction. We should note that although the correction used depended on the the direction and value of the electric field and the size of the drops there is another

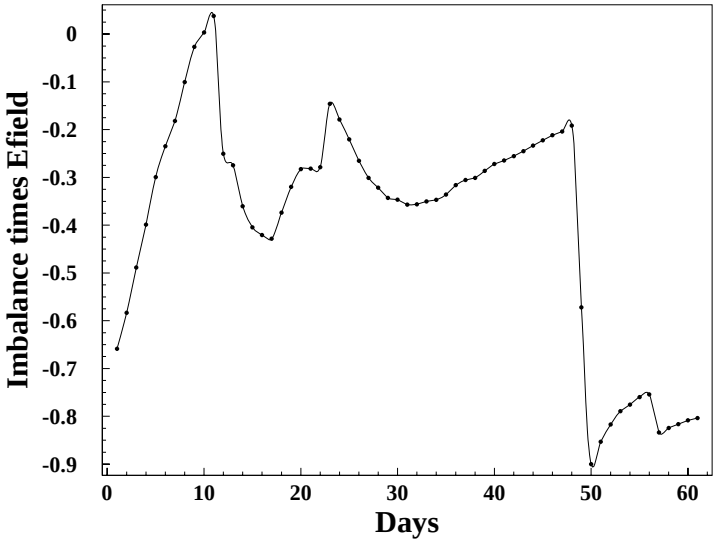

Figure 7.7: The charge imbalance times the effective value of the electric field as a function of days of data collection for data set II.

parameter that should have been considered in our correction which would render it to be on a drop-to-drop basis. This additional parameter is the distance between the drops. It has not been used in this work since we did not have the three dimensional information on the position of each drop image but only the (x,z) cordinates. It was found that the shift correction depends on the relative velocity between the drops reinforcing that the shift correction should be done on a drop-to-drop, especially if the distance between the drops decrease or drop size decrease.

Data set	D (μm)	Mass (mg)	Vg (mm/sec)	Ve (mm/sec)	Drops num	σ_q (e)
I	7.6	1.35	1.54	0.19	6.42×10^6	0.0160
II	10.4	10.13	2.88	0.16	1.88×10^7	0.020
III	9.4	5.92	2.34	0.18	1.49×10^7	0.019

Table 7.1: Summary information of our run which consisted of three data sets with different drop diameter sizes, terminal velocities, number of drops per data set and charge measurement accuracy. Where Ve is defined as the terminal velocity of a drop due to the electric force for charge one.

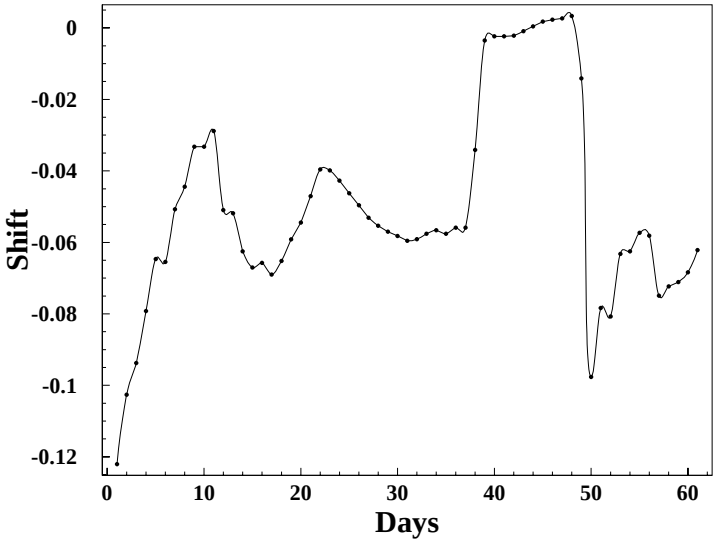

Figure 7.8: The shift which is a small velocity value added to all the drop velocities vs. days of data collection for data set II.

7.7 Measurement Criteria

After applying the above corrections we required that all drops used in the data sample met the measurement criteria listed in Table [7.2]. The first cut which removed drops with charges higher than 4.5 was required since the measurement accuracy decreased with charge. This is the major cut which removed 3.056% of the total number of drops. The second cut removed drops with less than 6 centroids in order to have at least two charge measurements per drop. This cut excluded 0.215% of the drops. The third cut checked the consistency of the charge within a drop to exclude drops that had an ion attached to them while they fell since that would simulate a fractional charge artifact. We chose $\delta q < 0.2$ where δq was defined to be $q_{max} - q_{min}$ for the following two reasons. First, we found that if we simulate events with no fractional charge the δq distribution fell at $\delta q = 0.2$. Second, fractional charge events were uniformly distributed between 0 and 1 with a small peak at 1. However, the peak at 1 is washed out due to the fact that the tracking algorithm examined the physical consistency of a track by excluding tracks with large residuals. This cut removed about 0.342% of the drops. The last cut checked for drops with high residuals to

eliminate tracking artifacts or any abrupt changes that happened in the system. For example, someone tapping on the main Millikan chamber during the run can easily move the position of the drops. This cut removed 0.0399% of the drops.

cuts	Percentage removed
$\|q\| < 4.5$	3.056%
$N > 6$	0.215%
$\delta q < 0.2$	0.342%
R$< 8\sigma_v$	0.0399%

Table 7.2: The drops used in the data sample were subjected to cuts on the charge q ($|q| < 4.5$ e), on the number of centroids N ($N > 6$), consistency of charge measurements of one drop δq ($\delta q < 0.2$ e), and the residuals R ($R < 8\sigma_v$), where σ_v is the uncertainty in the velocity due to Brownian motion. Percentages removed by each cut were in order of application.

7.8 Charge Measurement Errors

7.8.1 Brownian Motion

The largest contribution to the charge measurement error arose from the Brownian Motion

$$\sigma_v = \sqrt{\frac{K_B\ T}{3\pi\ \eta\ r\Delta t}}\,, \tag{7.20}$$

where $K_B = 1.3807 \times 10^{-23} JK^{-1}$ is the Boltzmann constant, T is the temperature in Kelvin, η is the viscosity of the air, r is the radius of the drops and t is the time between measurements.

This error propagates as an uncertainty in the calculation of the charge of a drop according to

$$\sigma_q = \sigma_v\ C\ \sqrt{2\ v_g} \tag{7.21}$$

We see from Table [7.3] that the contribution from Brownian Motion is different for the three data sets because the drops in the three date sets had different radii. For example, we expect according to Equation (7.20) the measurement error in data

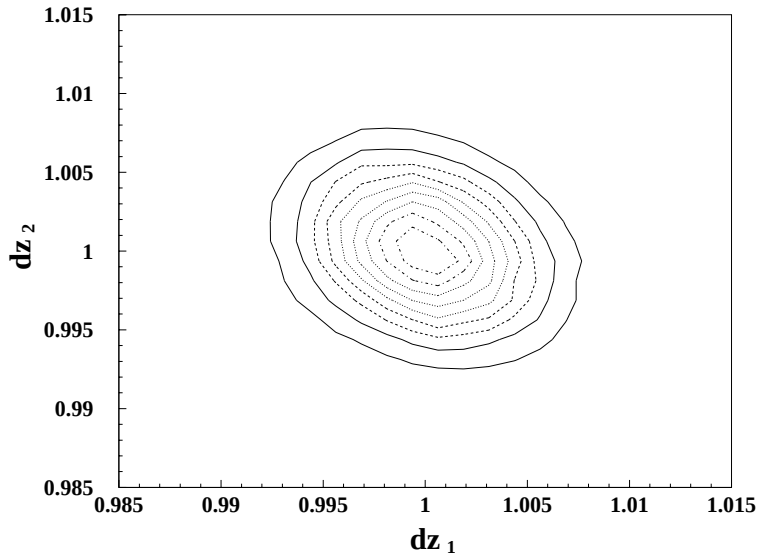

Figure 7.9: dz_1 vs. dz_2.

set II to decrease by 27% compared to data set I since drops in the latter had 10.4 μm diameter compared to drops with 7.6 μm diameter that were tested in the former.

7.8.2 The Centroid Measurement Error

The second measurement error arose due to centroid measurement error. The centroid error was observed through the anticorrelation between two consecutive velocity measurements as shown in Figure [7.9]. There were two main sources that could have contributed to the centroid measurement error. The first was a random uncorrelated variation in pixel values. The second was a systematic stripping effect that was observed across any given image. This is illustrated in Figure [7.10].

Other sources may contribute to the position measurement error but their contribution is less than one percent. An example is the determination of the background illumination level. The drop position was measured by taking the center of mass of the drop image as in Equation (6.2). We did not check if this was the optimal technique i.e. we could have used a fit for the shape of the intensity distribution instead of a calculation based on the 20 darkest pixels.

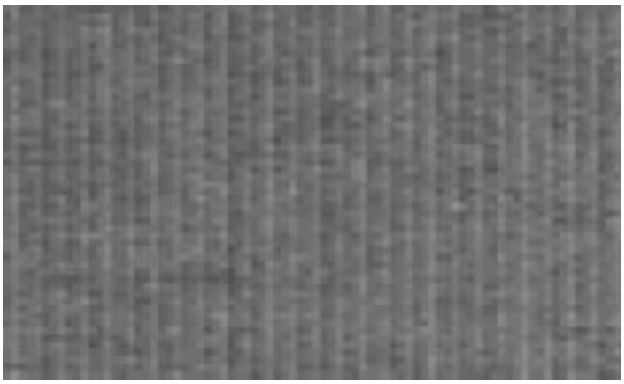

Figure 7.10: Empty region of camera image with enhanced contrast.

7.8.3 The Nonuniform Electric Field

In addition to the dominant electric dipole effect explained above we had obviously the electric field monopole term change over the field of view due to the nonuniformity produced by the two rectangular slits in the center of the two capacitor plates. In order to measure the change in the electric field, the field of view was divided into adjacent slices in the direction of the falling drops. Then, using the technique explained in the beginning of chapter 7 we measured the electric field values in every slice. The result can be seen in Figure [7.4] where the electric field value was observed to increase by 2% over the field of view. The electric field nonuniformity is a smaller effect than the the electric dipole effect as can be seen from

$$\frac{|e\Delta\vec{E}|}{|(\vec{P}\cdot\vec{\nabla})\vec{E}|} \sim 4\times 10^{-2} \tag{7.22}$$

where P is the induced dipole on the drop as estimated in Equation (7.19). Therefore the electric field nonuniformity appeared as a small contribution to the measurement error and the electric dipole effect was corrected in the analysis.

In Table [7.3] we see that data set I has a smaller contribution from the electric field nonuniformity error compared to the other two data sets. The reason for the difference is that the value of electric field for data set I was 13.4% smaller than the other data sets. After data set I, we increased the value of the electric field from $1.6\times 10^6\, V/m$ to $1.85\times 10^6\, V/m$ since the charge measurement error was inversely

proportional to the electric field value.

Source of Error	Set I	Set II	Set III
Brownian motion	57.0%	40.9%	42.1%
Centroid measurement errors	36.2%	47.8%	48.2%
Electric field non-uniformity	6.8%	11.4%	9.7%

Table 7.3: The contribution of different sources of error to the charge measurement accuracy σ_q^2 for each data set.

7.9 Results

In the following we present our results after applying all the corrections and the measurement criteria described in Table [7.2]. Figure [7.11] shows the data after applying the last three cuts described above, specifically for 4.14×10^7 drops. We see sharp peaks at integer charges and no drops with charges further than 0.14 from the nearest integer, other than a single drop at $q = 0.294$.

Figure [7.12] shows the residual charge distribution of q_c, which is defined as $q_c \equiv q - N_c$ where N_c is the integer closest to q, for data Set II. It displays a superposition of integer charge peaks centered at zero. The peaks at each integer charge have a Gaussian distribution shape. The standard deviation (σ_q) at charge zero is 0.018. The standard deviation (σ_q) of the residual charge distribution of q_c is 0.002 with $\chi^2/n.d.f. = 30$. We do not have a better $\chi^2/n.d.f.$ since the the plot is a superposition of different Gaussians. The higher charges result in a larger charge measurement error since σ_q gets a contribution from terms involving v_e/v_g. The search for drops with fractional charge is clarified in Figure [7.13] by the superposition of all data sets using the variable $q_s \equiv |q| - N_s$, where N_s is defined to be the largest integer less than $|q|$. This is the entire data remaining after applying the cuts. There is no background subtraction. Again one sees at $q_s = 0.294$, the sole drop charge measurement that lies outside of the integer tails.

We have applied the following experimental philosophy to this measurement. In searching for a rare phenomenon it is important to apply the same data selection

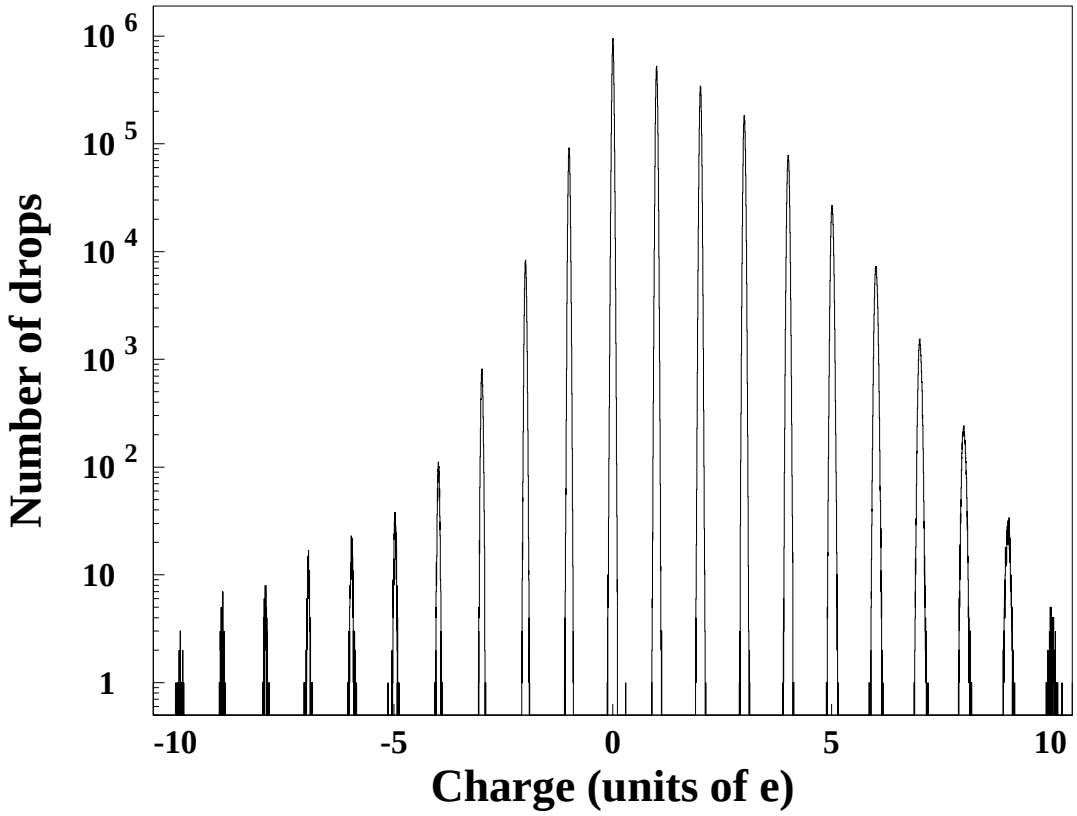

Figure 7.11: The charge distribution of 4.14×10^7 drops.

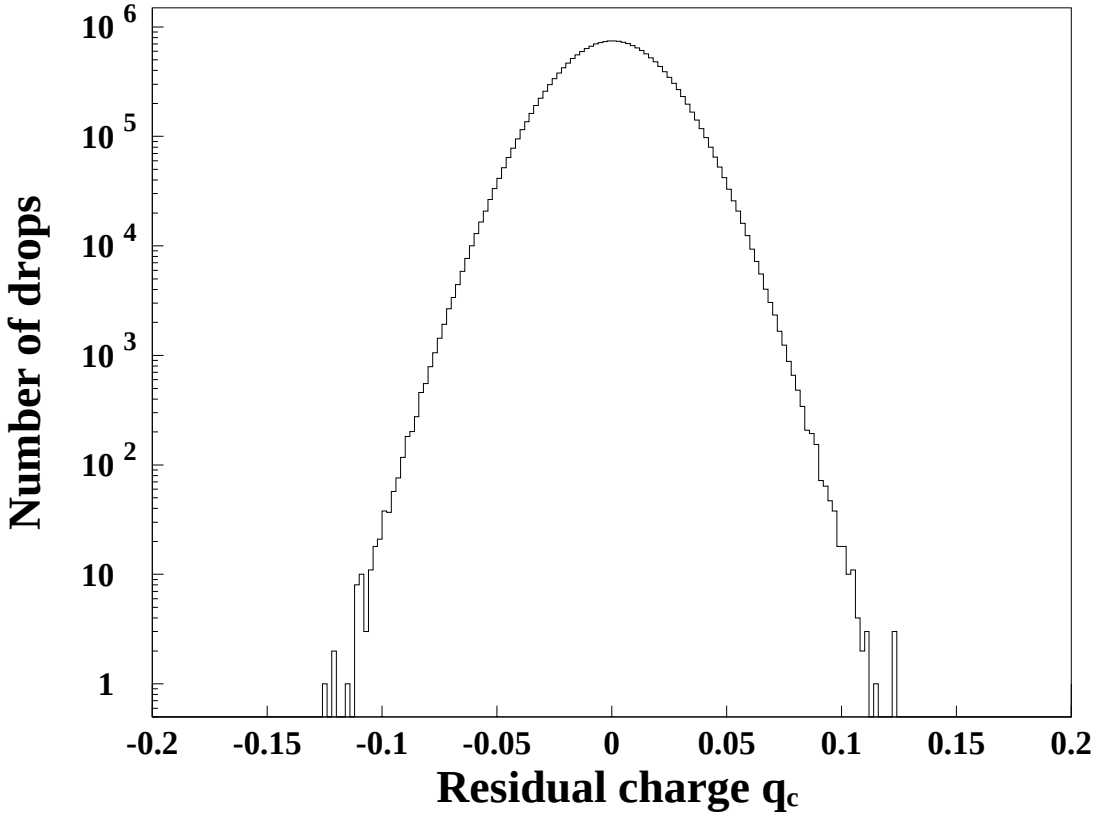

Figure 7.12: The residual charge based on 1.885×10^7 drops. The residual charge is defined as $q_c = q - N_c$.

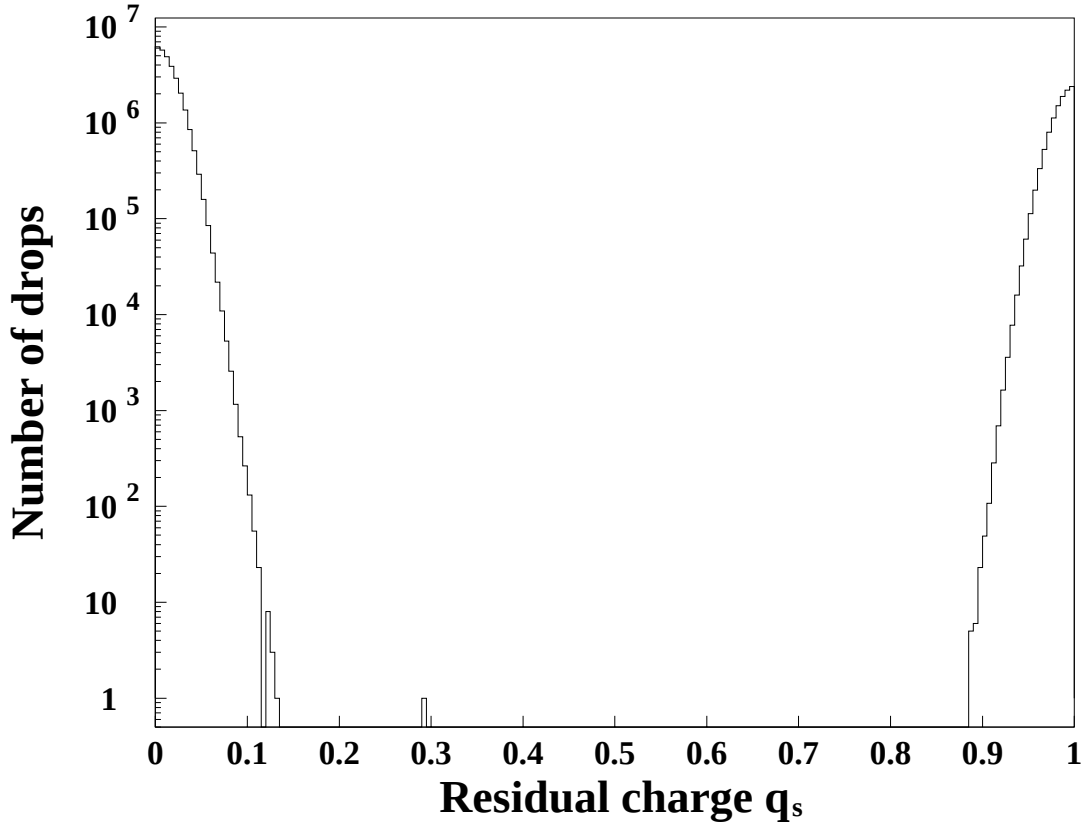

Figure 7.13: The residual charge on all the data. The residual charge q_s is defined $q_s = q - N_s$.

criteria to all the data as we have done. The drop with $q = 0.294$ fits all of our criteria and we do not know whether it is the first indication of some background that begins to appear at the 1 in 4×10^7 level or it has more significance. Our only choice is to repeat the experiment with a larger sample and we intend to do so. Table [7.4] presents 95% confidence upper limits on the number of FCPs per nucleon in silicone oil for each data set. We set conservative limits by counting the number of events in the signal region defined as within 2σ of each fractional charge and calculating the Poisson limits without background subtraction. Figure [7.14] shows the combined 95% confidence upper limits on the number of FCPs per nucleon in silicone oil for the entire run. We did not find any evidence for free FCPs. We found with 95%

Data set	D (μm)	Mass (mg)	Range	Upper limit
I	7.6	1.35	$0.15-0.26$	3.84×10^{-21}
			$0.34-0.84$	3.84×10^{-21}
			$0.26-0.34$	6.07×10^{-21}
II	10.4	10.13	$0.16-0.84$	5.12×10^{-22}
III	9.4	5.92	$0.17-0.86$	8.76×10^{-22}
Total		17.4	$0.17-0.26$	2.98×10^{-22}
			$0.34-0.84$	2.98×10^{-22}
			$0.26-0.34$	4.71×10^{-22}

Table 7.4: Final results from the three data sets including the combined limit on the total mass accumulated. The table describe drop diameter D, sample mass, the range of residual q_c and the 95% CL upper limit on the density of fractional charge particles per nucleon for each data set.

confidence that in silicone oil the concentration of particles with fractional charge more than 0.16 from the nearest integer charge is less than 4.71×10^{-22} particles per nucleon except in the region $0.26-0.34$ where the upper limit is 2.98×10^{-22} particles per nucleon.

7.9.1 The Single Anomalous Event

As we explained above, we do not know the source of the fractional charge event observed. We do not know whether it is the first indication of some background that begins to appear at the 1 in 4×10^7 level or it has more significance. The drop had a charge of $q=0.294\pm0.016$ which is $2.46\sigma_q$ from a charge of $\frac{1}{3}$. The probability of a Gaussian distribution of $\sigma_q=0.016$ to generate points at value of 0.294 or larger is less than a 1% but there is no reason to assume any particular value of charge to a new particle. The drop satisfied all measurement criteria as can be seen in figures [7.15-7.16]. It had 10 position measurements, a dq of 0.08 and its largest residual was 0.98.

The only way of knowing whether the event at $q=0.294$ has a higher significance is to repeat the experiment with a larger throughput and to apply the new insight

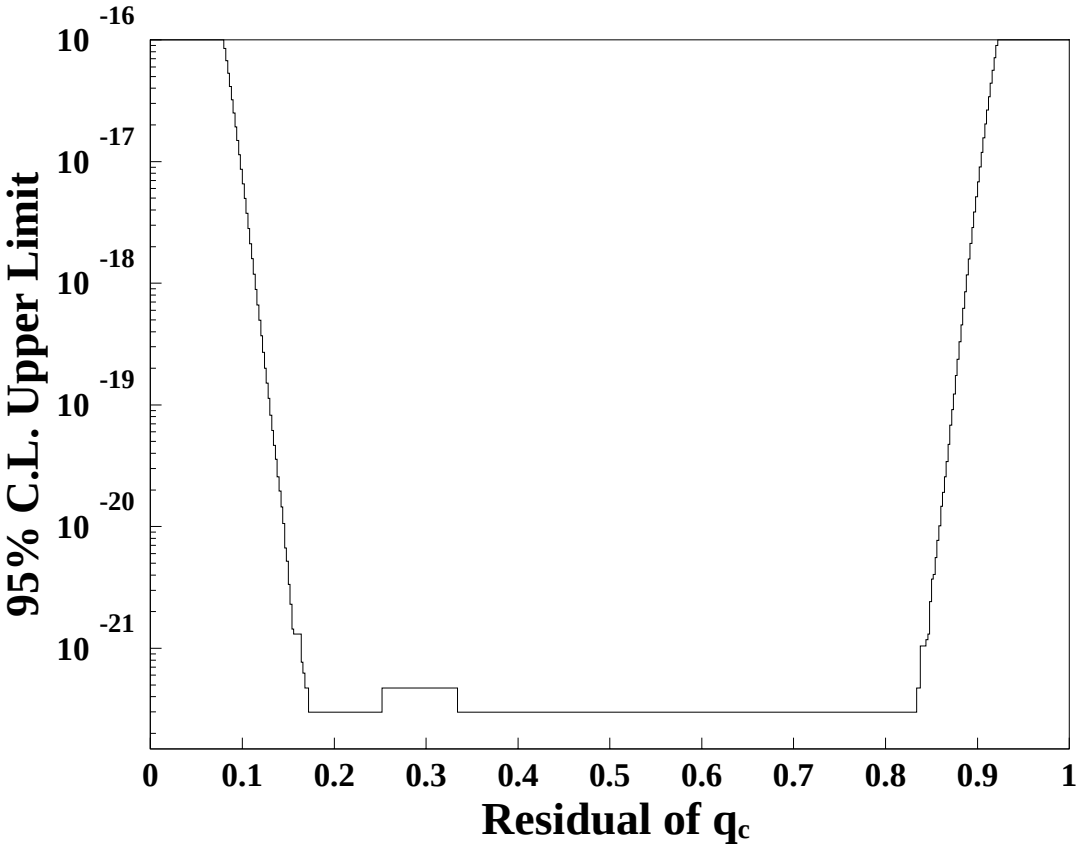

Figure 7.14: The 95% C.L. upper limit on density of fractional charge particles per nucleon vs. residual of q_c.

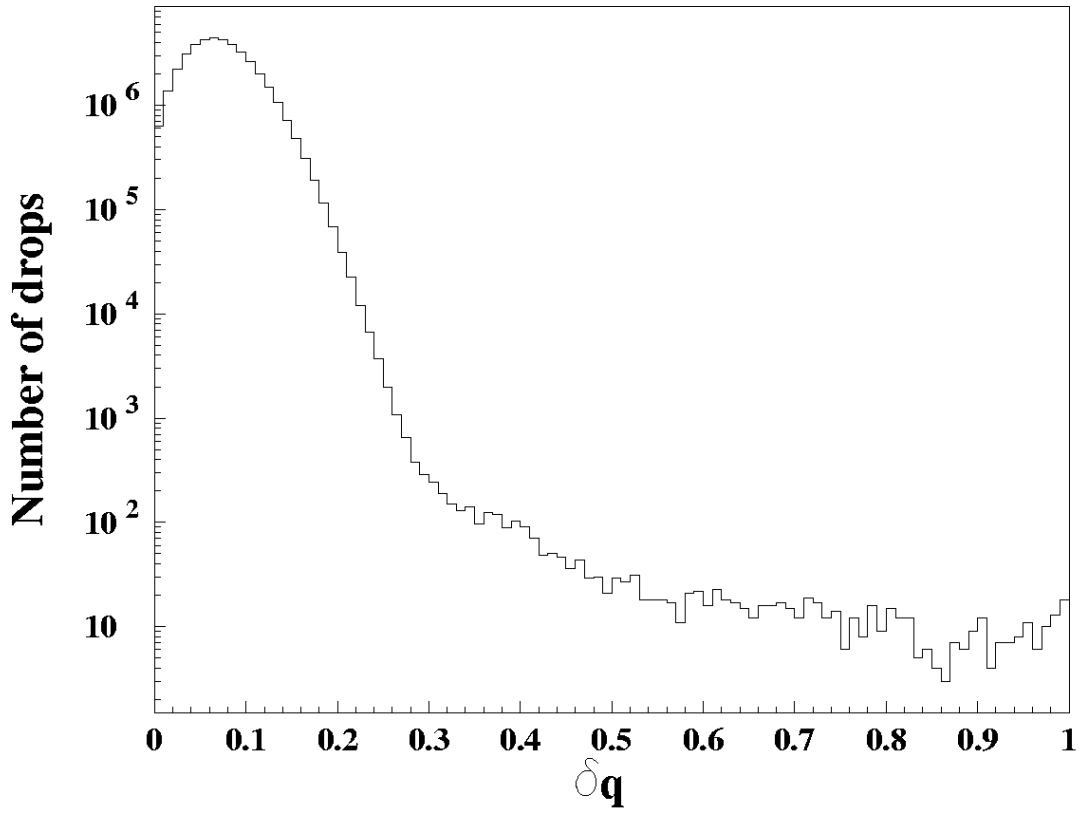

Figure 7.15: The third measurement criteria checks the consistency of charge measurements of one drop. This cut excludes drops with $dq > 0.2$. The dq value of the drop with a charge of 0.294 was 0.08.

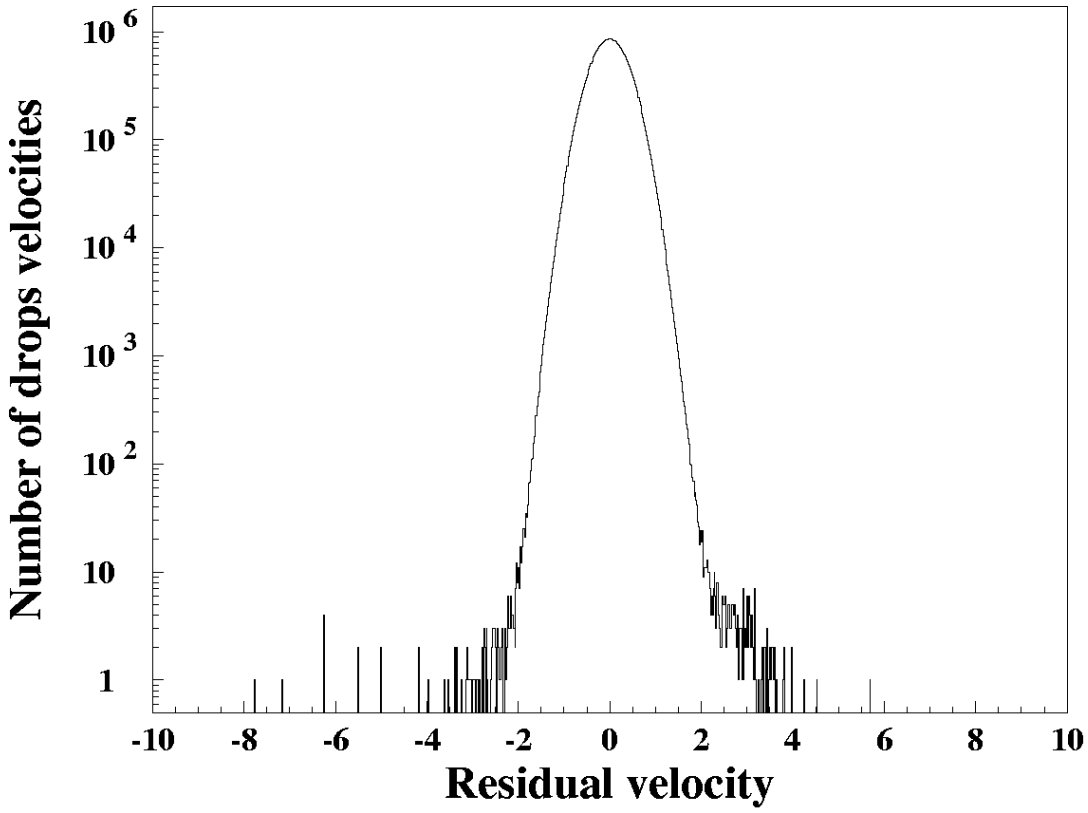

Figure 7.16: The fourth measurement criteria removes drops with high residuals R ($R < 8\sigma_v$), where σ_v is the uncertainty in the velocity due to Brownian motion. The drop with a charge of 0.294 appeared in data set I where the cut required residual > 2.9 and the residual value of that drop was 0.98.

we gained analyzing this data. After analyzing all the data and applying all the cuts we looked more carefully at this anomalous event, studying the images of the drop with charge 0.294 more carefully. The trajectory of the drop with charge 0.294 is shown in Figure [7.18] where a line connects all the drop positions as it fell in the field of view. We found that the drop that fell adjacent to the 0.294 charge drop has a charge of 11.25. The spacing between these two drops was 0.118 mm which was less than the average distance between drops in the data sample i.e. 0.46 mm. Using the information available in this experiment we were not able to cut on the distance between adjacent drops since first, as we decide on our set of cuts we dont change them as we learn new information about the data and second, we had only the 2D distance between the drops. An estimate using fluid dynamics as given below shows that the drop with a charge of 11.25 could have changed the spatial location of the 0.294 charge drop to simulate a fractional charge drop artifact. However, we found only one event that suggested a fluid dynamical interaction of the drops through the air; therefore we can not conclude that this anomalous event is a fractional charge artifact. Only a larger mass throughput experiment that will correct for this fluid dynamical effect per drop will be an answer to our question.

Consider two drops one neutral and one with charge 11.25. We estimate the displacement of the neutral drop due to the charge 11.25 drop using the measured velocities. As we see in Figure [7.17], the charge 11.25 which is labeled as drop A causes the neutral drop labeled B to be pushed by the air due to the fluid dynamical interaction in the direction of the falling drop. The neutral drop located at B gets a contribution to its velocity which is equal to

$$V_{down} = \frac{3}{4}\frac{Va}{r}(1 + cos(\theta)^2) \tag{7.23}$$

where V is the relative velocity between the drops, a is the radius of drop A, r is the distance between the drops as illustrated in Figure [7.17]. Measuring $V = 1.45\,\mathrm{mm/s}$, $a = 8.3\,\mu\mathrm{m}$, $r = 0.118\,\mathrm{mm}$ and $\theta = 32.44^0$. We find that drop A pushes drop B in the direction of their fall through the air by adding or subtracting from the velocity of drop B the amount $v_Z \sim 0.06\,\mathrm{mm/s}$. On the other hand, a drop with a charge of

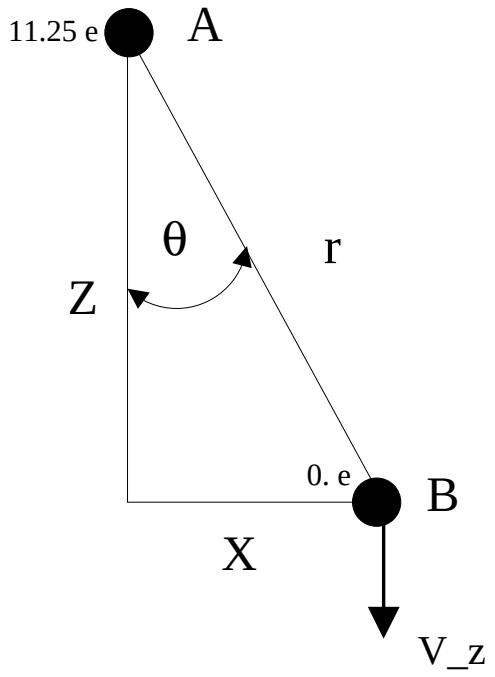

Figure 7.17: Illustration of the geometry relevant for Equation (7.23).

0.294 and a diameter of 7.9 μm reaches a terminal velocity $V_e = 0.056$ mm/sec which is very close to the velocity a neutral drop should obtain if it is dragged through the air due to drop A.

In future experiments using the Millikan technique the following improvements are recommended based on the experience gained in our experiment.

1. The real $3D$ distance between the drops should be obtained since the drops were fluid dynamically coupled through the air. It is important to estimate how this interaction affects the spatial location of the drops on a drop-to-drop basis. The $3D$ distance between the drops will tell us when the fluid dynamical effects through the air are strong enough to cause a fractional charge artifact.

2. Instead of recording the calculated positions of the drops to disk it is recommended to record the raw data i.e. the centroid information onto disk in order to search for an algorithm that will yield least position measurement errors.

3. The experiment should be monitored online by allowing automatic saving of

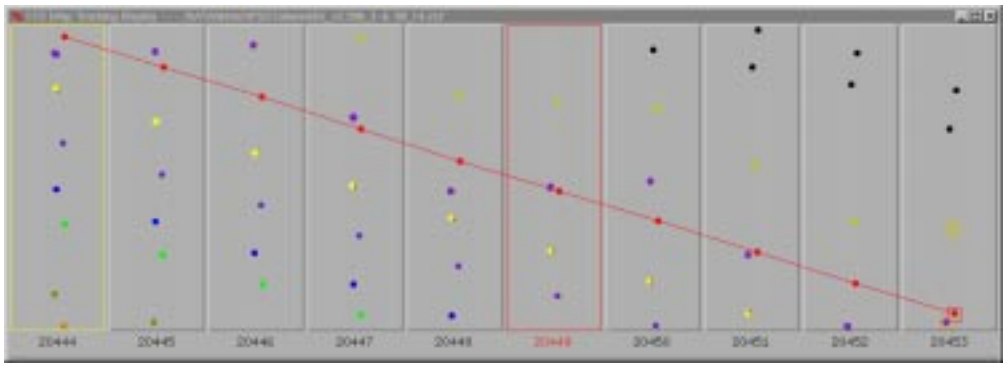

Figure 7.18: The trajectory of the anomalous event with a charge 0.294 drop.

about 20 images each time a drop with a fractional charge is measured. The measurements of the charge of these drops is done online on the raw data without any cuts or corrections applied. It was very useful to observe that most of the fractional charge artifacts whose origin we did not understand usually occurred due to a drop that was past very fast by another drop.

In this experiment the online monitoring was applied for data sets II and III.

Chapter 8

Conclusions

We have demonstrated several advantages of our Millikan method compared to the levitometer method [7] for searching for FCPs in bulk matter. The Millikan method allows a broad charge range to be studied with good charge resolution and provides natural self-calibration of the charge measurement. It is amenable to automation and simple replication and it permits a relatively large amount of material to be examined. There is no obvious limit to the amount of material to be studied [57]. We did not find any evidence for free FCPs. We found with 95% confidence that in silicone oil the concentration of particles with fractional charge more than 0.16 from the nearest integer charge is less than 4.71×10^{-22} particles per nucleon except in the region $0.26 - 0.34$ where the upper limit is 2.98×10^{-22} particles per nucleon.

Searches in bulk refined matter such as silicone oil, niobium, or iron suffer from the uncertainty of whether an FCP would remain in the material during the chemical or physical refining process [53], [58]. Pure materials also suffer from the uncertainty of whether the geochemical and geophysical processes that concentrate a mineral in a local region of the Earth's crust would also carry along any elementary FCPs. Therefore, there is great value in searching in unprocessed and unrefined bulk matter such as meteorites and certain primordial terrestrial minerals. Our subsequent searches for fractional charge particles will use drops containing such materials.

Chapter 9

Future Plans

Our first and immediate future plan is to look for FCPs in silicone oil with a much larger throughput in order to understand the significance of the event found at $q = 0.294 \pm 0.016$. Our second goal is to look for FCPs in interesting materials such as meteorites that have not under gone geochemical or geophysical processes that might exclude FCPs, again with a large mass throughput. Our third goal would be to test different terrestrial minerals. According to K. Lackner and G. Zweig [61]-[64] any FCP search should consider the chemistry of fractional charge atoms since its understanding would be a guide to what kind of material could be host to these fractional charge atoms. One of the interesting materials they suggested is fluoraptite. In either case a new method has to be used in order to achieve these goals as described in the following.

9.1 Increasing the Throughput in the Original Millikan Experiment

Fluid dynamical interactions between the drops have taught us that the traditional Millikan technique is limited as explained in chapter 7. Increasing the drop ejection rate arbitrarily decreases the spacing between the drops and increases the effect of drops being fluid dynamically coupled through the air. In addition, we learned that

taking only the Brownian motion error contribution to the charge measurement error into account we have

$$\sigma_q = \frac{\sqrt{2}}{E}\frac{\sqrt{3\pi\eta r K_B T}}{\Delta t N} \tag{9.1}$$

We see that increasing the drop diameter decreases the charge accuracy. One may also suggest using a camera with a larger number of pixels and demagnifying the image of the drop onto the CCD camera in order to have more position measurements. The problem is that it takes a long time (minutes) to clock a CCD camera with 4000×4000 pixels such as astronomers use. Another suggestion is to increase the distance between the plates in order to have more position measurements however, this requires increasing the electric field between the plates which is a problem. There is a practical problem of designing a low cost high voltage switcher. Designing a push-pull high voltage switcher with the new types of vacuum tubes will increase the cost by a factor of 100. In addition, having a uniform electric field between the plates requires increasing the size of the plates which increases the size of the whole experiment. This increases the air currents in the box and also the cost of the experiment.

Therefore, the solution is to find a new experimental method for searching for free FCPs in bulk matter. The new method derives from the traditional Millikan liquid drop method but allows the use of much larger drops, $20\,\mu$m to $100\,\mu$m in diameter compared to the traditional method that uses drops less than $12\,\mu$m in diameter. These larger drops have the advantage of being much more easily produced consistently even if they contain liquid suspensions of powdered meteorites and other special minerals. These materials are of great importance in bulk searches for fractional charge particles that may have been produced in the early universe.

9.2 The New Method

In the new method, shown in Figure [9.1], the electric field direction is horizontal and thus orthogonal to the direction of the gravitational force. Thus the effect of gravity on the drop trajectory is decoupled from that of the electric field. The equations that

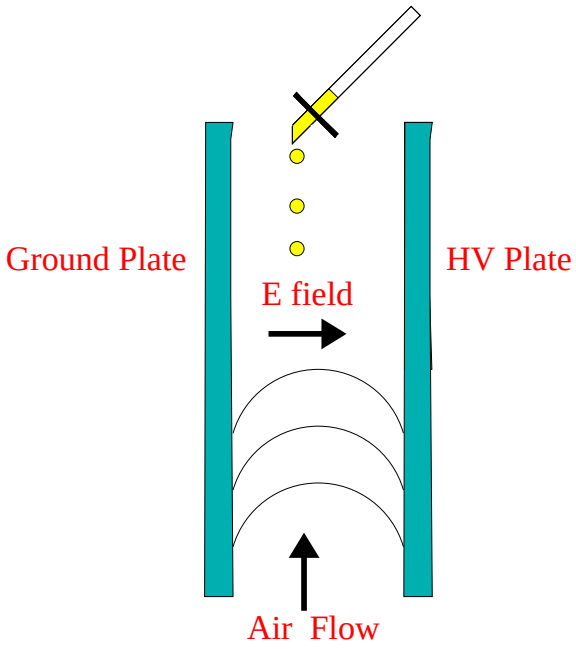

Figure 9.1: The schematic drawing of the new method to look for FCPs.

govern the motion of the drop are

$$v_x = \frac{QE}{6\pi\eta r} \tag{9.2}$$

$$v_z = \frac{2r^2\rho g}{9\eta} \tag{9.3}$$

The horizontal motion depends on the radius r and the charge on the drop Q. The vertical motion depends on the radius and the density of the fluid drop. The charge is computed by solely the measurement of v_x

$$Q = \frac{6\pi\eta r v_x}{E} \tag{9.4}$$

The radius of the drop is measured independently by using the drop image on the CCD camera. Assuming that the Brownian motion of the drop is the dominant contribution to the charge error we find that the charge accuracy for one charge

measurement is given by

$$\sigma_q = \frac{2}{E}\frac{\sqrt{3\pi\eta r K_B T}}{\Delta t N} \tag{9.5}$$

Equation (9.5) is $\sqrt{2}$ larger than the charge measurement accuracy in the traditional Millikan experiment. However the traditional Millikan experiment requires two velocity measurements per charge but the new method needs only one. Therefore the new method is equivalent to the traditional method for the same number of independent velocity measurements. In this new method, the electric field can be static or can be alternated in direction as in the traditional Millikan method. Either choice has its advantages. With a static field, the drops move smoothly along straight-line trajectories prescribed by their charge. Trajectories corresponding to differently charged drops diverge linearly with time, which if exploited, provides a means for improving the charge resolution. With an alternating field, the drop trajectory remains within a narrow range of x, simplifying the corrections. In either case the greatest advantage of the new method originates from the independence of charge determination from the measurement of the z component of the drop's trajectory; z component measurements can be ignored or altered if needed to aid the experiment. This allows increasing the drop size while maintaining good charge resolution.

9.3 The Use of Upward Airflow

In the traditional Millikan method, increasing the drop diameter decreases the charge measurement accuracy, since with a fixed z observation length, a decrease in the number of velocity measurements occurs. However in the new method, since only the horizontal component of the velocity affects the charge measurement the vertical component can be changed freely. Therefore, a laminar airflow directed upward will be introduced. We are free to alter v, by introducing a laminar, upward directed airflow against the direction of the gravitational force as seen in Figure [9.1]. The drops can be slowed vertically as needed to achieve the necessary number of velocity measurements since laminar air flows with velocities of the order of several cm/s are easily achieved. For example, the Reynolds number for a $30\mu m$ diameter drop is

$Re = 2.5 \times 10^{-3}$, resulting in a laminar flow even for $100\,\mu m$ diameter.

9.4 The Development of the Experiment

The importance of using relatively large drops is obvious. First, it allows us to test a larger mass throughput. Second, it is the only way to look for FCPs in suspensions of meteoritic and other mineral materials.

The new method that we are going to use to increase our throughput was described above. In the following we describe the method we are going to use to look for FCPs in interesting materials such as meteorites or moon dust that have not undergone any chemical processing. We already have a sample of the Allende meteorite that is supposed to be representative of the solar system in it most pristine state. Developing the new method required overcoming a few problems which are described in the following.

9.4.1 Pulverizing

Suspensions of the meteorite was prepared by mechanically pulverizing the material into a powder fine enough to be suspended. The material was not chemically processed in any way since we have no way of knowing whether we may lose a fractional charge particle during the processing or not. The first suggested method to pulverize mineral samples was to use a ball mill or a mortar and pestle. The problem is that in this method the mineral size could be reduced to only few μm. The reasons are as follows. First, minerals break at defects such as grain boundaries and the smaller the piece the less the chance that it contains defects. Second, as the mineral pieces get smaller they protect each other against further milling since their surface energy becomes larger. Therefore, the solution is to use as a second step a jet pulverizer, a device in which high-speed air jets which draw in the powder from the first step with the mineral pieces are being given relatively high kinetic energies. These pieces then collide with each other further reducing their sizes. In minerals with which we work, this produces a powder with sizes ranging from about $0.1 - 5.0\,\mu$m.

9.4.2 Suspension

After grinding the meteorite we tried to suspend this ground mineral in mineral oil. We found that simple mixing caused the particles to agglomerate separately from the solvent and settle. The solution was to use surface active agents called surfactants that are used to coat the individual particles in order to increase the repulsive force between the particles. A discussion about the technique and the preparation of the suspension can be found in Appendix C.

9.4.3 Ejection

Ejection of the suspension was jittery and unstable until at least two changes were applied. First, the aperture geometry was changed to a knife edge. Second, the dropper was oriented horizontally to prevent the settling of particles onto the orifice.

9.4.4 The Charge Problem

The last problem that had to be overcome was the charge distribution of the drop made of suspension. It was found by D. Loomba that the charge distribution was 12 with a mean around a few hundred. In a simple conductive fluid like water the mean was easy to shift using a capacitor plate close to the orifice by grounding the plate adjacent to the orifice and changing the potential on the other. Since we decided to use a nonaquaous suspension with mineral oil as the solvent the conductivity was small and a new method had to be used. The suggestion was to use a radioactive β source that generates positive and negative ions with the hope that these are going to help neutralize the charge on the drop and reduce the rms of the charge distribution. The suggestion worked and Sr^{90} was used to neutralize the ejected drops and shift the mean of the charge distribution to zero.

Appendix A

Charge Measurement Errors

A.1 Propagation of Errors into q

$$N_e \equiv \frac{q}{e} = 2Cv_e\sqrt{v_g}\,, \tag{A.1}$$

Using the expression above, the equation for propagation of errors is

$$\sigma_q^2 = \sigma_{v_e}^2(\frac{\delta q}{\delta v_e})^2 + \sigma_{v_g}^2(\frac{\delta q}{\delta v_e})^2 + \sigma_{v_e v_g}^2(\frac{\delta q}{\delta v_e})(\frac{\delta q}{\delta v_g}) \tag{A.2}$$

or

$$\sigma_q = C\,\sqrt{v_g}\sqrt{4\sigma_{v_e}^2 + 4(\frac{v_e}{v_g})\sigma_{v_e v_g}^2 + (\frac{v_e}{v_g})^2\sigma_{v_g}^2} \tag{A.3}$$

A.1.1 One Charge Measurement

For one measurement of v_e and v_g, v_e and v_g are independent with errors given by

$$\sigma_{v_e} = \frac{1}{\sqrt{2}}\sigma_{\Delta z} \tag{A.4}$$

$$\sigma_{v_g} = \frac{1}{\sqrt{2}}\sigma_{\Delta z} \tag{A.5}$$

$$\sigma_{v_g v_e} = 0 \tag{A.6}$$

Substituting these in Equation (A.3), we have for one q measurement

$$\sigma_q = C\sqrt{v_g}\sigma_{\Delta z}\sqrt{2 + \frac{1}{2}(\frac{v_e}{v_g})^2} \tag{A.7}$$

The ratio $v_e/v_g \propto 1/r^3$, and is 1 for a drop of roughly $3\,\mu$m diameter. In our experiment we used drops with $7.6 - 10.4\,\mu$m diameter. Therefore, this lead to an uncertainty of less than 3% for data set one and less than 0.5% for the other data sets. Neglecting this term in σ_q gives the result

$$\sigma_q = \sqrt{2}C\sqrt{v_g}\sigma_{\Delta z} \tag{A.8}$$

Looking at Equation (A.11), the approximation that v_e/v_g is small also implies that the fractional error in q is dominated by the fractional error in v_e.

$$\frac{\sigma_q}{q} = \frac{\sigma_{v_e}}{v_e} \tag{A.9}$$

which is equivalent to Equation (A.8).

A.2 The Temperature Variation Effect

We did not take temperature affects into account because of the following reasons. The temperature appears only through the viscosity as shown in Equation (A.10)

The viscosity of the air is given by:

$$\eta = \frac{A\ T^{3/2}}{B + T} \quad , \tag{A.10}$$

where the A, B are the following constants

$$\begin{aligned} A &= 1.485 \times 10^{-6} \quad kg\ m^{-1}s^{-1}K^{\frac{-1}{2}} \\ B &= 110.4 \quad K \end{aligned}$$

$$\begin{aligned}
\rho_{oil} - \rho_{air} &= 911.77 \quad kg/m^3 \\
g &= 9.8 \quad m/s^3 \\
d &= 10.8 \quad mm \\
V_i &= 10 \quad kV \quad i = u, dw \\
T &= 296 \quad K \\
K_B &= 1.3807 \times 10^{-23} J \quad K^{-1} ,
\end{aligned}$$

$$N_e \equiv \frac{q}{e} = 2C v_e \sqrt{v_g} , \tag{A.11}$$

$$C = \frac{9\ \pi}{e} \quad \sqrt{\frac{2}{(\rho_{oil} - \rho_{air})\ g}} \quad \frac{1}{E \quad \eta^{3/2}} \tag{A.12}$$

Estimating the contribution of the temperature variation to the charge measurement for data set I we get

$$\sigma_Q = (\frac{dQ}{dT})\Delta T \tag{A.13}$$

$$= 0.0332754(\frac{T^{1.5}}{110.4+T})^{0.5}(-\frac{T^{1.5}}{(110.4+T)^2} + \frac{1.5T^{0.5}}{110.4+T})\Delta T \tag{A.14}$$

which is less than 1%. The same estimate is made for the other data sets and the results are presented in Table [A.1].

Data set	diameter (in μm)	$\frac{\sigma_{q_T}}{\sigma_{q_{all}}}$
I	7.6	0.033%
II	10.4	0.038%
III	9.4	0.039%

Table A.1: The contribution of temperature variation to the charge measurement accuracy σ_q for each data set. The temperature variation is presented as the percentage change in σ_q.

A.3 The Angle of Rotation Effect

As mentioned above, we used a CCD camera to image the drops. The active region of the CCD was 6.4 mm ×4.8 mm (736 × 242 pixels) where the 6.4 mm edge was chosen along the trajectory of the falling drops. However we found out that the 6.4 mm edge of the camera was not perfectly aligned with the trajectory of the falling drops axis. The angle between these axes led to a correction for each (x,z) position of the drop as given in the following

$$\begin{aligned} x' &= x * cos(\theta) + z * (\text{xppm/zppm}) * sin(\theta) \\ z' &= z * cos(\theta) - x * (\text{zppm/xppm}) * sin(\theta) \end{aligned} \tag{A.15}$$

where θ is the angle between the z axis of the CCD camera and the trajectory of the falling drops axis, xppm and yppm are the number of pixel per milimeter along the x and y axis of the camera respectively. The value of these variables were measured to be $\theta = 0.018\,\text{rad}$, $xppm = 196.\,\text{pixel/mm}$, $zppm = 455.\,\text{pixel/mm}$. Therefore the misalignment changed the drops velocities by

$$\Delta z \rightarrow \Delta z * cos(\theta) - \Delta x * (\text{zppm/xppm}) * sin(\theta) \tag{A.16}$$

From Equation (A.8) above we find that σ_q would change less than a percent; therefore this correction was ignored in this work.

$$\frac{\sigma_{q'}}{\sigma_q} \sim (1 - cos(\theta)) \sim 5 \times 10^{-8} \tag{A.17}$$

A.4 The Stokes Correction Effect

The atmosphere is not a perfect continuum and therefore small drops will be prone to interactions with the nearby molecules.

The correction to Stokes' law is given by the Cunningham correction factor

$$C_c = 1 + (2\lambda/d)(A + Qe^{(\frac{-bd}{2\lambda})}) \tag{A.18}$$

where $A = 1.252$, $Q = 0.399$, $b = 1.10$, $\lambda = 0.065\,\mu$m and $d =$ drop diameter. C_c is always equal or greater than 1. In our experiment we produced drops with $d > 2\lambda$; therefore C_c can be approximated by the expression

$$C_c = 1 + \frac{2\lambda}{d}A \tag{A.19}$$

Inserting the Cunningham correction to the equation of motion governed by Stokes' law equations [4.1] and 4.2] and then solving for the radius of the drop we find that

$$r \to r - A\lambda \tag{A.20}$$

From the equation above we found that $\sigma_q \sim \sqrt{r}$. Therefore including Stokes' correction would change the charge measurment accuracy by

$$\frac{\sigma_{q'}}{\sigma_q} \approx \sqrt{\frac{r - A\lambda}{r}} \tag{A.21}$$

The percentage contribution of Stokes' correction to the charge measurement error for all data sets are given in Table [A.2].

Data set	diameter (in μm)	σ_q
I	7.6	1.07%
II	10.4	0.78%
III	9.4	0.87%

Table A.2: The contribution of Stokes correction to the charge measurement accuracy σ_q for each data sets. The Stokes correction is presented as the percentage change in σ_q.

Again as we see in Table [A.2] Stokes' correction yields less than a percent variation to the charge measurement accuracy. Therefore this correction was not applied in our work.

Appendix B

Massive Particle Search

B.1 Introduction

A new and simple method was offered [58] to search for massive stable charged particles. We first assumed that these particles were produced in the early universe with a mass larger than $10 \times 10^{13}\,\mathrm{GeV/c^2}$ and that some abundance of them remains today. The search is motivated by the opportunity to look for particles that are beyond the reach of current or projected accelerator searches.

B.2 The Experimental Layout

The experimental layout is very similar to the improved Millikan setup described in chapter 5. We mounted all the hardware on a vibrationally damped optical table and drops were produced and ejected inside the main Millikan chamber. The main difference was that the falling drops were backlit by a 1000 LED strobe instead of a small two dimensional LED array. We built an 8 inch diameter hemisphere in order to focus the LEDs on the drops. The hemisphere is made from epoxy resin and a few layers of fiberglass cloth. All the LEDs were divided to 40 modules of 5×5 LEDs each with its own driver. The reason we needed so many LEDs is that we had to use a $1\,\mu$m pulse width to backlit the drops. A picture of the LED strobe backlighting the falling drops in the main chamber is shown in Figure [B.1]. We planned to test

Figure B.1: A picture of the LED strobe backlighting the falling drops in the main chamber.

5 μm diameter drops and therefore a 135 mm focal length lens was used in order to magnify the images of the drops onto CCD camera. Inside the Millikan chamber we built an additional transparent polycarbonate box with dimensions of $1 \times 1.5\,\mathrm{in}^2$ and a height of 4 in to shield the drops from convection or other air currents due to their small radius.

B.3 The Theory of the Search

The method to look for massive particles is similar to the Millikan oil drop method. We assume a drop falling in the air under the influence of gravity. Since the drop falls in the air, the air exerts a resistive force on the drop that will cause the drop to reach terminal velocity in few milliseconds according to Stoke's Law. The equation that governs the motion of the drop is

$$v(m) = \frac{m\ g}{6\pi\eta r}\,. \tag{B.1}$$

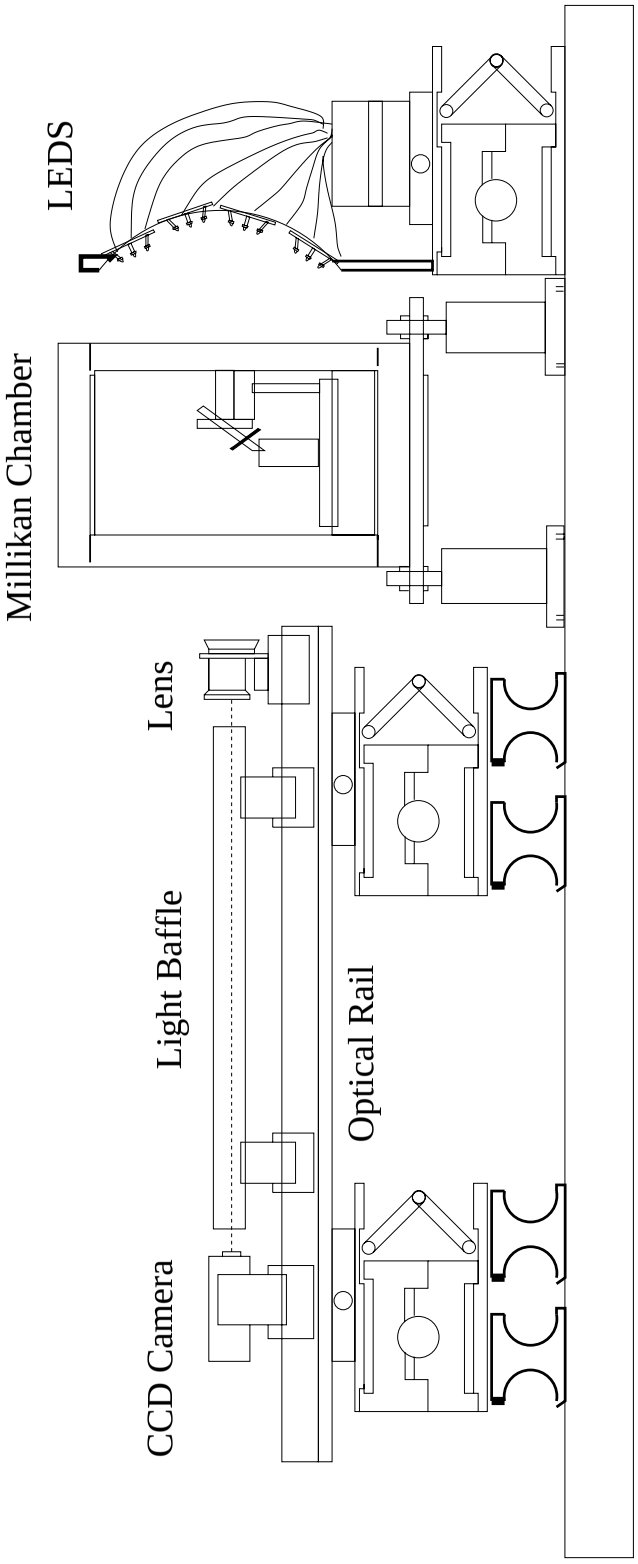

Figure B.2: The layout of massive particle search experiment.

where m and r are the mass and radius of the drop respectively, and η is the viscosity of the air. We see that $v(m)$ the larger the mass of the drop the larger the terminal velocity. Using the relation

$$m = \frac{4\pi\rho r^3}{3}\,. \tag{B.2}$$

we get

$$v = \frac{2g\rho r^2}{9\eta}\,. \tag{B.3}$$

As we see from Equation (B.3) once we measure the terminal velocity of the drop we can find the radius of the drop and hence the mass of the drop assuming known density fluids using the Equation (B.2).

In this experiment we generate a large number of drops with radius r and mass m. Consider a few drops that contain a charged, stable, massive elementary particle with a mass M. The terminal velocities of these drops would be

$$v(m+M) = \frac{(m+M)\ g}{6\pi\eta r}\,. \tag{B.4}$$

Figure [B.3] illustrates an expected result in case particles with mass 4.2×10^{13} GeV/c^2 are attached to 5×10^{13} GeV/c^2 drops. The method depends on the fact that we can produce uniform radius drops and are able to distinguish between drops with large radius or rare events v(m+M) that are caused by a massive particle attached to the drop. In order to prevent the problem described above from happening we would have an independent measurement of the radius for each drop.

B.4 The Method of the Search

The method proposed to look for massive particles was to grind up the meteorite sample using a jet pulverizer and then to suspend the ground meteorite in mineral oil. Once the suspension is stable we will eject fluid drops using a drop generator to

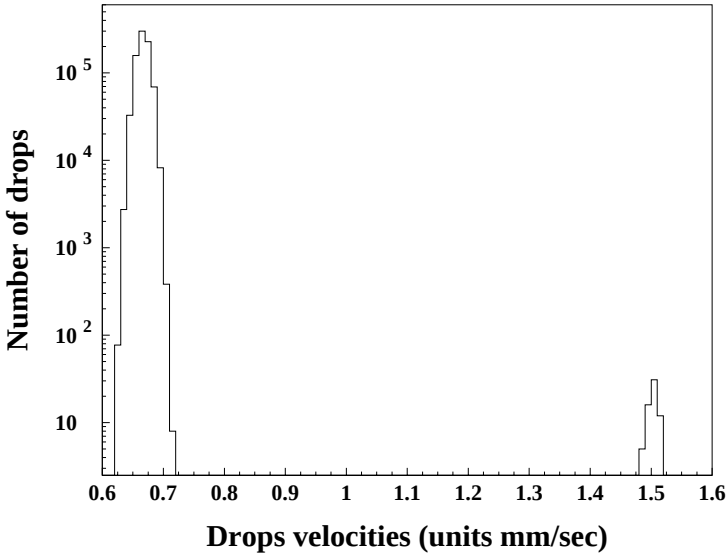

Figure B.3: A simulation of the expected results for mass $4.2 \times 10^{13}\,\mathrm{GeV/c^2}$ particles attached to $5 \times 10^{13}\,\mathrm{GeV/c^2}$ drops.

generate drops on demand. The dropper will be glued to piezoelectric plate that will move the dropper back and fourth so that the drops would have a smaller chance to collide. In addition, a special LED strobe was designed and built to provide $4-5$ bursts of $1\,\mu$s pulses every $0.1\,$s and with a variable delay time between them. The number of short pulses depend on the number of measurement we want per drop. The pulse width and the delay between pulses were chosen to prevent an image of the drop onto the CCD camera to look like a strike. Otherwise, the calculation of the position of the drop as a function of time will not be possible. These times put upper and lower limits on the velocity and hence on the mass of the particle that we are sensitive to. The triggering of 5 fast pulses every 100 ms was designed and built using an eprom. The times were adjustable depending on the mass range of the particles we were looking for and the CCD camera resolution. For example, if we choose 5 $1\,\mu$s pulses with 1 ms delay between them we find that the mass range of the particles we are sensitive to is between $1.7 \times 10^{13}\,\mathrm{GeV/c^2}$ and $1.0 \times 10^{17}\,\mathrm{GeV/c^2}$. This mass range is compatible with the first two limits explained below. However, as we were building the experiment we discovered a few more limits that lead us to reevaluate

the proposed technique to look for massive particles.

B.5 Limitations

In the following we give different constraints that limit the mass range we wanted to study. The first two points discuss the original mass range proposed for a massive particle search using the technique described in this chapter. The rest bring new constraints that questioned the technique we proposed.

1. The smallest drops we can generate with stable ejection properties are $5\,\mu$m diameter drops. This size corresponds to a mass of $5 \times 10^{13}\,\mathrm{GeV/c^2}$. Using the drop on demand technique described in chapter 5 we are able to produce uniform size drops once we set the pulse shape and amplitude to better than a 0.1%. Our limitations come from the possibility that once in a while larger drops would be produced corresponding to larger velocities and hence heavier drops. A larger drop could lead us to conclude that the drop contains a heavy particle which is a false signal. Therefore, we will use two independent measurements of the radius: one from the velocity of the drop and another from the intensity distribution of drop image onto the CCD camera. The latter technique is able to tell the size of the drop up to 1%. Therefore, we are going to restrict ourself to a particle mass $M > m$ larger than the drop mass.

   The lower limit comes from the ability to produce stable small drops as explained above with $r > 5\,\mu m$ corresponding to $M > 5 \times 10^{13}\,\mathrm{GeV/c^2}$.

2. The upper limit comes from the necessity that the massive particle remains bound to ordinary matter in Earth's gravitational field. Since we assume that the massive particle has electric charge e, the Coulomb force or the binding force to matter should be larger than the gravitational force on the particle $F_c > Mg$. $F_c = 1\mathrm{eV}/10^{-10}N$ where 1 eV is the binding energy and 10^{-10} m is the distance between atoms. We get $F_c = 1.6 \times 10^{-9}N$ and $M < F_c/g \sim 1.6 \times 10^{-10}Kg \sim 10^{17}\,\mathrm{GeV/c^2}$.

3. Assuming the massive particle is contained inside a $1\,\mu m$ ground meteorite particle, in order for the massive particle not to fall from the drop the surface tension of the drop should hold the piece of meteorite containing the massive particle. Estimates lead to $M \leq 10^{19}\,\mathrm{GeV/c^2}$ which is weaker than the limit obtained in point 2.

4. Meteorites that enter Earth's atmosphere undergo a deceleration of the order of $100 - 1000\,\mathrm{g}$. Therefore, very massive particles contained in the meteorite which suffer this deceleration could be dislodged. This acceleration puts an upper limit on the mass of the heavy particle. This weakens the upper limit arising from Coulomb attraction to $M < 10^{14}\,\mathrm{GeV/c^2}$.

5. Assuming that very massive particles are bound to our galaxy, they would have to have the virial velocity of $\beta = 10^{-3}$. According to point 1 the lower limit on the mass of the particle we can study is $M > 5 \times 10^{13}\,\mathrm{GeV/c^2}$. The kinetic energies of these particles is $E_k \geq 10^6\,\mathrm{GeV}$. Massive particles with such high kinetic energies will not be able to lose enough of their energy in order to bound to normal matter. Our conclusion is that we will not be able to look for massive particles is the mass range $10^{13} - 10^{17}\,\mathrm{GeV/c^2}$ using the technique proposed in this chapter since these particles will keep moving in the halo of our galaxy and will never condense onto ordinary matter.

6. The air jet pulverizer used in our experiment to grind the mineral we are interested in studying set strigent limit on the mass of the heavy particles we are able to look for. The air jet pulverizer works by using high-speed air jets which gives the particles relatively high kinetic energies causing the particles to collide with each other to further reduce their sizes. The air jets move the particles in a circle to speeds close to Mach $1 - 2$ accelerating them to $a \sim 5 \times 10^5 g$ and therefore scaling down the upper limit explained in point 2 to $M < 10^{12}\,\mathrm{GeV/c^2}$. This constraint rules out the proposed technique to look for massive particles unless we come up with a new way to grind up the meteorite.

7. Our drops are ejected from a drop generator as explained in chaper 5. The ejected fluid is acelarated to $\sim$ 5000 g leading the drops to reach a terminal velocity of few millimeters per second. The problem is that a massive particle experiencing an acceleration of $\sim$ 5000 g will be dislodged from its location inside the meteorite. As a result, the mass upper limit is estimated to be $M < 10^{13}\,\mathrm{GeV/c^2}$. The small mass difference between the upper and lower limits raises the effectiveness of the proposed technique to look for massive particles unless we come up with a new way to eject our drops.

Appendix C

Colloid Suspensions Using Surfactants

There is great value in searching for fractional electric charge particles in unprocessed and unrefined bulk matter such as meteorites and certain primordial terrestrial minerals. Pure materials suffer from the uncertainty of whether the geochemical and geophysical processes that concentrate a mineral in a local region of the Earth's crust would also carry along any elementary FCPs or not. Our subsequent searches for FCPs will use drops containing such materials.

C.1 Surfactants

In order to prepare a suspension which is a dispersion of a solid in a liquid we had to overcome the problem that solid particles separate from the fluid and settle at the bottom of the test tube. The solution was to use surfactants. A surfactant-surface active agent- represents a chemical compound which consists of a hydrocarbon and a polar or ionic portion. The hydrocarbon portion which is referred as hydro/lipophobic has a weak affinity to the liquid and the ionic or polar portion which is referred as the hydro/lipophilic has a strong affinity to the base liquid the suspension is prepared in. Surfactants are classified by the nature of the polar head: ionic, nonionic and polymeric surfactants.

C.2 Dispersion

Surfactants play an important role in preparing suspensions of the right particle size that will be stable for an extended period of time. The usual way of preparing a suspension is to add a solid to a small amount of liquid, to grind it to the required size and then to disperse the concentrate into a larger volume of liquid. In the dispersion process new solid/liquid interfaces are formed. The surfactant will reduce the interfacial energy at the solid/liquid interface and therefore facilitate the formation of new interfaces. The surfactant must stabilize the particles against aggregation /sedimentation. The way we prepared a nonaquaous suspension of meteorite is the following:

- Grind the meteorite using an air jet pulverizer. We get a particle size distribution with about 90% (by volume) with less than 1 μm diameter.
- Warm the solvent (in our case the oil).
- Prepare a solution of oil and surfactant by adding few percent (by weight) of the surfactant and then put the mixture into a sonicating bath for about 30 minutes to get a homogeneous solution.
- Measure a few percent (by weight) of the meteorite and mix it with a little amount of the solution previously prepared.
- Disperse the concentrate into a larger volume of liquid while sonicating overnight.

C.3 Stability of Particles in Solutions

The suspension will be stable if any attractive force can be countered by a repulsive force between the particles. The attractive forces can be London or electrodynamic forces arising from the fluctuations in the electron distribution of the molecules which make up the particles (long range). The repulsive forces arise from the electrostatic interaction of charged ions or steric forces.

C.3.1 Electrostatic Stabilization

The theory that explains the stabilization of the suspension is DLVO (Derjaguin, Landau, Verwy and Overbeek). This theory takes into account the Van der Waals attractive force and the electrostatic repulsion of similarly charges particles. The net effect is an energy barrier. The influence of the surfactant is that the adsorption of the lyophobic tail on the solid causes the solid to acquire a charge which will repel similarly charged particles by increasing the electrostatic force. This energy barrier will prevent reaggregation. The adsorption is due to the Van der Waals interaction between the hydrophobic/solid.

C.3.2 Steric Stabilization

Dispersions of solids in liquids can be stabilized by steric barriers. Such barriers can be produced when portions of molecules adsorbed onto the surfaces of the solid particles extend into the liquid phase and interact with each other. Steric effects increase with the number of adsorbed chains per unit of surface area on the dispersed particles and with the length of the chains. Steric stabilization is most effective when one group of the adsorbed molecules has only limited solubility in the liquid while the other has a strong interaction with the liquid. Therefore, the adsorbed polymer layer is thick enough to cause the particles to be far apart. As a result, the dispersion force attraction between the particles is insignificant. In nonaqueous media electrical barriers are usually less effective for preventing aggregates but steric barriers are generally required to disperse solid particles.

C.4 List of Preferred Stable Suspensions

We ordered many surfactants and a few different types of mineral oil that were used as the solvent for the suspension. The type of surfactant we ended up using is polyisobutenyl succinimide (PS) which is usually used as a dispersent in commercial motor oil. This dispersant has a 2500 mw polyisobutenyl tail and its “head group” has imide, amide and amine functional groups with (fewer) carboxyllic acid and hydroxyl

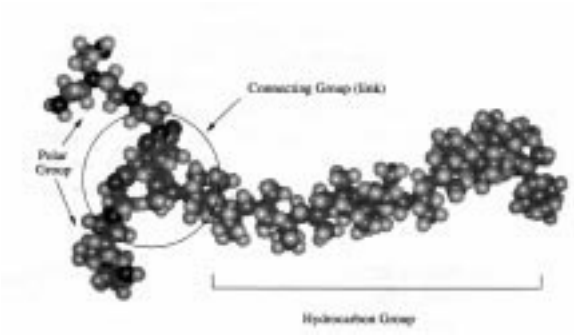

Figure C.1: The molecular structure of polyisobutenyl succinimide dispersant.

10 ml solvent	Surfactants % by wt	Meteorite
Chevron 100R / Squalene oil	2% OLOA 1200	1% by wt
Chevron 100R / Squalene oil	3% OLOA 1200 + 2% PS	"
Chevron 100R /Squalene oil	6% OLOA 1200 + 3% PS	"
chevron 100R /Squalene oil	25% HiTEC 646	"
Chevron 100R oil	4% OLOA 2500 + 2% PS	"
Ultraol mineral oil	3% OLOA 2500	"
Ultraol mineral oil	3% Castrol CA4000	"
27 oil $\frac{\rho}{\rho_0} = 2$	–	"

Table C.1: Summary of stable meteorite suspension. The table describes the solvent the suspension was prepared in, the surfactants used and their precentanges (by weight) in the suspension. All suspensions included 1% (by weight) of Allende meteorite.

functional groups. The general structure of this molecule is shown in Figure [C.1]. Dispersing particles with acidic functional groups on the surface adheres well due to acid base attraction; therefore we believe that the same is true for silica and probably various other silicates. We already have a sample of the Allende meteorite which is a carbonaceous chondrite meteorite which we believe has about 70% of its mass Olivine and Pyroxene. The chemical composition of Olivine is Fe_2SiO_4 or Mg_2SiO_4 and of Pyroxene is $Fe_2Si_2O_6$ or $Mg_2Si_2O_6$. In Table [C.1] we have a summary of suspensions that have shown stability for about a week. The table describes the content of the suspensions which includes the type of solvent and the percentage (by weight) of the different surfactants used. All suspensions included 1% by weight of the meteorite.

We have tested whether the third suspension is ejectable or not and found that we could eject fluid drops from the this sample through a $75-35\,\mu$m diameter orifice. To receive information on surfactants one should contact one of the four research groups working in this field which are the companies Lubrizol, Infineum, Ornite and Ethyl.

Appendix D

Open Questions

D.1 The Charge Imbalance

In April 1998 we concluded taking the first data set in which we accumulated 1 mg of silicone oil as can be seen in Figure [D.1].

The charge distribution shows a narrow peak around zero but when we resumed taking data in July 1998, we noticed that the charges of the drops became more positive with time. In addition, there was a clear and enhanced imbalance between the number of positive and negative drops. This imbalance remained to the end of the run as can be seen in Figure [D.2].

We think the charge imbalance may be a result of the tribo-electric or the streaming effect. However, neither of these can account for the change of the charge imbalance in time.

D.2 Intermittent Stoppage of Drop Ejection

In September 1998 we decided to generate four coloumns of multiple drops, each ejected at a frequency of 3 Hz. The drop ejection exhibited an unintentional, intermittent behavior as can be seen in the two plots that appear in Figure [D.3]. The drops seem to run for 2 hours and 40 minutes on average and than to stop for a period of 11.5 min on average. The upper plot shows the time the drop ejection continued

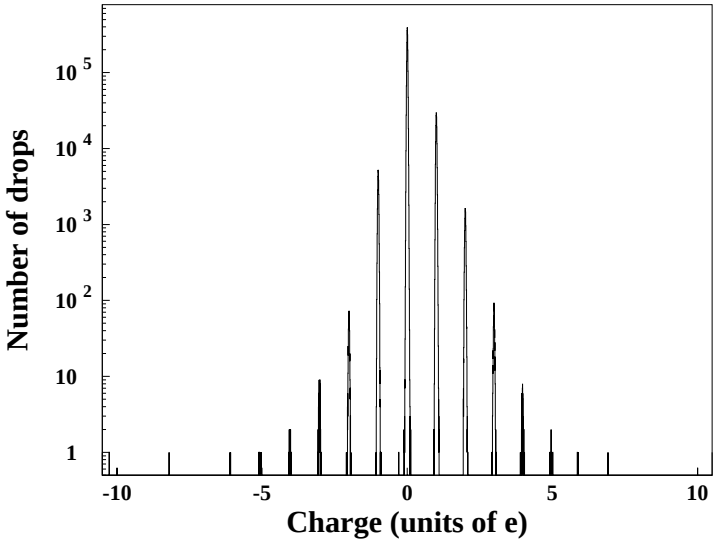

Figure D.1: The charge distribution of data set I.

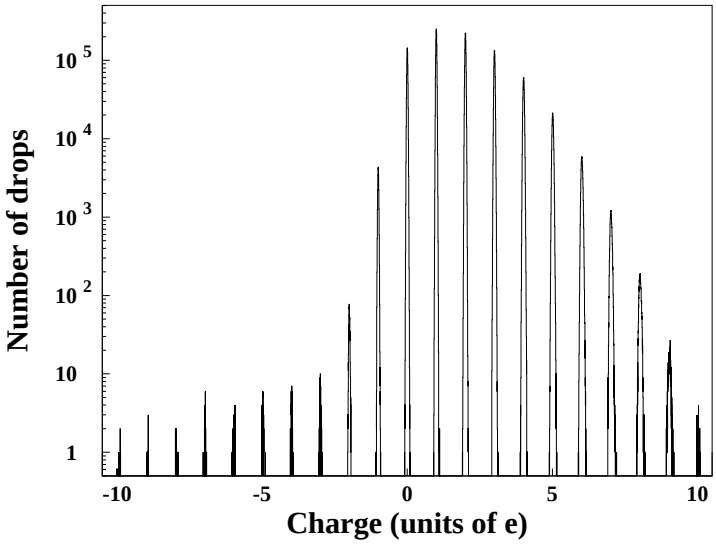

Figure D.2: The charge distribution of data set II.

uninterrupted versus the 88 hours of run time. The lower plot shows the period of time drop ejection stopped each time versus the 88 hours of run time. The reason for the drop ejection to stop for few minutes and start over again is an unsolved question.

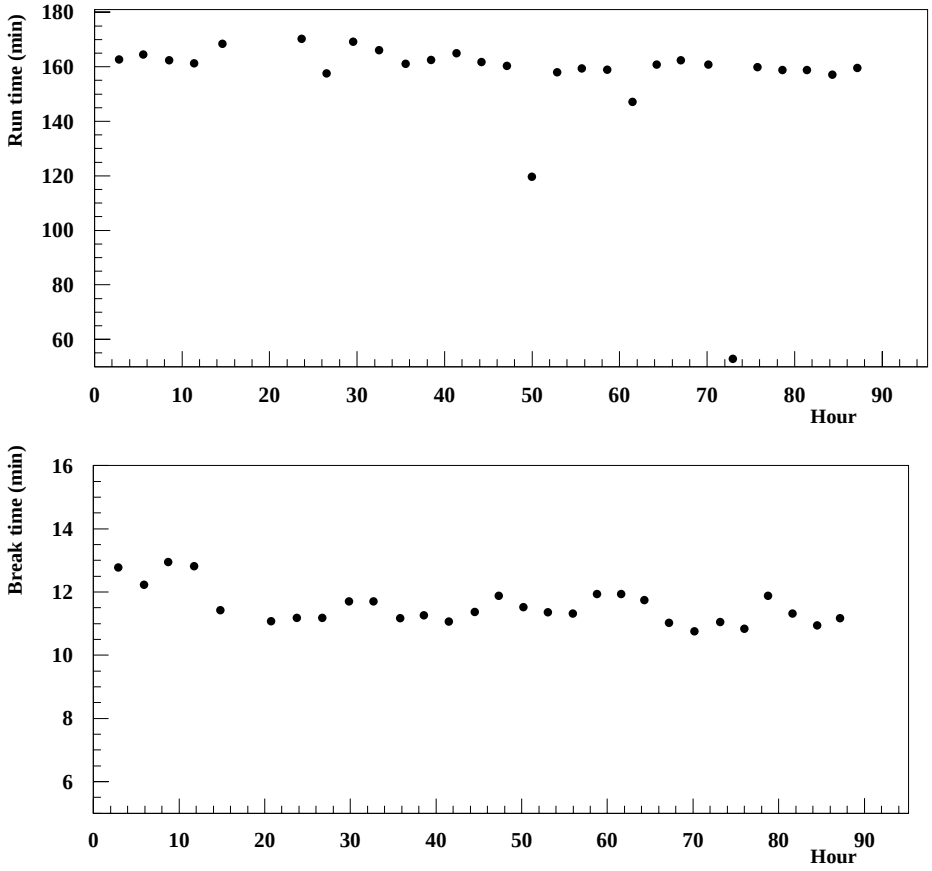

Figure D.3: The two figures above show the drop production stoppage. The top figure shows that this happens on average every 3 hours and the bottom one shows that it lasts for about 12 minutes.

Bibliography

[1] L. Lyons, *Phys. Rep.* **129**, 225 (1985)

[2] P.F. Smith, *Ann. Rev. Nucl. Part. Sci.* **39**, 73-111 (1989).

[3] L. Jones, *Rev. Mod. Phys.* **49**, 717 (1977).

[4] D. C. Joyce *et al.*, *Phys. Rev. Lett.* **51**, 731 (1983).

[5] P. F. Smith *et al.*, *Phys. Lett.* B **171**, 129 (1986).

[6] N. M. Mar *et al.*, *Phys. Rev.* D **53**, 11 (1986).

[7] P. F. Smith *et al.*, *Phys. Lett.* B **153**, 188 (1985).

[8] P. Abreu *et al.*, *Phys. Lett.* B **396**, 315 (1997).

[9] F. Abe *et al.*, *Phys. Rev.* D **46**, 1889 (1992).

[10] J.J. Aubert *et al.*, *Phys. Lett.* B **133**, 461 (1983).

[11] A. Bussiere *et al.*, *Nucl. Phys.* B **174**, 1 (1980).

[12] M. Basile *et al.*, *Phys. Rev.* **45**, 171 (1978).

[13] C.W. Fabjan *et al.*, *Nucl. Phys.* B **101**, 349 (1975).

[14] T. Nash *et al.*, *Phys. Rev. Lett.* **32**, 858 (1974).

[15] B. Alper *et al.*, *Phys. Lett.* B **46**, 265 (1973).

[16] L.B. Leipuner *et al.*, *Phys. Rev. Lett.* **31**, 1226 (1973).

[17] R. Akers *et al.*, *Phys. Rev.* C **67**, 203 (1995).

[18] D. Buskulic *et al.*, *Phys. Lett.* B **303**, 198 (1993).

[19] L. Lyons *et al.*, *Phys. Rev.* C **63**, 363 (1987).

[20] M. Banner *et al.*, *Phys. Lett.* B **156**, 129 (1985).

[21] A. Marini *et al.*, *Phys. Rev. Lett.* **48**, 1649 (1982).

[22] J.M. Weiss *et al.*, *Phys. Lett.* B **101**, 439 (1981).

[23] W. Bartel *Phys. Rev.* C **6**, 295 (1980).

[24] A. Milone *Suppl. Nuov. Cim.* **XII**, 353 (1954)

[25] A. Milone, Suppl. Nuov. Cim. XII (1954) 353.

[26] S. Tokunaga and T. . Ishii, Nuov. Cim. V (1957) 517.

[27] P.B. Price *et al.*, *Phys. Rev. Lett.* **50**, 566 (1983).

[28] S.W. Barwick *et al.*, *Phys. Rev.* D **30**, 691 (1984).

[29] M.A. Bloomer *et al.*, *Phys. Lett.* B **138**, 373 (1984).

[30] J. Napolitano *et al.*, *Phys. Rev.* D **25**, 2837 (1982).
S. J. Freedman *et al.*, Vanderbilt Conerence 1982, p. 24.
A. Marini *et al.*, *Phys. Rev.* D **26**, 1777 (1982).

[31] T. Mashimo *et al.*, *Phys. Lett.* B **128**, 327 (1983).

[32] C.B.A. MaCusker, *Aust. J. Phys.* **36** 717(1983)

[33] M. W. W. Allison, *et al.*, *Phys. Rev. Lett.* **25**, 550 (1970).

[34] M. Mori *et al.*, *Phys. Rev.* D **43**, 2843 (1991).

[35] P.N. Bhat *et al.*, *Phys. Rev.* D **25**, 2820 (1982).

[36] T. Wada *et al.*, *Lett. Nuov. Cim.* **40** 329 (1984).

[37] M. Marinelli, G. Morpurgo, *Phys. Rep.* **85**, 162 (1982)

[38] LaRue *et al.*, *Phys. Rev. Lett.* **38**, 1011 (1977).

[39] LaRue *et al.*, *Phys. Rev. Lett.* **42**, 142 (1979).

[40] LaRue *et al.*, *Phys. Rev. Lett.* **46**, 967 (1981).

[41] A. F. Hebard, *Serach for fractional charge using low temperatue technique*, Thesis, Stanford Univ., Calif. (1970)

[42] G. S. LaRue, *Measurement of residual charge of superconduction niobium spheres*, Thesis, Stanford Univ., Calif. (1978)

[43] J. D. Phillips, *Residual charge of niobium spheres*, Thesis, , Stanford Univ., Calif. (1983)

[44] W. G. Jones *et al.*, Z. Phys. C, **43** 349 (1989)

[45] M. Marinelli *et al.*, *Phys. Lett.* B **137**, 439 (1984)

[46] D. Liebowitz *et al.*, *Phys. Rev. Lett.* **50**, 1640 (1983)

[47] C. L. Hodges *et al.*, *Phys. Rev. Lett.* **47**, 1651 (1981)

[48] M. A. Lindgren *et al.*, *Phys. Rev. Lett.* **51**, 1621 (1983).

[49] M. L. Savage *et al.*, *Phys. Lett.* B **167**, 481 (1986).

[50] R. A. Millikan, Phys. Rev. **32** 349 (1911)

[51] R. A. Millikan *The Electron* (The University of Chicago Press, Chicago, IL, 1963)

[52] A. N. Schellekens, *Phys. Lett.* B **237**, 363 (1990).

[53] M. L. Perl and E. R. Lee, *Am. Journ. of Phys.* **65**, 698 (1997).

[54] J. D. Bjorken *et al.*, *Phys. Rev.* D **20**, 2353 (1979).

[55] E. R. Lee and M. L. Perl, U.S. Patent 5943075 (1999).

[56] E. R. Lee *et al.*, to be published.

[57] D. Loomba *et al.*, accepted to *Rev. Scientific Instruments* .

[58] M. L. Perl, *Phys. Rev.* D **57**, 7 (1998).

[59] Colloidal System and Interfaces S. Ross I. D. Morrison.

[60] V. Halyo *et al.*, *Phys. Rev. Lett.* **84**, 2576 (1999).

[61] K. S. Lackner and G. Zweig, Lettere Al Nuovo Cimento **33** 65 (1982)

[62] K. S. Lackner and G. Zweig, Proc. AIP **93** (1982)

[63] K. S. Lackner and G. Zweig, Phys. Rev. D **28**, 1671 (1983)

[64] K. S. Lackner *et al.*Proc. Fifth Int. Conf. on Part. Phys. (May 1982)

[65] Instrument Research Company Model 1k-30. Colombia, MD 21045 USA

[66] COHU, INC. Model 4110 Digital Output Monochrome CCD Camera. San Diego, CA 92123 USA

[67] M. L. Perl, Invited talk at Cosmic Genesis and Fundamental Physics Workshop, Rohnert Park, California, 28-30 Oct 1999.